UNIVERSIDADE FEDERAL DO PARANÁ

KALEL LUIZ ROSSI

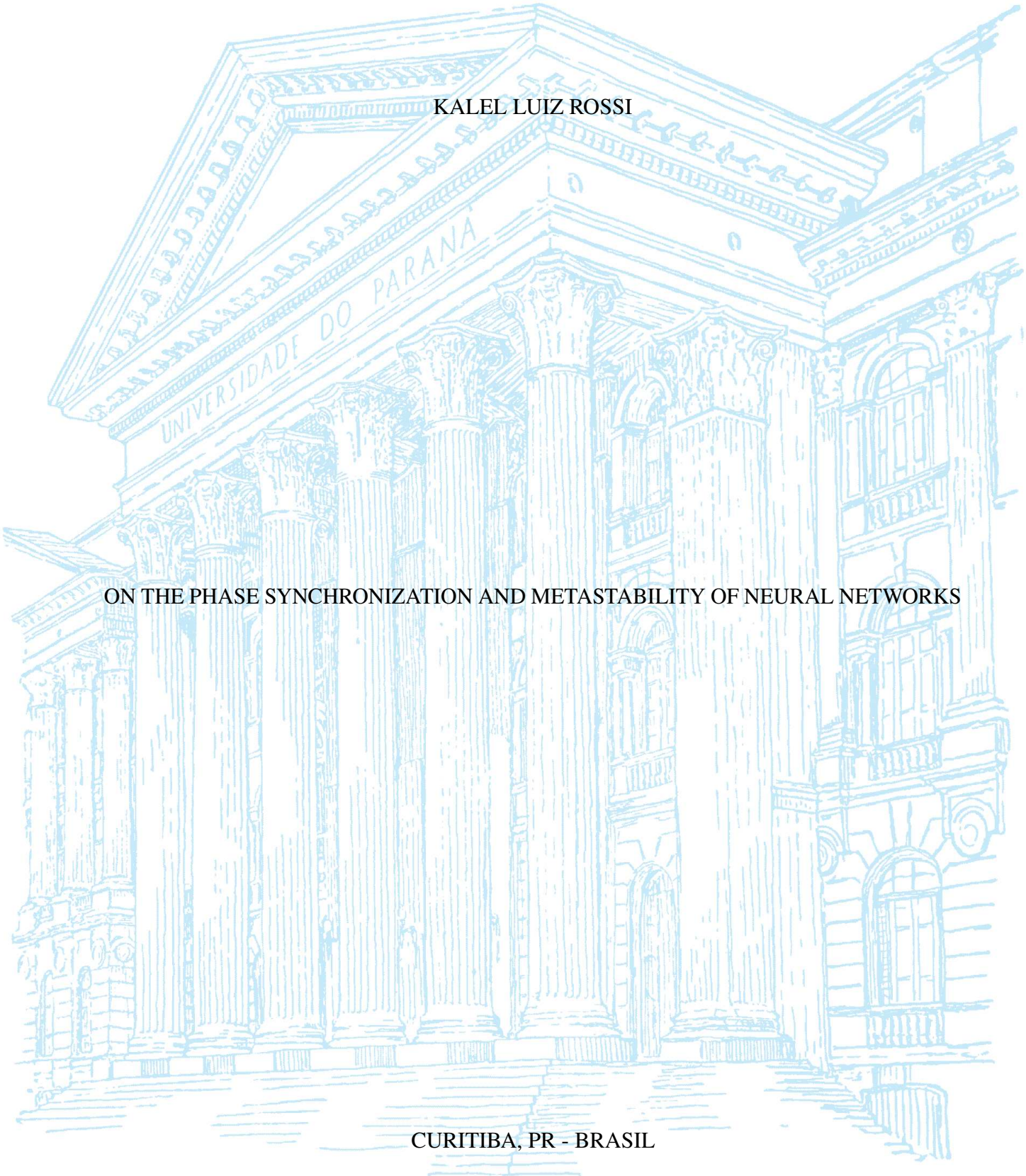

ON THE PHASE SYNCHRONIZATION AND METASTABILITY OF NEURAL NETWORKS

CURITIBA, PR - BRASIL

2021

KALEL LUIZ ROSSI

ON THE PHASE SYNCHRONIZATION AND METASTABILITY OF NEURAL NETWORKS

Dissertação apresentada ao curso de Pós-Graduação em Física, Setor de Ciências Exatas, Universidade Federal do Paraná, como requisito parcial à obtenção do título de Mestre em Física .

Orientador: Prof. Dr. Sergio Roberto Lopes.

CURITIBA, PR - BRASIL

2021

CATALOGAÇÃO NA FONTE – SIBI/UFPR

R831o Rossi, Kalel Luiz

On the phase synchronization and metastability of neural networks [recurso eletrônico]/ Kalel Luiz Rossi - Curitiba, 2021.

Dissertação apresentada como requisito para o grau de Mestre em Física na Pós-Graduação Programa em Física, Setor de Ciências Exatas, da Universidade Federal do Paraná, Brasil.

Orientador: Prof. Dr. Sergio Roberto Lopes

1. Redes neurais (Computação). 2. Neurônicos. 3. Sincronização. I. Lopes, Sérgio Roberto. II. Título. III. Universidade Federal do Paraná.

CDD 621.391

Bibliotecária: Vilma Machado CRB9/1563

TERMO DE APROVAÇÃO

Os membros da Banca Examinadora designada pelo Colegiado do Programa de Pós-Graduação em FÍSICA da Universidade Federal do Paraná foram convocados para realizar a arguição da Dissertação de Mestrado de **KALEL LUIZ ROSSI** intitulada: **"On the phase synchronization and metastability of neural networks"**, sob orientação do Prof. Dr. SERGIO ROBERTO LOPES, que após terem inquirido o aluno e realizada a avaliação do trabalho, são de parecer pela sua APROVAÇÃO no rito de defesa.
A outorga do título de mestre está sujeita à homologação pelo colegiado, ao atendimento de todas as indicações e correções solicitadas pela banca e ao pleno atendimento das demandas regimentais do Programa de Pós-Graduação.

CURITIBA, 24 de Fevereiro de 2021.

Assinatura Eletrônica
25/02/2021 09:14:09.0
SERGIO ROBERTO LOPES
Presidente da Banca Examinadora (UNIVERSIDADE FEDERAL DO PARANÁ)

Assinatura Eletrônica
25/02/2021 09:06:59.0
ELBERT EINSTEIN NEHRER MACAU
Avaliador Externo (UNIVERSIDADE FEDERAL DE SÃO PAULO)

Assinatura Eletrônica
25/02/2021 09:25:34.0
RICARDO LUIZ VIANA
Avaliador Interno (UNIVERSIDADE FEDERAL DO PARANÁ)

À minha mãe, Andrea Cristina Martins, por tudo.

ACKNOWLEDGEMENTS

Nessa dissertação, falamos bastante sobre redes de neuronios. Ao longo do caminho que culminou nesse trabalho, a rede neural que a escreveu e está escrevendo teve a ajuda, orientação, e compania de várias outras redes neurais. Gostaria de aproveitar esse espaço para agradecer a todas, em especial algumas específicas, pelo valioso papel que tiverem no seu trabalho e na sua vida. Todas essas redes neurais podem ser organizadas também em redes sociais (afinal de contas, essas redes são pessoas!). Principalmente, em redes sociais acadêmicas, redes sociais de trabalho, redes sociais pessoais e familiares. Nessa jornada, tive o prazer de ver várias dessas redes sociais se interlaçarem, à medida que colegas de pesquisa e trabalho se tornaram amigos, amigos (uma em específico) entraram pra família, e amigos conheceram outros amigos.

Tentando um pouco separar essas redes, gostaria de começar pela parte acadêmica e de trabalho. Gostaria de agradecer ao meu orientador, Prof. Dr. Sergio Roberto Lopes, pela orientação desde a iniciação científica; à minha futura orientadora Prof. Dr. Ulrike Feudel, que contribuiu muito também para o estudo aqui; às minhas bancas de pré-defesa e de defesa, Profs. Drs. Wilson Marques, Thiago de Lima Prado, Ricardo Luiz Viana e Elbert Macau, pelas críticas e sugestões; ao departamento de Física da Universidade Federal do Paraná como um todo, especialmente ao coordenador do curso, Prof. Dr. Cristiano Woellner, que esteve sempre à disposição para ajudar no que fosse necessário; ao grupo ao qual pertenço, o de Dinâmica Não-Linear e Física de Plasmas, pelas discussões; ao Conselho Nacional de Desenvolvimento Científico e Tecnológico (CNPq) pelo fomento indispensável à minha pesquisa; ao Prof. Dr. Carlos de Carvalho, que administrou as máquinas de cálculo.

Nessa rede acadêmica, tive o prazer de ter dois colegas em específico se tornarem amigos muito bons: Roberto Budzinski e Bruno Boaretto, cuja colaboração foi muito importante na parte acadêmica e pessoal. Falando na rede social, gostaria de agradecer a alguns amigos em específico, pelas conversas, discussões, e diversão em geral: Carlos Alberto Martins Jr.; João Silveira; Alexandre Camargo; Rafaela Jacuboski; Lucas Pollyceno; Marcos Sato. À amiga que é mais que do que só amiga, Maíra Theisen, que tornou o ano de 2020, condenado pela pandemia, ainda um ano bastante feliz.

Por fim, a parte talvez mais fundamental, gostaria de agradecer à rede familiar, que me tornaram essa configuração de rede neural feliz que sou: minha mãe, Andrea Cristina Martins; meu pai, Daniel Francisco Rossi; minha irmã, Isabela Rossi; minha vó, Aurea Martins; meu cunhado, Thiago Saquette.

Obrigado a todos!

RESUMO

Regiões cerebrais e neurônios precisam se comunicar eficientemente e coordenar as suas respectivas atividades. Para conseguir isso, dois fenômenos importantes são a sincronização de fase, relevante para comunicação neural, e a metastabilidade, relevante para atividade neural. Nessa dissertação, estudamos ambas em uma rede de neurônios *bursting* acoplados quimicamente sob uma topologia aleatória. A temperatura desses neurônios influencia seu modo de disparo, que pode ser *bursting* ou caótico ou periódico. O *bursting* caótico leva a uma transição não-monotônica comum, enquanto o periódico leva a transições não-monotônicas mais incomuns. Em todos os casos, observamos que as diferenças de fase entre neurônios mudam intermitentemente ao longo do tempo, mesmo em redes fortemente sincronizadas em fase. Chamamos esse fenômeno promiscuidade, e o medimos diretamente calculando como os tempos de *burst* dos neurônios flutuam entre si ao longo do tempo. Então, agrupando neurônios de acordo com suas fases, exploramos como a promiscuidade afeta a composição desses clusters, e obtemos detalhes aprofundados sobre a sincronização de fase dessa rede. Também calculamos duas variabilidades neurais, medindo como os tempos de disparo se dispersam ao longo do tempo ou da rede, e encontramos que os dois possuem valores similares e estão fortemente correlacionados com o grau de sincronização de fase da rede para acoplamento fraco. Em seguida, expandimos nosso foco para metastabilidade como vista em neurociência, considerando promiscuidade um tipo de comportamento metastável. Nós fazemos uma mini-revisão das diferentes definições do termo, e discutimos elas. Com isso, categorizamos brevemente os mecanismos dinâmicos levando à metastabilidade. Finalmente, usando o conhecimento obtido no estudo de promiscuidade, investigamos novamente a rede promíscua para discutir como metastabilidade pode diferir dependendo das múltiplas escalas do sistema.

Palavras-chave: Metastabilidade. Sincronização de Fase. Redes Neurais.

ABSTRACT

Brain regions and neurons need to communicate effectively and coordinate their respective activities. To manage this, two important phenomena are phase synchronization, relevant for neural communication, and metastability, relevant for neural activity. In this dissertation, we aim to study both in a network of chemically coupled Hodgkin-Huxley-type bursting neurons under a random topology. The temperature of these neurons influences their firing mode, which can be either chaotic or periodic bursting. The firing mode in turn influences the transitions from desynchronization to phase synchronization when neurons are coupled in networks. Chaotic bursting leads to a common monotonic transition, while periodic bursting leads to rarer nonmonotonic transitions. In all these cases, we observe that phase differences between neurons change intermittently throughout time, even in strongly phase-synchronized networks. We call this promiscuity, and measure it directly by calculating how neuron's burst times drift from each other across time. Then, grouping neurons according to their phases, we explore how promiscuity affects the composition of these clusters, and obtain detailed knowledge of the network's phase synchronization. We also calculate two neuronal variabilities, measuring how the neuronal firing times disperse over time or over the network, and find that the two have very similar values and are strongly correlated to the network's degree of PS for weak coupling. Next, we expand our focus to metastability as viewed in neuroscience, regarding promiscuity as a type of metastable behavior. We provide a mini-review of the different definitions of metastability, and discuss them. With this, we categorize briefly the dynamical mechanisms leading to metastability. Finally, using the insights gained from studying promiscuity, we investigate the promiscuous network again to discuss how metastability can differ depending on the multiple scales of a system.

Keywords: Metastability. Phase synchronization. Neural networks.

LIST OF FIGURES

LIST OF TABLES

CONTENTS

Introduction

The brain is a complex system with a huge number of cells connected in intricate ways leading to complicated behaviors on several scales. A common approach to study it is to take a localized look, and focus on networks of neurons. In this dissertation, we do this through simulations and the use of dynamical systems theory on a network of bursting neurons chemically coupled in a random topology.

This network, and similar ones, are already known to have very rich dynamics, such as nonmonotonic transitions to phase synchronization (Boaretto et al., 2018a,c, 2019), nonstationarity (Budzinski et al., 2017), intermittency (Budzinski et al., 2019a) and complex spatiotemporal patterns such as chimeras (Glaze et al., 2016). Phase synchronization is a particularly important phenomenon, due to its role as a mechanism for neuronal communication (Fries, 2005; Fell and Axmacher, 2011). Studying it, we notice that even when the networks are strongly phase-synchronized, neurons still tend to intermittently change the phase differences between themselves. We call this tendency promiscuity, characterize it, analyze its influence on cluster formation, and relate it to the variability of neuronal firing.

The understanding gained from these studies then leads us to discuss an important dynamical regime in neuroscience called metastability. Metastability is seen as the dynamical regime underlying cognitive processes in the brain (Tognoli and Kelso, 2014; La Camera et al., 2019), in part as it naturally solves the organ's need to integrate its functional areas while also keeping their functions segregated (Fingelkurts and Fingelkurts, 2004; Kelso and Tognoli, 2007). It is also more generally seen as a regime of brain dynamics, characterized by sequences of transient (metastable) states (Friston, 1997, 2000). Despite the large amount of works studying it in neuroscience, a few theoretical issues are still open in the literature. In particular, the definition of the term is not well established, and commonly used loosely. In the second part of this dissertation, we provide a mini-review of the different definitions of metastability, discuss them and what a general definition could be. We also categorize the dynamical mechanisms that can lead to it. Finally, we discuss how the observation of metastability, following a specific definition, may differ depending on the scales being studied.

To fully comprehend these results and discussions, we first need to understand the theoretical framework surrounding them. This is done in Part I. We begin in Chapter 1 focusing on the biology of neuronal networks, beginning with the fundamental units of neural networks: the neurons. We talk briefly about their electrophysiology, the mathematical formalism of Hodgkin and Huxley to model them, how their connections work and how they behave. Then, we move to networks themselves and review some important subjects regarding brain functioning, such as synchronization, brain scales, and the formation of neuronal groups. This biological knowledge then serves as motivator for the concepts in subsequent chapters.

In Chapter 2 we study the theory of dynamical systems and nonlinear dynamics, which forms the basis of our study. We talk about the stability of systems, calculation of Lyapunov exponents, characterization of attractors, bifurcations and some important dynamical behaviors.

With this theory, we in Chapter 3 look at specific models of neurons using the formalism already presented. We discuss the Nobel-winning Hodgkin-Huxley model, its dynamics, and the modifications made to it that lead to the Huber-Braun model, used in this dissertation. This model's dynamics is explored, and its biological relevance discussed.

Next, the focus goes to the theory of Complex Networks in Chapter 4. We present some aspects of this theory needed to model the connections in the network, introducing graph theory and some important connection schemes like the small-world network.

Chapter 5 contains the methods used for simulations and analysis, including the network we use, softwares for simulation, and quantifiers for characterizing the network.

Finally, in Chapter 6 we provide the theoretical discussions on metastability in neuroscience mini-review of the definitions in the literature, discussions, and categorization of the mechanisms for generating metastability.

This leaves us ready for the results, in Part II. Starting in Chapter 7 we study the phase synchronization of the network, its relation to the network variabilities and the phenomenon of promiscuity. In Chapter 8, we provide further details characterizing the network behavior, supporting our study in the previous chapter. Finally, in Chapter 9, we focus again on metastability, following a specific definition, and explore how the behavior varies depending on the scale of observation.

With all of this, we then summarize our results, present our conclusions and future works in Part III.

Part I

Theoretical framework

1 BIOLOGY OF NEURONAL NETWORKS

The animal nervous system is composed of neurons and glial cells (Kandel et al., 2000) interconnected in a nontrivial way, forming a network. It is generally considered that neurons perform the computations, processing relevant information (Koch and Segev, 2000), while glia are considered to play mostly a supportive role (Chouard and Gray, 2010) (though this view is changing (Chouard and Gray, 2010; Fields et al., 2014; Fields and Stevens-Graham, 2002) as evidence for the role of glial in information processing is increasing). Following this general view, neurons are the seen as the cells responsible for the wide range of behaviors presented by the nervous system, justifying the interest in studying networks of neurons.

This chapter therefore concerns itself with the biology of both individual neurons, interactions they make, and a bit with the behavior of brain networks.

1.1 NEURONAL COMPOSITION

Neurons are remarkable due to their ability to generate and propagate electrochemical signals (Dayan and Abbott, 2005), which serve to communicate with other cells (Kandel et al., 2000). These signals come in the form of spikes or trains of spikes (bursts). Spikes are fast, transient changes in the membrane potentials of the neuron and are the focus in the start of this chapter.

The neuronal anatomy is very important for the transmission of signals (Kandel et al., 2000), so this section aims at introducing its basic elements. Neurons receive input signals in their dendrites, which, if transmitted, go through their bodies (also called soma) and then through their axons. The signal eventually reaches the end of the neuron at the synaptic terminal, where it has a chance of being transmitted to subsequent neurons. This basic anatomy is shown in Fig 1.1.

Neurons also have embedded in their membrane specialized proteins, called ion channels and receptors, which regulate the flow of ions through the cell. These have aqueous pores which allow the passage of specific ions (in the case of ion channels), and neurotransmitters (in the case of receptors).

1.2 NEURONAL ELECTROPHYSIOLOGY

The basic ions are sodium (Na^+), potassium (K^+), calcium (Ca^{2+}) and chloride (Cl^-) (Izhikevich, 2007). Outside the cell, in the intercellular medium, the concentration of Na^+, Cl^- and Ca^{2+} is higher than inside, where the concentration of K^+ and negatively charged molecules, denoted as A^-, is higher (cf. Fig 1.2). The differences in these concentrations lead to electrochemical gradients which generate a difference in electrical potential across the cell membrane, commonly called the membrane potential V.

At rest, meaning without any stimuli external to the neuron, this difference V is generally of about $-70\,\text{mV}$, which is achieved through cell pumps that regulate the concentration of the ions (Kandel et al., 2000).

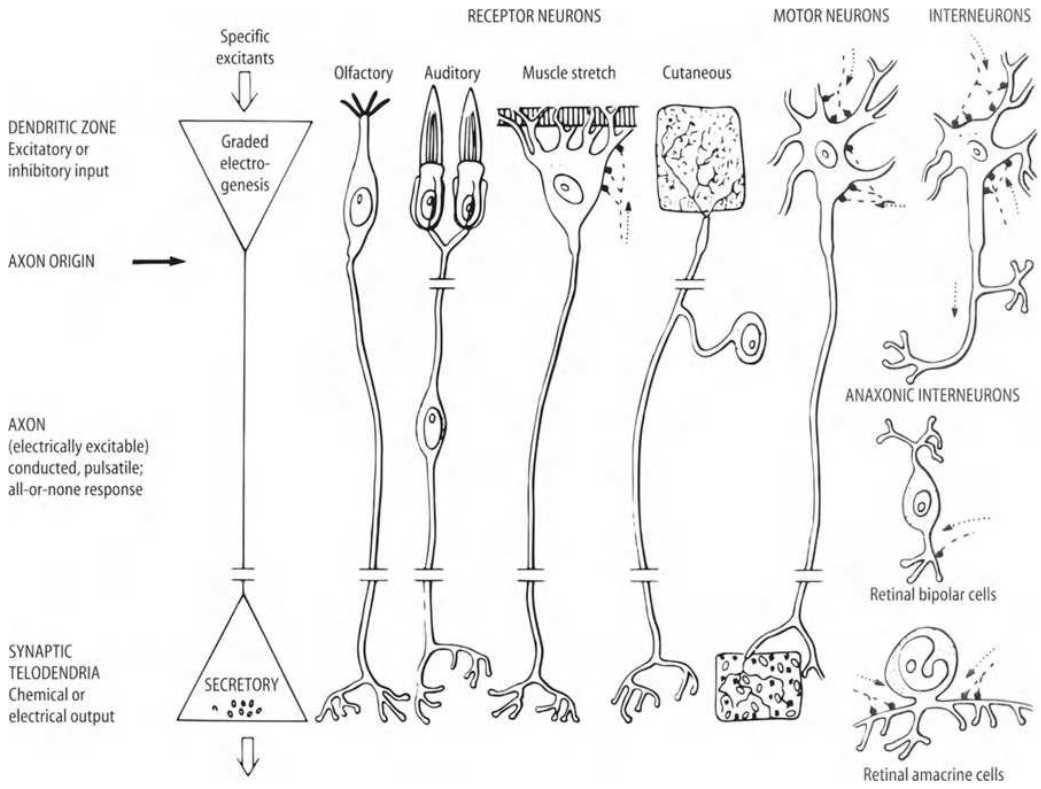

Figure 1.1: **Basic anatomy of a neuron, represented by a generalized neuron (left) and various types real of neurons.** Figure taken from (Brown, 1991).

1.2.1 Nernst potential

Each ionic species tends to follow its concentration gradient. For example, K^+, whose concentration is bigger inside the cell, tends to diffuse out. Imagining momentarily a cell with only this ionic species, equilibrium would be reached when the inside and outside were equal. If, instead, we wanted to reach an equilibrium before and stop this diffusion midway, we could apply an electric potential V to balance this concentration force. This potential V that stops the ionic flow is called the Nernst Potential E_{ion} of the ion, given by

$$E_{\text{ion}} = \frac{RT}{zF} \ln \frac{[\text{Ion}_{\text{out}}]}{[\text{Ion}_{\text{in}}]}, \tag{1.1}$$

where R is universal gas constant, T is the temperature, z is the ionic charge, F is the Faraday constant and [Ion] is the ionic concentration, measured inside or outside the cell. For reference, in monovalent ions ($z = 1$) and in body temperature ($T = 310\,\text{K} = 37\,^\circ\text{C}$), the equation becomes

$$E_{\text{ion}} \approx 62 \log_{10} \frac{[\text{Ion}_{\text{out}}]}{[\text{Ion}_{\text{in}}]} \quad (\text{mV}), \tag{1.2}$$

where we changed the logarithmic basis to 10, following (Izhikevich, 2007).

1.2.2 Ionic currents

In a real cell, there are various ionic species, each with their own Nernst potentials, in general different from the membrane voltage. This means that, even at rest, there are ionic

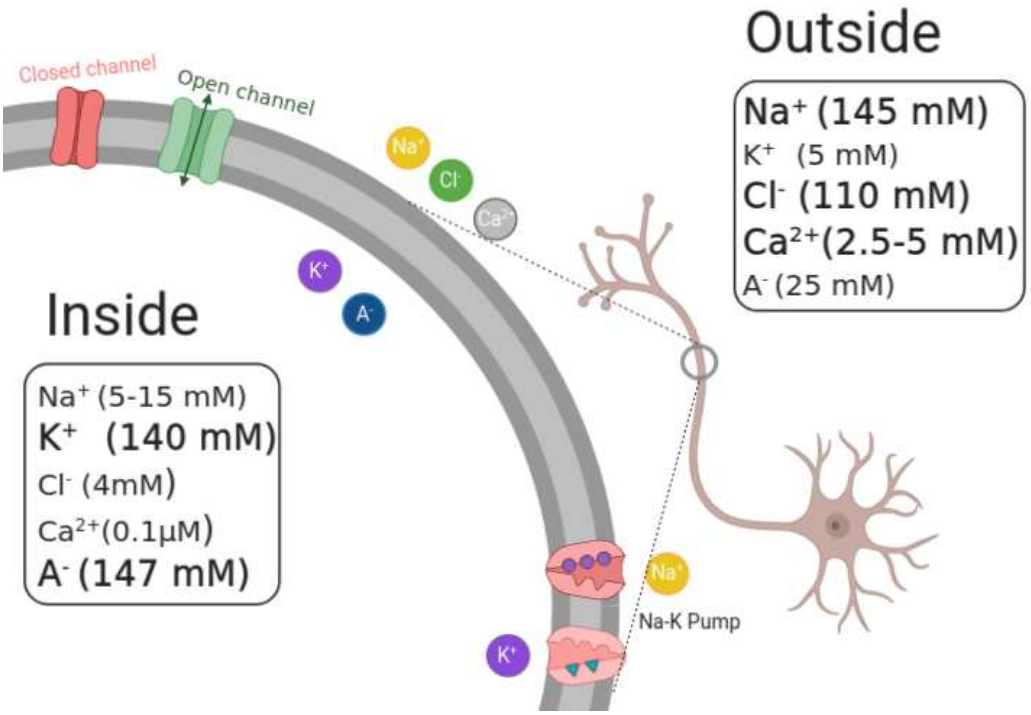

Figure 1.2: **Representation of the main ionic species in a typical mammalian neuron.** The figure contains their concentrations inside and outside the patch of cell membrane, a representation of a closed and an open channel, and the Sodium-Potassium pump. Figure inspired by (Izhikevich, 2007), and made using BioRender.

currents flowing through the membrane. We can describe the ionic current density J_{ion} as proportional to the difference between the membrane voltage V and the Nernst potential E_{ion}:

$$J_{\text{ion}} = g_{\text{ion}}(V - E_{\text{ion}}), \tag{1.3}$$

where g_{ion} is the conductance per unit area associated with each ionic species. We remark that this conductance is *not* constant, so the current is not Ohmic. In fact, the time dependence of these conductances is essential for spike generation (Izhikevich, 2007).

1.2.3 Equivalent circuit

Now, we aim to model the neuronal membrane as an electric circuit. This is the basis of the Hodgkin-Huxley model, which is discussed in detail in chapter 3.

Due to their resemblances, the membrane is considered as a capacitor with capacitance C_{M}, the ionic conductances are seen as conductors with conductance g and the ionic potentials are seen as electromotive forces E_{ion} (Johnston, 1995; Izhikevich, 2007). This is represented in Fig 1.3. Applying Kirchhoff's current law, according to which the sum of the currents at a point is zero:

$$J = J_C + J_{\text{Na}} + J_{\text{Ca}} + J_{\text{K}} + J_{\text{Cl}}, \tag{1.4}$$

where $J_C = C_{\text{M}}\dot{V} = C_{\text{M}}dV/dt$ is the capacitive current density and J_{Na}, J_{Ca}, J_{K}, and J_{Cl} the total current densities for Sodium, Calcium, Potassium, and Chloride, respectively. Now, substituting the capacitive current and the description for ionic currents in 1.3, we can write

$$C_{\text{M}}\dot{V} = J - g_{\text{Na}}(V - E_{\text{Na}}) - g_{\text{Ca}}(V - E_{\text{Ca}}) - g_{\text{K}}(V - E_{\text{K}}) - g_{\text{Cl}}(V - E_{\text{Cl}}). \tag{1.5}$$

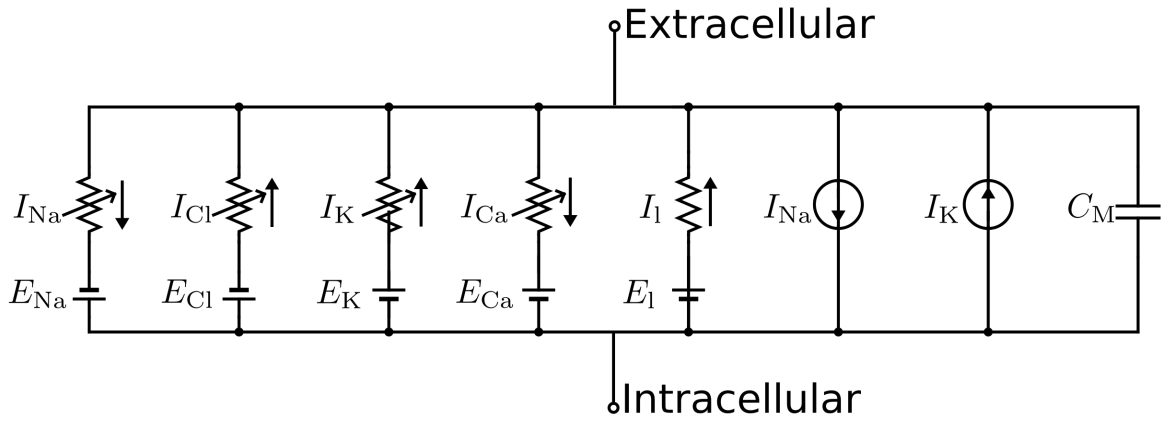

Figure 1.3: **The equivalent circuit of a patch of neuronal membrane.** The ion channels (Na, Cl, K, Ca) are represented by variable resistors; the leak current by an ohmic resistor; the electrochemical gradients for both ion and leak channels by voltage sources; Na^+ and K^+ pumps by current sources; and the membrane capacitance by a capacitor.

where C_{M} denotes the membrane capacitance per unit area, and the conductances g are taken over a unit area. Equation 1.5 is the basis for our modelling of the neuronal dynamics. With the description of the ionic conductances, in Section 1.2.4, we have the ingredients for the Hodgkin-Huxley model, which is presented in Chapter 3.

In a resting state without external currents ($J = 0$), the membrane potential is constant, therefore $\dot{V} = 0$ and so we arrive at the following expression for the membrane potential:

$$V_{\mathrm{rest}} = \frac{g_{\mathrm{Na}}E_{\mathrm{Na}} + g_{\mathrm{Ca}}E_{\mathrm{Ca}} + g_{\mathrm{K}}E_{\mathrm{K}} + g_{\mathrm{Cl}}E_{\mathrm{Cl}}}{g_{\mathrm{Na}} + g_{\mathrm{Ca}} + g_{\mathrm{K}} + g_{\mathrm{Cl}}}. \tag{1.6}$$

In this way, we see that the membrane voltage is the weighted arithmetic mean of the Nernst potentials with the respective conductances serving as weights.

We remark that the chosen convention is that the difference in electric potentials are taken as the potential inside minus the potential outside (Kandel et al., 2000). For example, membrane voltage is $V = V_{\mathrm{in}} - V_{\mathrm{out}}$. Following this, a positive current $J > 0$ corresponds to positive charge going out of the cell. Table 1.1 shows values of Nernst potentials for the main ionic species, according to (Izhikevich, 2007) (these values can of course vary in different neurons). We see that negative, also called inward, currents are due to Sodium (Na^+) and Calcium ($Ca_2{}^+$), while positive, outward, currents are due to Potassium (K^+) and Chloride (Cl^-). Therefore, inward currents make the membrane potential more positive, and outward currents make it more negative. In other terms, inward currents depolarize the membrane (increase V), while outward currents hyperpolarize it (decrease V).

Ionic species	Nernst potential
Na^+	61 mV to 90 mV
K^+	−90 mV
Cl^-	−89 mV
$Ca_2{}^+$	136 mV to 146 mV

Table 1.1: Nernst potentials for the main ionic species of neurons (Izhikevich, 2007).

1.2.4 Conductances

Both ion channels and receptors can be in an open (allowing passage of ions) or closed (not allowing) state, with the transitions between open and closed states being stochastic in nature, owing to thermal agitation (O'Donnell and van Rossum, 2014). These states are controlled by gating particles for some ion channels, which are in part dependent on the membrane voltage. In these voltage-gated channels the transition probabilities are dependent on the membrane potential.

However, despite this stochasticity between individual channels, the current in a large population can be described with some accuracy by the equation

$$J = \overline{g} p (V - E), \tag{1.7}$$

where $\overline{g}$ is the maximal conductance of the whole population of channels, p is the average proportion of open channels, and E is the Nernst potential of the current.

There are two types of gating particles: (i) activation gates, which activate (open) the channel; (ii) inactivation gates, which inactivate (close) the channel. These gates can also be in open or close states. The probabilities of the activation and inactivation gates to be in an open position are, respectively, m and h. We have 4 important combinations, which lead to open or close channels:

- open activation gates ($m = 1$), open inactivation gates ($h = 1$): open channel;
- open activation gates ($m = 1$), close inactivation gates ($h = 0$): close channel;
- close activation gates ($m = 0$), open inactivation gates ($h = 1$): close channel;
- close activation gates ($m = 0$), close inactivation gates ($h = 0$): close channel.

For channels types with a activation gates and b inactivation gates, the proportion of channels in open states can be written as (Izhikevich, 2007)

$$p = m^a h^b. \tag{1.8}$$

Therefore, m and h determine p and, as a result, the conductance g. Continuing our modelling, we define $\alpha_m(V)$ and $\beta_m(V)$ as the rates of the gate transitions from closed to open and from open to closed, respectively, for the variable m. Then, the rate at which the probability of the channel being open changes is:

$$\dot{m} = \alpha_m(V)(1 - m) + \beta_m(V)m. \tag{1.9}$$

This is the difference between the probability of the gate opening minus the probability of it closing. The probability that the gate opens in a short interval of time is equal to the probability of the gate being closed $(1 - m)$ times the opening rate (α_m); conversely, the probability that the gate closes in a short interval is equal to the probability of it being open (m) times the closing rate (β_m).

As a remark, we note that with a change of variables the previous equation can be written as

$$\tau_m(V)\dot{m} = m_\infty(V) - m, \tag{1.10}$$

where $\tau_m(V)$ is the characteristic time of variable m and $m_\infty(V)$ is the limiting value of m.

The rates α_m and β_m can then be found experimentally. The same idea can be applied to the inactivation variable h. Therefore, we finish the description of the ion channel conductance and have all the ingredients for the Hodgkin-Huxley model, the nobel-winning description of a neuron (Hodgkin and Huxley, 1952), which is described in chapter 3.

1.3 SPIKE GENERATION

In the previous section we studied the electrochemical properties of the neuron, which allow for its mathematical description. In this section, we describe a simple mechanism for generating a spike, also called an action potential, which is a fast transient change in the membrane voltage V of the neuron.

At rest, also called the neuron's quiescent period, the membrane potential is constant and the fluxes of the ions balance each other. In this case, the conductances are such that the membrane potential is at the rest value V_{rest}, described in Eq. 1.6.

For an action potential to be initiated, the membrane potential has to increase (i.e. the neuron has to be depolarized) beyond a threshold (Kandel et al., 2000). With this increase, the conductance of Na^+ increases rapidly, which leads to an increase in the inward Na^+ current, which further depolarizes the neuron. While the potential goes up, Na^+ inactivation gates start to close, decreasing the inward Na^+ current and also K^+ activation gates start to open, increasing outward K^+ current. In this case, the membrane potential reaches a maximum at a value close to $V \approx 55\,\text{mV}$. At this point, Na^+ current is very small, since the channel is closed, but K^+ is still significant, decreasing V. The process up to now is called depolarization of the membrane.

After this, K^+ channel continues open, and K^+ closed, driving the membrane potential below the rest potential. This is called a hyperpolarization. Around this time, Na^+ channels start to reopen, leading to inward currents which start to lead the voltage up to the rest potential.

We therefore see that spike generation is due to the temporal changes in the conductances of, mainly, Na^+ and K^+ channels (corresponding to the opening and closing of activation and inactivation channels).

The experimental observations reveal the action potential is a all-or-none process, meaning that initially the membrane depolarization has to go above a certain threshold in order for the whole process to happen. If the depolarization does not pass the threshold, the neuron simply repolarizes back to the rest potential. But, if it does pass the threshold, the amplitude and duration of the action potential changes very little with stimulus intensity.

Also, neurons pass through two types of refractory periods after the action potential. During hyperpolarization, even a very strong stimulus is incapable of generating a spike in the neuron, because the Na^+ current is still inactivated and the initial positive feedback process cannot happen. This is called an absolute refractory period. However, a bit after hyperpolarization, spikes can be generated, but the stimulus strength is higher than initially, because Na^+ currents are not still at their former level. This is called a relative refractory period (Izhikevich, 2007).

1.4 SYNAPSES

In this section we now describe briefly the main mechanisms involving neuronal connections. In general, neurons may be connected either electrically - via gap junctions -, or chemically - via special molecules called neurotransmitters. In both cases, the structure connecting the two neurons is called a synapse (Kandel et al., 2000; Brown, 1991). In the chemical synapse (Fig 1.4), neurons are separated in space by a synaptic cleft, with the sending

neuron being called a presynaptic neuron ("before synapse") and the receiving one being the postsynaptic ("after synapse") neuron.

The action potential in the presynaptic neurons activates voltage-gated calcium channels, which may lead to the release of neurotransmitters into the synaptic cleft. Neurons have a probability of release that is not necessarily 1. The release probability is an important factor in determining the synaptic strength.

The released molecules are then diffused until they reach receptors in the postsynaptic neurons. In a common type of receptor, neurotransmitters bind to the receptors, causing changes in ion channel conductances, leading to ionic currents (Kandel et al., 2000). These generate postsynaptic potentials, which are excitatory (EPSP, for Excitatory Postsynaptic Potential) if they increase probability of action potential generation, or inhibitory (IPSP, for Inhibitory Postsynaptic Potential), if they decrease the probability. These effects depend on the receptor and neurotransmitter types. An EPSP may then lead to an action potential, if its effect is sufficiently strong (Kandel et al., 2000; Brown, 1991).

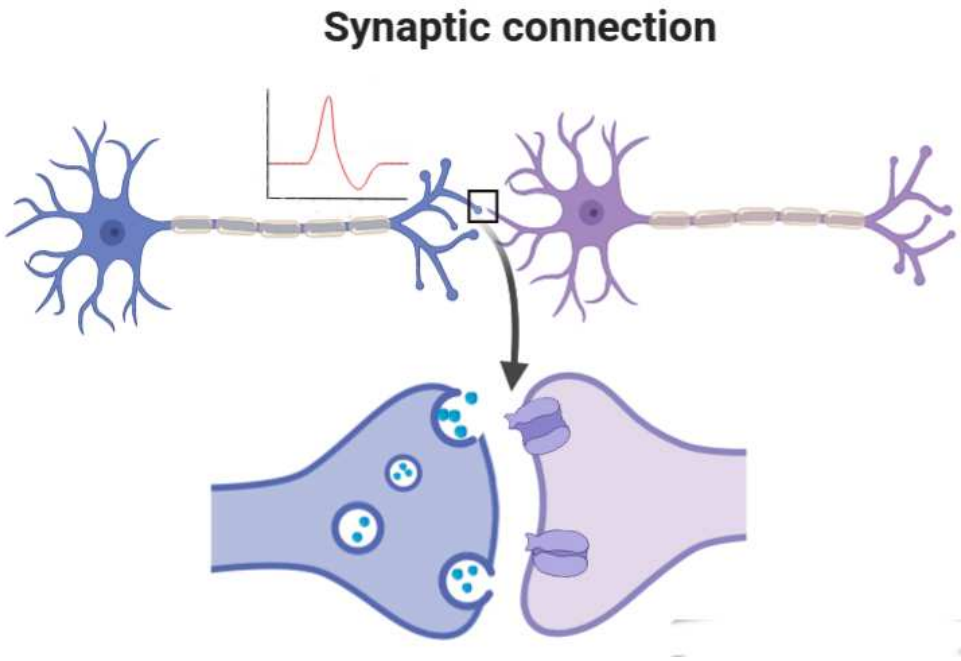

Figure 1.4: **A chemical synaptic connection between two generic neurons.** The presynaptic neuron (left) releases neurotransmitters (cyan circles) to the synaptic cleft (space between the two neurons), which then diffuse until reaching the postsynaptic neuron (right) and binding to its receptors embedded in the membrane.

1.5 BURSTING NEURON

There is another mode of firing called burst, characterized by a fast sequence of spikes followed by a long period of silence, as shown in Figure 1.5. Most neurons are capable of firing bursts, if stimulated appropriately (Izhikevich, 2006), but, also, many neurons fire bursts intrinsically. Examples are ubiquitous in the nervous system (Fox et al., 2015), like endocrine cells, respiratory pacemaker neurons, thalamic relay cells, pyramidal neurons in the neocortex (Coombes and Bressloff, 2005) and neurons in the Botzinger complex (involved with the respiratory rhythm) (Butera et al., 1999).

1.5.1 Importance

Bursts are hypothesized to have various advantages (compared to single spikes) for neural computation (Izhikevich, 2006; Swadlow and Gusev, 2001) due to their higher capability of generating responses on postsynaptic neurons (Swadlow and Gusev, 2001; Csicsvari et al., 1998). For example, they are more reliably transmitted to postsynaptic neurons (Lisman, 1997), have more informational content (Reinagel et al., 1999), and have higher signal-to-noise ratio (generation of bursts require stronger stimulation) (Sherman, 2001). Bursting is also the most common mode of firing in central pattern generators, networks that generate rhythmic motor activity (Fox et al., 2015; Kandel et al., 2000).

1.5.2 Physiological mechanisms

Bursting is composed of oscillations at two time scales: a fast spiking oscillation that is modulated by a slow oscillation. One can think of bursting as repetitive spiking that is periodically terminated by the slow oscillations (Izhikevich, 2007): while the neuron fires, some processes start to occur that reduce its excitability until it no longer fires. Then, during quiescence, the neuron recovers and regains its excitability. The processes can be (i) slow increase of an outward (hyperpolarizing) current or (ii) slow decrease of an inward current needed for spiking (Izhikevich, 2007). Moreover, these currents can be (i) voltage-gated or (ii) Ca^{2+}-gated. These 4 types of currents are described in (Izhikevich, 2007), but we focus here on the voltage-gated slow increase (activation) of an outward current since that is the case of the Huber-Braun model we use in this dissertation.

In this case, the repetitive firing activates the outward current, which hyperpolarizes the neuron and reduces its excitability until it can no longer fire. This current then deactivates during rest, allowing another burst. An example of such a current is a persistent (non-inactivating) K^+ current like the M-current (Izhikevich, 2007). Also, example of neurons with these voltage-gated activation of outward currents are neocortical chattering neurons (Wang, 1999) and neurons in the pre-Botzinger complex (Butera et al., 1999).

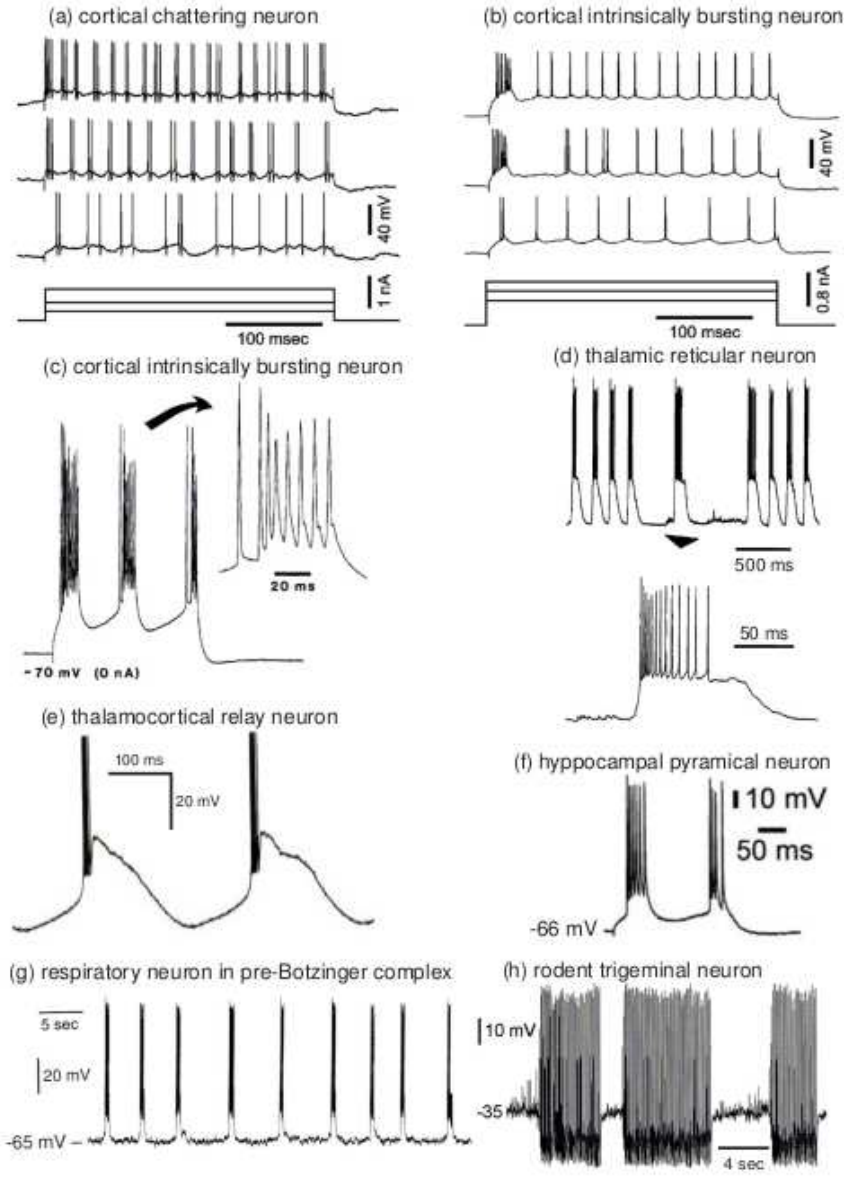

Figure 1.5: **Examples of intrinsically bursting neurons.** Figure is taken from (Izhikevich, 2007), with panels (a) and (b) showing recordings from neurons in the cat primary visual cortex taken by (Nowak et al., 2003), panel (c) showing neurons in the cortex of an anesthetized cat made (Timofeev et al., 2000), (d) from the reticular thalamic nucleus (Steriade, 2003); (e) a cat thalamocortical relay neuron (McCormick and Pape, 1990); (f) a CA1 pyramidal neuron (Su et al., 2001); (g) neuron in the pre-Botzinger complex (Butera et al., 1999); (h) trigeminal interneuron from brainstem of rats (Del Negro et al., 1998).

1.6 NEURONAL VARIABILITY

The neuronal responses may be highly variable across time and trials. This variability is observed in all types of electrophysiological recordings across the central nervous system (Nawrot et al., 2008; Shadlen and Newsome, 1994), with different degrees in different areas and levels. For example, variability of single neurons increases at higher stages of sensory processing (Kara et al., 2000) and is higher in the motor cortex if compared to the periphery (Prut and Perlmutter, 2003). This suggests a role for it in information processing. Indeed, since neural codes usually depend on firing rates or spike timing (Stein et al., 2005; Quiroga and Panzeri, 2013; Rieke et al., 1999), variability is a very important phenomenon, and may be either noise

or a part of the signal (Stein et al., 2005). Therefore, understanding variability is crucial for understanding the neural code (Nawrot et al., 2008; Stein et al., 2005; Movshon, 2000).

Neuronal variability may be divided roughly in two types: neuron-intrinsic and neuron-extrinsic (Nawrot, 2010; Deweese and Zador, 2004), meaning variability generated internally in the neuron or externally by its connections. In the former, it may for example be due to synaptic failures, to noise in the dendritic integration while, in the latter, it is generated by the spatiotemporal patterns of inputs to the neuron, coming from external connections.

1.7 PHASE SYNCHRONIZATION

Neurons can be regarded as (nonlinear, complex) oscillators. As such, we can ascribe a phase ϕ to their oscillation, measuring where in the oscillation the current state of the neuron is. Thinking of the phase as an angle (Pikovsky et al., 2002), we can imagine that, for example, just after a spike (or burst), the phase is $\phi = 0$ and it starts increasing with time to $\phi = \pi$ between this first spike and the second and $\phi = 2\pi$ just after the second spike (the precise definition is given in Section 5.6). At the network level, phases can also be defined for the network oscillations.

In biological systems, phases are often correlated between neurons or even between networks of neurons, with the phase differences being constant for periods of time (Fell and Axmacher, 2011) in what is known as phase-locking (Pikovsky et al., 2002). In some works, this is usually considered to be the same as phase synchronization (PS) (Lachaux et al., 1999; Aydore et al., 2013). However, in works focused on nonlinear dynamics, and in this dissertation, this is not the case. We refer to PS as the phenomenon in which there is phase-locking with the additional restriction of equal phases.

The phenomena of phase-locking and phase synchronization are crucial widespread mechanisms for the functioning of the nervous system (Fell and Axmacher, 2011; Lowet et al., 2016; Buschman and Miller, 2007; Colgin et al., 2009). They are observed in healthy systems in various cognitive processes (Engel et al., 2001; Fries et al., 2007; Cavanagh et al., 2009), such as memory (Fell and Axmacher, 2011), consciousness (Gaillard et al., 2009; Dehaene et al., 2014; Melloni et al., 2007), visual-motor behavior (Roelfsema et al., 1997) and perception (Rodriguez et al., 1999). Moreover, their disruption (lack or excess) is also observed in unhealthy systems (Uhlhaas and Singer, 2006; Uhlhaas et al., 2009), such as in epileptic episodes (Mormann et al., 2000), Parkinson's disease (Galvan and Wichmann, 2008) and autism (Dinstein et al., 2011).

The putative importance of PS for neural communication has theoretical reasons, explained for example in the influential ideas of binding-by-synchrony (Singer, 1999) and communication-through-coherence (CNC) (Fries, 2005, 2015).

To understand the first idea, imagine two neural assemblies (e.g. brain areas), each with its own representation of a certain piece of information (defined by the spatiotemporal pattern of activation) (Fries, 2015). For these two areas to communicate (i.e. transfer their representation), they can simply synchronize their oscillations in phase. For example, thinking about sensory information, PS can establish transient associations between different brain regions that represent certain attributes of a stimulus (Fell and Axmacher, 2011). In this way, PS has a binding function, linking different representations being processed in different areas (Fell and Axmacher, 2011; Fries, 2015; Singer, 1999). This binding may be very important, for example, in consciousness (Engel et al., 1999).

The second idea is based on the observation that the spike probability of neurons is dependent on the phase of the network oscillation (Buzsáki and Draguhn, 2004; Fries et al., 2007): during an oscillation cycle, some periods facilitate neuronal spiking (enhancing neuronal excitability), while others hinder it (reducing excitability). This makes it so that, in order

for two networks to communicate (exchange information) effectively, their oscillation phases have to be aligned (i.e. coherent). This is the idea of the communication-through-coherence hypothesis (Fries, 2005, 2015). A very interesting example of CNC is in (Womelsdorf and Fries, 2007), where attention is shown to regulate which neuronal groups phase synchronize and thus, communicate more effectively. The authors argue that selective PS may be a general mechanism for dynamically controlling which neurons communicate effectively.

Another example of the importance of synchronization is in (Gonzalez et al., 2019). The authors studied how neuronal representations change in time and with damage in the hippocampus and showed that information stored in individual neurons is labile, but information in networks of synchronized neurons is much more reliable.

1.8 BRAIN SCALES

The brain, like many other complex systems, has multiple scales of behavior and anatomy. Following (Betzel and Bassett, 2017), we identify three types of scales: (i) spatial; (ii) temporal; (iii) topological. For each scale, we describe possible observations and measurements to illustrate how they can be put in different depth levels.

1.8.1 Spatial scale

This refers to the ”granularity at which its [the network’s] nodes and edges are defined" (Betzel and Bassett, 2017). Can range from a micro level, with individual cells and synapse or voxels (in MRI studies); to meso, with neuronal populations or clusters; to macro, like brain regions and large-scale fiber tracts.

1.8.2 Temporal scale

This scale refers to the time duration and characteristic times for the processes in the networks. Both functional and structural networks are not static, but fluctuate over time. One can identify the following timescales, for example: (i) cellular (micro): $10 - 100$ ms; (ii) meso: large-scale integration of neural areas - $100 - 300$ ms; (iii) macro: long-range integration, ($1 >$ s). In a "supermacro" scale, one could also identify life-long processes and even evolutionary ones (Betzel and Bassett, 2017).

1.8.3 Topological scale

This refers to the views of the network (also called graph, cf. Chapter 4). The different levels can be identified as (i) micro: individual nodes (e.g. node’s degree) or a few nodes (e.g. pairwise interactions); (ii) meso: several nodes (e.g. community structures, cores, peripheries, rich clubs); (iii) macro: whole network properties (e.g. characteristic path length, global properties of the network).

An important step in understanding the whole system is to understand these different scales, and levels, and the interactions between them. Specifically, for example, how properties at one scale are related to properties at another scale (Betzel and Bassett, 2017). One important point in this dissertation goes in this vein, by studying the metastable behavior (cf. Chapter 6) at different scales and levels.

Figure 1.6, taken from (Betzel and Bassett, 2017), illustrates the three scales, along with examples of the different levels for each case.

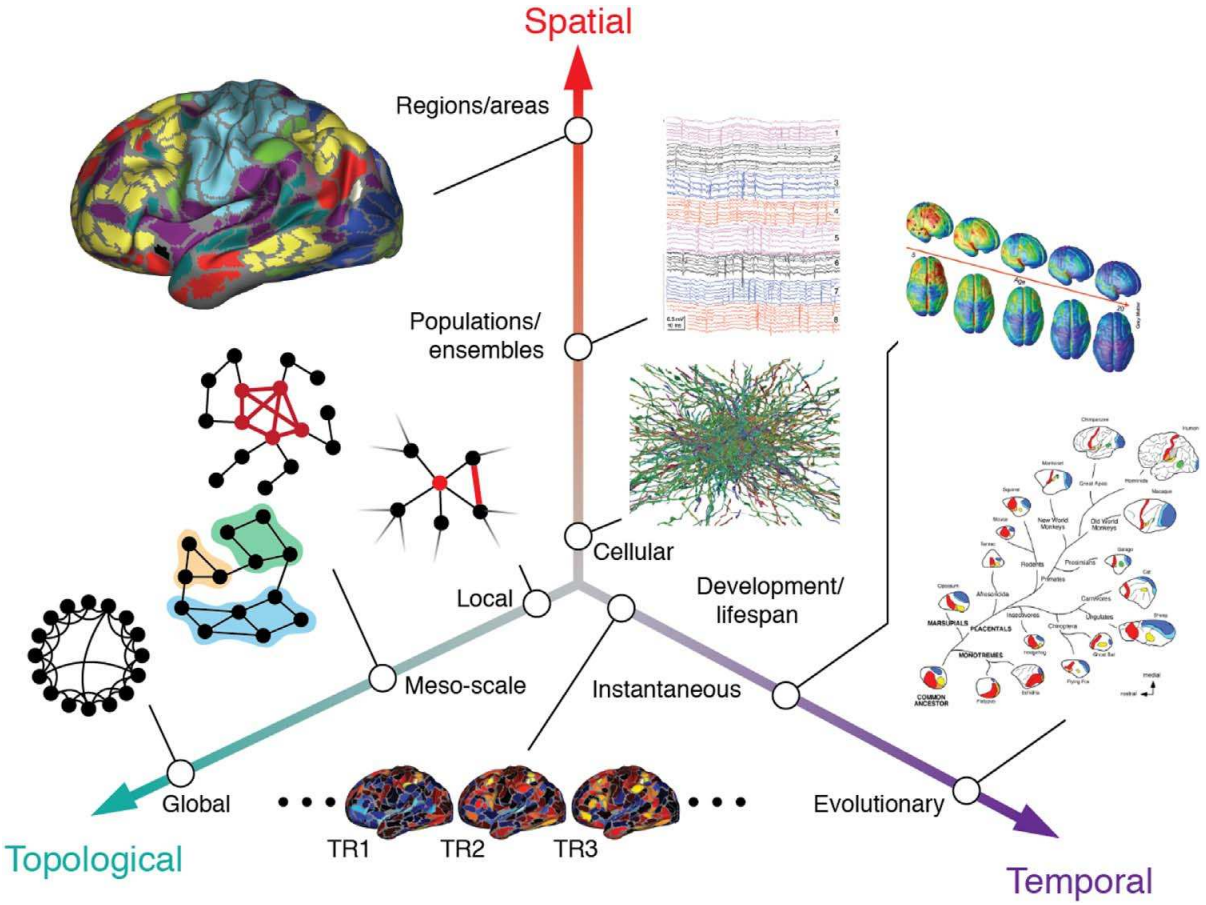

Figure 1.6: **Brain scales.** Three axes representing the three brain scales: spatial, temporal and topological. Image taken from (Betzel and Bassett, 2017). Spatial scale ranges from molecules to cells to neural populations and to brain areas; temporal scale range from almost millisecond to hundreds of milliseconds to seconds and even lifetimes; topological scale ranges from individual nodes to clusters to the whole network.

1.9 FORMATION OF NEURONAL GROUPS

In the brain, neurons tend to organize themselves: from the macroscopic brain regions (Kandel et al., 2000; Ding et al., 2016), to anatomical clusters in microcircuits (Perin et al., 2011; Klinshov et al., 2014). In this latter, for example, research in the neocortex shows that the probability of any two neurons being connected increases the more neighbors in common they have (Perin et al., 2013), accounting for the small-world properties observed throughout the brain (cf. Section 4.2.3). Small-world topology is another example, for one of its defining features is high clustering (Watts and Strogatz, 1998). These anatomical properties are also subject to change, as several mechanisms for brain plasticity exist (Abbott and Nelson, 2000; Kandel et al., 2000; Dayan and Abbott, 2005; Schaefer et al., 2017; Watt and Desai, 2010), making anatomy dependent on dynamics.

Dynamics of course also depends on anatomy (Sporns, 2013; Klinshov et al., 2014). In the dynamics, neurons can organize themselves functionally, meaning the activity of neural populations can be organized into clusters too (Berry and Tkačik, 2020; Dombeck et al., 2009; Tononi et al., 1998a) (as a curious remark, this organization into clusters is so robust it has been proposed as a way the brain can code information (Berry and Tkačik, 2020)). These clusters, or neural assemblies, emerge and disband constantly and much more quickly than the anatomy changes. They are said (Shine et al., 2016) to form the basis for complex cognitive functions

(Bassett et al., 2015), learning (Bassett et al., 2011, 2015) and even consciousness (Barttfeld et al., 2015).

Another important example on the importance of neural clusters is captured by the idea that "For every cognitive act, there is a singular and specific large cell assembly that underlies its emergence and operation" (Le Van Quyen, 2003). This is related to the Dynamic Core Hypothesis (Tononi et al., 1998a), according to which each conscious experience is associated to a transient assembly of neurons (the dynamic core) (Cavanna et al., 2018). Neurons in the dynamic core can be interacting intensely between themselves, while still being separated from the rest of the network as these processes, though influenced, are not restricted by the anatomy (Werner, 2007b).

2 DYNAMICAL SYSTEMS

In Chapter 1, we have encountered two very important systems: neurons, with their nonlinear, spike-generating behavior, and networks of neurons, with their complex, emergent phenomena that are in part the object of study of neuroscience. The behaviors of both systems can be better understood and described using the framework of dynamical systems theory, the object of study in this chapter. With the knowledge acquired here, we are then able to describe the mathematical models for neurons in Chapter 3, and better describe the behaviors of the networks we study in this dissertation, such as the mechanisms for metastability in Chapter 6.

2.1 DEFINITION AND INITIAL CONCEPTS

A dynamical system has two important components: (i) variables that describe its state and (ii) a law governing how these variables change in time (Izhikevich, 2007; Strogatz, 2018). The important example is the Hodgkin-Huxley neuron whose (i) variables are V, n, m, h and (ii) laws are the equations 3.1, presented in Chapter 3. The laws can be either differential equations (where the system is said to be a flow) or difference equations (where it is said to be a map). The cases studied in this dissertation are of the first type so, for completeness, we show the general formula of these laws:

$$\begin{aligned} \dot{x}_1 &= f_1(x_1, x_2, \ldots, x_n) \\ \dot{x}_2 &= f_2(x_1, x_2, \ldots, x_n) \\ &\vdots \\ \dot{x}_n &= f_n(x_1, x_2, \ldots, x_n). \end{aligned} \tag{2.1}$$

Alternatively, the dynamical system can also be put in vector form, for convenience:

$$\dot{\mathbf{x}} = \mathbf{f}(\mathbf{x}, t). \tag{2.2}$$

This system is said to be n-dimensional (and so is the vector $\mathbf{x}$). We can define an abstract space with coordinates $\{x_1, x_2, \ldots, x_n\}$, called phase space, where the solutions of the system can be visualized as trajectories (also called orbits) (Ott and Edward, 2002).

These orbits can be characterized according to their behavior under a small perturbation. If the perturbed orbit (which can also be viewed simply as a nearby orbit) returns (or tends to) the original orbit as it evolves, the original orbit is said to be stable; otherwise, it is unstable (Alligood et al., 1997).

2.2 LINEAR STABILITY ANALYSIS

Typically, the study of stability is done with infinitesimal perturbations $\delta\mathbf{x}$ from an original trajectory $\mathbf{x}$. In this case, the perturbation follows the linearized system of equations (Ott and Edward, 2002; Pikovsky, 2016), also called variational system of equations (Barreira, 2017):

$$\dot{\delta\mathbf{x}} = \frac{\partial \mathbf{f}}{\partial \mathbf{x}} \delta\mathbf{x}(t) = \mathbf{J}(\mathbf{x}, t)\delta\mathbf{x}(t), \tag{2.3}$$

where $\frac{\partial \mathbf{f}}{\partial \mathbf{x}} \equiv \mathbf{J}(\mathbf{x}, t)$ is the system's Jacobian. Explicitly,

$$\mathbf{J}_{ij} \equiv \frac{\partial f_i}{\partial x_j}. \tag{2.4}$$

Equation 2.3 can be obtained by writing the Taylor series expansion of the functions $\mathbf{f}$ and keeping only first order (linear) terms (Ott and Edward, 2002; Strogatz, 2018). One can obtain an analytic solution to the linear system by integrating it, obtaining the solution for the initial condition $\delta\mathbf{x}(0)$

$$\delta\mathbf{x}(t) = \mathbf{H}(\mathbf{x}_0, t)\delta\mathbf{x}(0), \tag{2.5}$$

where $\mathbf{H}(\mathbf{x}_0, t) = \exp\left(\int_0^t dt' \mathbf{J}(\mathbf{x}(\mathbf{t}'), \mathbf{t}')\right)$ is the generator of the evolution of the linear system, and, importantly, depends on the trajectory of the original system. Though we write it explicitly here, in practice it is obtained by numerical integration of the linear differential equations (Pikovsky, 2016).

For fixed-point solutions (where $\mathbf{f}(\mathbf{x}) = 0$), stability can be assessed through the eigenvalues of the Jacobian. In general, for non-periodic trajectories, the stability can be studied through the Lyapunov exponents, which are described next.

2.3 LYAPUNOV EXPONENTS

2.3.1 Introduction and definition

As a rough introduction, the Lyapunov exponents (LE) measure the rate of divergence (or convergence) of the nearby perturbations. The number of LEs is the dimension of the system and the set of all exponents is the Lyapunov *spectrum*. A characteristic of chaotic systems, in which nearby trajectories diverge exponentially, is that the maximum Lyapunov exponent is positive.

We are interested in how the amplitude of the perturbation $\delta\mathbf{x}$ changes. We can write it as

$$|\delta\mathbf{x}(t)|^2 = |\mathbf{H}\delta\mathbf{x}(0)|^2 = \delta\mathbf{x}^T(0)\mathbf{H}^T(t)\mathbf{H}(t)\delta\mathbf{x}(0), \tag{2.6}$$

where $(\cdot)^T$ denotes the transpose of either a vector or a matrix. Therefore, the amplitude of the perturbation is dependent only on the properties of the matrix

$$\mathbf{M}(t) = \mathbf{H}^T(t)\mathbf{H}(t), \tag{2.7}$$

which is real and symmetric. A very important property is given by Osedelets theorem (Pikovsky, 2016), according to which if the process $\mathbf{x}$ is ergodic, then the limit

$$\mathbf{P} \equiv \lim_{t\to\infty} (\mathbf{M}(t))^{\frac{1}{2t}} \tag{2.8}$$

exists and is a N-dimensional matrix with positive eigenvalues $\mu_1 \geq \mu_2 \geq \cdots \geq \mu_N$. As we see next, the N Lyapunov exponents are defined as

$$\lambda_k = \log \mu_k. \tag{2.9}$$

As a side note, an equivalent definition for the Lyapunov exponents (Pikovsky, 2016) is given in terms of the linear evolution of the perturbations. In this case, the growth rate of any initial perturbation $\delta\mathbf{x}$ is one of the Lyapunov exponents

$$\lambda_k \equiv \lim_{t\to\infty} \frac{1}{t} \ln \frac{|\delta\mathbf{x}(t)|}{|\delta\mathbf{x}(0)|} = \lim_{t\to\infty} \frac{1}{t} \ln \frac{|\mathbf{H}(t)\delta\mathbf{x}(0)|}{|\delta\mathbf{x}(0)|}. \tag{2.10}$$

To which of the Lyapunov exponents this equation corresponds depends on the original perturbation $\delta\mathbf{x}(0)$.

2.3.2 Volume contraction

To understand the first definition, we need to first study how volumes in phase space typically behave. First, define m orthogonal vectors $\mathbf{v_i}$, $i = 1, \ldots m$, defining a parallelepiped with volume $V(0)$. These vectors correspond to perturbations $\delta\mathbf{x}$. As they evolve, under the linearized system, through Eq. 2.5, the volume $V(t)$ at each time t is

$$V_m(t) = V_m(0) \left|\det \mathbf{H}\right|, \tag{2.11}$$

where H is the generator of the evolution

$$\mathbf{H} = \exp \int_0^t dt' \mathbf{J}(\mathbf{x}(t'), t'). \tag{2.12}$$

Therefore, the growth rate S_m can be written as

$$S_m \equiv \lim_{t\to\infty} \frac{1}{t} \ln \frac{V_m(t)}{V_m(0)} = \lim_{t\to\infty} \frac{1}{t} \ln \left|\det \mathbf{H}\right|. \tag{2.13}$$

Also, from Eq. 2.8, using properties of determinants

$$\ln \det \mathbf{P} = \lim_{t\to\infty} \ln \det \left(\mathbf{M}\right)^{(1/2t)} \tag{2.14}$$

$$= \lim_{t\to\infty} \ln \left(\left|\det \mathbf{H}^{1/t}\right|\right) \tag{2.15}$$

$$= \lim_{t\to\infty} \frac{1}{t} \ln \left|\det \mathbf{H}\right|. \tag{2.16}$$

From Linear Algebra we know that the determinant of a matrix is equal to the product of its eigenvalues:

$$\ln \det \mathbf{P} = \sum_{i=1}^{m} \ln \nu_i = \sum_{i=1} \lambda_i, \tag{2.17}$$

where the last equality comes from the definition of the Lyapunov exponents as $\lambda_i \equiv \ln \nu_i$. Therefore, we have

$$S_m = \sum_{i=1}^{m} \lambda_i. \tag{2.18}$$

This relation is the key for the numerical estimation of Lyapunov exponents, as we see next.

2.3.3 Numerical estimation

To obtain the full spectrum of Lyapunov exponents we can estimate the growth rate S_m of the volume V_m of an m-dimensional parallelepiped. To do this, we define m N-dimensional orthogonal vectors living in the tangent space, which are treated as perturbations $\delta\mathbf{x}$. These vectors form an $N \times m$ orthogonal matrix $\mathbf{Q}_0$ and define the parallelepiped. After some time t, these vectors evolve according to the solution of the linearized system, so the matrix $\mathbf{Q}_0$ turns into $\mathbf{P}$ according to:

$$\mathbf{P}(t) = \mathbf{H}(t)\mathbf{Q}_0, \tag{2.19}$$

and the volume of the parallelepiped changes following Eq. 2.18. Now, the matrix P can be uniquely decomposed into

$$\mathbf{P}(t) = \mathbf{QR}, \tag{2.20}$$

following the QR-decomposition from Linear Algebra, where $\mathbf{Q}$ is an $N \times m$ orthogonal matrix and $\mathbf{R}$ is an $m \times m$ upper triangular matrix whose diagonal elements are positive. It can be shown (Pikovsky, 2016; Barreira, 2017) that the volume depends only on the determinant of $\mathbf{R}$, which, being a triangular matrix, leads to

$$V_m(t) = V_m(0) \prod_{i=1}^{m} R_{ii}. \tag{2.21}$$

Substituting this into 2.18 we arrive at

$$\lambda_i = \lim_{t\to\infty} \frac{1}{t} \ln R_{ii} \quad i = 1, \ldots, m. \tag{2.22}$$

This is the basis of the QR-decomposition method for numerical calculations of the Lyapunov spectrum, with more details provided in (Pikovsky, 2016). We remark that the common way to implement the QR-decomposition is through the Gram-Schmidt orthogonalisation.

2.4 CHARACTERIZING ATTRACTORS

Now we move our focus from linear stability of trajectories to their long-time behavior: we study attractors of trajectories. Attractors are very important in the theory of dynamical systems, and have various different definitions. The general idea, however, is always similar: they are regions (sets of points) in phase space to which trajectories tend as they evolve. In other words, given some initial trajectories, their evolution tend to the attractor as time goes on. This is represented in Fig 2.1, where the blue points represent points in the attractor, and red points are the ones evolving on the attractor. Each panel corresponds to different instants in time, starting from a very small initial region. This attractor is the one for the Lorentz system (Strogatz, 2018), which for the parameters used here has divergence of nearby trajectories, which can also be seen in the figure.

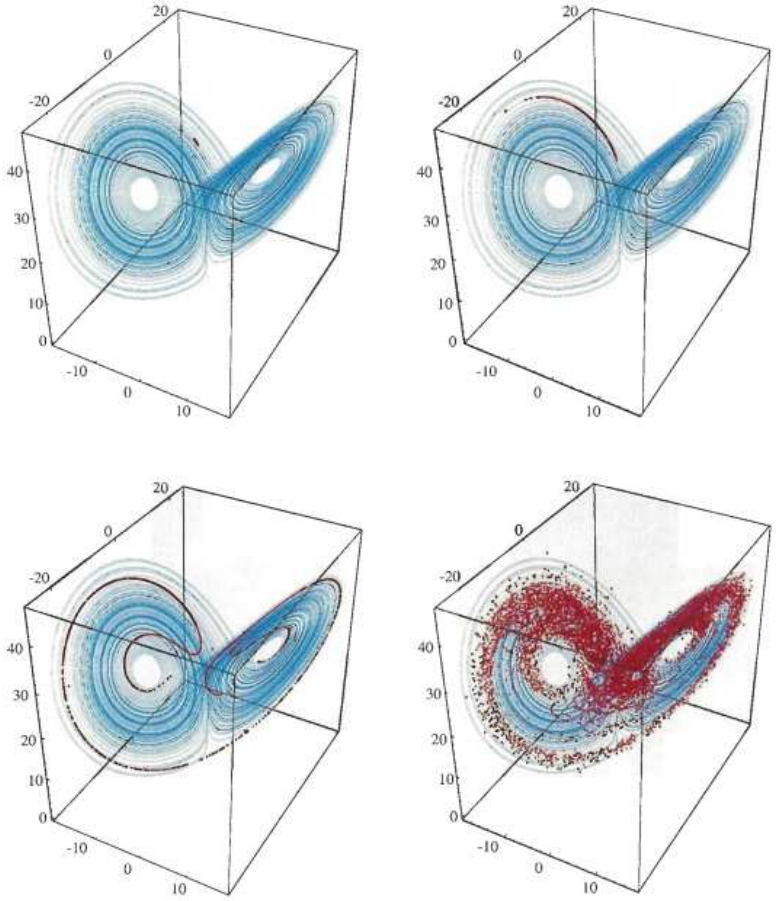

Figure 2.1: Trajectories (red points) evolving on the Lorentz attractor (blue points). Different panels correspond to different times, and the divergence of nearby trajectories can be easily seen. Figure is taken from (Strogatz, 2018).

We now focus on a robust definition of attractor, but first need to first introduce basins of attraction.

2.4.1 Basin of attraction

Roughly, the basin of attraction $\mathcal{B}(A)$ of an attractor A is the set of points which go to the attractor in the long term. A very intuitive mathematical definition, which depends on the concept of the omega limit set $w(x)$ of a point x, is present in (Milnor, 1985) and also given here. We define the ω-limit set of a point $\mathbf{x}_0$ as the set

$$\omega(\mathbf{x}_0) = \{\mathbf{x} : \forall\, T\ \forall \epsilon > 0 \text{ there exists } t > T \text{ such that } |f(\mathbf{x}_0, t) - \mathbf{x}| < \epsilon\}. \tag{2.23}$$

This means, for example, that for a point $\mathbf{x}$ in the set of $\mathbf{x}_0$ ($\mathbf{x} \in \omega(\mathbf{x}_0)$), the trajectory passing through $\mathbf{x}_0$ passes arbitrarily close to $\mathbf{x}$ infinitely often as t increases. Also, $\omega(\mathbf{x})$ can be, as the name says, a set of points, not just one point.

Then, Milnor defines the realm of attraction $\rho(A)$ as all points x for which $\omega(x) \subset A$. Note that this means only the long-term behavior of orbits is observed, and the transient could be anything (that is, points in the realm of attraction could go very far from A, as long as they go back to it and stay there eventually). Finally, if the realm of attraction $\rho(A)$ is an open set, then it is called the basin of attraction of A, denoted $\mathcal{B}(A)$. If $\rho(A)$ is a lower dimensional smooth manifold, then it is called the stable manifold of A (Milnor, 1985).

2.4.2 Milnor attractor

A weaker version of the concept of attractor. A set A is a Milnor attractor (sometimes called an attracting set simply) if:

1. The basin of attraction $\mathcal{B}(A)$ has strictly positive measure (i.e., if $m(\mathcal{B}(A)) > 0$). This condition says that there is some probability that a randomly chosen point will be attracted to A (Milnor, 1985).

2. For any closed proper subset $A' \subset A$, the set difference $\mathcal{B}(A) \setminus \mathcal{B}(A')$ also has strictly positive measure. This condition ensures that any part of A plays an essential role (that is, you cannot choose a subset of A to which all points go to, leaving other parts of A unimportant) (Milnor, 1985; Taylor, 2011).

As a note, a set is said to be close if it contains all of its limit points (Milnor, 2006), and it is said to be proper if its size is not zero. The measure m is a measure equivalent to the Lebesgue measure (Milnor, 1985).

A Milnor attractor can also be proven to be invariant (i.e. $f(A, t) = A$) (Cao, 2004). Also, a Milnor attractor can be connected to unstable orbits that are repelled from the attractor (Érdi et al., 2004; Kaneko and Tsuda, 2003). In this case, it is unstable by arbitrarily small perturbations, though still globally attracting typical orbital points (Kaneko and Tsuda, 2003). Furthermore, the Milnor attractor does not have to attract all the points in its neighborhood, and there can also be orbits transiently go very far from the attractor, even if initially close, before eventually getting close to it.

Finally, a minimal Milnor attractor is one in which no proper subset of it is also an attractor. That is, a Milnor attractor is minimal if there is no strictly smaller closed set $A' \subset A$ for which $\rho(A')$ has positive measure (Milnor, 1985).

An important property is that, if A is a minimal attractor, then $\omega(\mathbf{x})$ is precisely equal to A for almost every point $\mathbf{x}$ in $\rho(A)$ (Milnor, 1985).

2.4.3 Attractor

An attractor is a Milnor attractor with an additional condition (Milnor, 2006; Taylor, 2011): we say that an attractor follows the conditions

1. Is a Milnor attractor.

2. Contains a dense orbit.

A dense orbit $\mathbf{x}$ in A is such that, for every point $\mathbf{a}$ in A there is a subsequence of $\mathbf{x}$ that converges to $\mathbf{a}$. Roughly, this means that the orbit is dense in A if its points pass close to every point in A. This condition ensures that the attractor is not the union of two smaller attracting sets (Milnor, 2006; Taylor, 2011).

2.4.4 Quasi-attractor or attractor-ruin

It is also useful for later to define here quasi-attractors, also called attractor-ruins (Kaneko and Tsuda, 2003; Tsuda and Umemura, 2003). These are attracting regions from which orbits can escape. They can be Milnor attractors, or conventional attractors (like previously defined) that lost stability, for example.

2.5 TYPES OF ATTRATORS

We can study now a brief over overview of different types of attractors.

2.5.1 Fixed points and equilibria

Fixed points (used for maps) and equilibria (for flows) are constant solutions. Mathematically, they are

$$\mathbf{x}_{n+1} = \mathbf{x}_n \quad \text{(maps)} \tag{2.24}$$

$$\dot{\mathbf{x}} = \mathbf{0} \quad \text{(flows).} \tag{2.25}$$

For a neuron, this corresponds to the resting state. For further reference, an equilibrium with at least one unstable direction is called a saddle. Also, an orbit connecting a saddle to itself is called a homoclinic orbit.

2.5.1.1 Stability of equilibria

There are many definitions of equilibria. Here we present a simple one that is sufficient for getting the intuition behind the concept. Namely, this is the Lyapunov stability, that, simply defined, says that a point $\mathbf{x}$ (or an equilibrium) is stable if nearby orbits stay near. That is, if and only if for all $\epsilon > 0$ there exists a $\delta > 0$ such that if $|\mathbf{x} - \mathbf{y}| < \delta$ then $|f(\mathbf{x}, t) - f(\mathbf{y}, t)| < \epsilon$ for all $t \geq 0$ (Glendinning, 1994).

2.5.2 Periodic orbits

Periodic orbits are attractors that repeats in time. Mathematically, a non-constant solution $\mathbf{x}(t)$ is such that, for $T > 0$

$$\mathbf{x}(t + T) = \mathbf{x}(t), \tag{2.26}$$

where the minimal T is called the period of the solution. A periodic orbit is, then, the set of points that are mapped during the interval $[0, T]$ (it is the image of the interval under $\mathbf{x}$) (Glendinning, 1994). A two-dimensional periodic orbit is a limit cycle. For a neuron, this corresponds to periodic firing.

2.5.3 Stability of periodic orbits

Again, a simple view of stability of periodic orbits comes from taking their Poincaré surface of sections. Taking the periodic orbit, a surface transversal to the flow is defined (the Poincaré section) and we register the intersections of the orbit with the surface, generating the Poincaré map (Strogatz, 2018). The periodic orbit is a fixed point in this map, so the stability analysis is the same in this case.

2.5.4 Chaotic attractors

Nonlinear systems can have solutions that are not periodic, but are still bounded in space. In this case, nearby trajectories diverge (separate) rapidly in time. In other words, the system is very sensitive to the initial conditions. These solutions are called chaotic, forming chaotic

attractors, and are very important for the understanding of nonlinear dynamical systems. The geometric structure of the solutions is very complicated, so proper rigorous analysis are often too difficult to perform. One important result, following the Poincaré-Bendixon Theorem, is that chaos is only possible in flows of dimension 3 upwards (for maps, dimension 1 already suffices) (Glendinning, 1994; Strogatz, 2018). In neurons, this naturally corresponds to chaotic firing.

2.6 BIFURCATIONS

Depending on the parameters, a dynamical system may have all three of the above attractors, stable or not, simultaneously or not. When the system changes drastically its qualitative behavior as one parameter is changed, we say a bifurcation has taken place. This can lead, for example, from an equilibrium to a periodic orbit.

As we have seen from the linear stability analysis, if the stationary point is hyperbolic, then the local behavior is determined by the linearized flow. Following from this is that small perturbations from this point are also hyperbolic. Therefore, we have bifurcations only for non-hyperbolic points (i.e. points with at least one eigenvalue that is zero or purely imaginary).

Now we describe some bifurcations that are relevant for this dissertation. This is done for equilibria (fixed points), but the general considerations also apply for periodic orbits.

2.6.1 Saddle-node (fold) bifurcation

In a saddle-node bifurcation two equilibria (one stable and the other unstable) coalesce and annihilate each other. Therefore, this bifurcation deals with the creation (and destruction) of stable and unstable equilibria. In this case, one equilibrium had a negative eigenvalue and the other has a positive eigenvalue before bifurcation. At the bifurcation, these values reach 0 and later the points are destroyed (Strogatz, 2018). This scenario also occurs for periodic orbits (e.g. limit cycles).

Neurons passing through this bifurcation are of type II excitability (cf. Chapter 3), the exception being if the bifurcation occurs on an invariant circle (a saddle-node on invariant circle bifurcation), where the neuron has type I excitability (Izhikevich, 2007).

2.6.2 Andronov-Hopf

In an Andronov-Hopf bifurcation, a small-amplitude limit cycle is born from an equilibrium: it appears when the equilibrium disappears. In a supercritical bifurcation, the limit cycle is born stable (and the equilibrium loses its previous stability). In a subcritical, the inverse happens: the limit cycle is born unstable and the equilibrium gains stability. In this case, the Jacobian has a pair of complex eigenvalues whose real part becomes zero at the bifurcation.

Neurons passing through this bifurcation are of type II excitability (Izhikevich, 2007).

2.6.3 Homoclinic bifurcations

The homoclinic bifurcations also describe the appearance (or disappearance) of limit cycles (two-dimensional periodic orbits). The bifurcation is supercritical if the limit cycle is stable and supercritical if unstable. In the supercritical case, before the bifurcation there is a saddle and a stable limit cycle. At the bifurcation, these two touch each other, thereby making a homoclinic orbit (connecting the saddle to itself). After the bifurcation, the homoclinic orbit disappears (and the limit cycle already disappeared) and only the saddle remains. In the subcritical case the behavior is similar, but the limit cycle is unstable.

An important point is that the homoclinic orbit has infinite period (or zero frequency), so neurons passing through this bifurcation are of type I excitability (Izhikevich, 2007).

2.6.4 Period-doubling (or flip) bifurcation

This bifurcation deals with the destruction of a periodic orbit of period T and appearance of another of period $2T$. A cascade of period-doublings often occurs, leading to chaotic behavior (Ott and Edward, 2002). The inverse can also happen, leading from chaos to periodic behavior.

2.7 IMPORTANT DYNAMICAL PHENOMENA

Now, we talk briefly about dynamical phenomena which can lead to metastable dynamics, as later discussed in Section 6.3.2.

2.7.1 Chaotic itinerancy

Chaotic itinerancy is a trajectory in phase space connecting several quasi-attractors (also called attractor-ruins cf. Section 2.4.4). These are attractors in the sense that they attract trajectories, but "quasi" because the trajectories can escape them (Tsuda, 2013). Attractors can become quasi-attractors due to noise (Ansmann et al., 2016) or other mechanisms (Kaneko and Tsuda, 2003). In the chaotic itinerancy, then, a trajectory spends some time in one quasi-attractor, then leaves it to go to another one.

2.7.2 Unstable attractors

One possible strange phenomenon is that a Milnor attractor can be enclosed by the basins of attraction of other attractors, and also be remote from its own basin. In this case, arbitrarily small noise leads to trajectories switching attractors (Timme et al., 2002). Therefore, these attractors are called unstable attractors (Timme et al., 2002).

2.7.3 Heteroclinic cycles

A heteroclinic cycle is a sequence of several saddles linked to each other by their unstable manifolds (forming heteroclinic orbits) (Rabinovich et al., 2008; Afraimovich et al., 2008). Though each saddle is separately unstable, the cycle as a whole can be stable and attracting: trajectories initially are attracted to the cycle through the stable manifolds of the saddles and, once inside they hop from each saddle by their unstable manifolds. Each time the trajectory passes near a saddle, it gets closer to it, meaning passage times increase monotonically (beim Graben et al., 2019). A heteroclinic cycle can be considered an attractor, in the sense defined in Section 2.4.3.

2.7.4 Intermittency

There are several kinds of intermittency. We now describe some of them, following (Ott and Edward, 2002; Ott, 2006).

Pomeau-Maneville
Pomeu-Maneville intermittencies occur for no attractor, and are classified according to the bifurcation leading to them:

1. Type I: A saddle-node bifurcation (creation/destruction of periodic orbits, like fixed-points);

2. Type II: A subcritical Hopf bifurcation (creation/destruction of limit cycle);

3. Type III: Inverse period-doubling bifurcation (chaotic attractor turns into a period one and then into nothing).

On-off intermittency

On-off intermittency is an aperiodic switching between static, or laminar (i.e. periodic-like), behavior and chaotic bursts of oscillation. A before-stable attractor loses transverse stability, so the trajectory escapes from the attractor and returns later.

Crisis-induced

Interior-crisis: The chaotic attractor collides with an unstable periodic orbit that is contained within the interior of its basin of attraction. With this, the attractor increases its size. Therefore, the behavior is as follows: before the crisis, the system has a normal chaotic dynamics. After the crisis, it appears to have the same chaotic dynamics, but with occasional bursts outside the "normal-chaos" region. These bursts occur intermittently.

Symmetry-induced: In this type of crisis, at appropriate parameter values, due to a system symmetry, there are several distinct chaotic attractors that transform, one to the other, under a suitable symmetry transformation. As the crisis is approached, each of the symmetrically disposed attractors moves toward the basin boundary separating its basin from the basins of its symmetric neighbors. At the crisis, the attractors all simultaneously collide with an unstable periodic orbit on their respective basin boundaries. Just past the crisis, an orbit on the large, merged attractor spends long epochs on what appears to be one of the pre-crisis attractors, but then abruptly jumps to the state-space region of one of its neighboring pre-crisis attractors, spending another long epoch there, jumping, and so on, ad infinitum.

3 MODELLING NEURONS

With the biophysical and modelling knowledge acquired in Chapter 1 and 2 we plan now to present important concrete models for neurons. We start with the Hodgkin-Huxley model, whose formalism we already presented in part previously and which is the most accepted model for neuronal behavior (Izhikevich, 2007). Then, we present the Huber-Braun model, a modification of the Hodgkin-Huxley model, used in the dissertation.

3.1 HODGKIN-HUXLEY MODEL

At around 1950, Hodgkin and Huxley did experiments on neurons with very large axons in squids. These enabled them to observe that the axon had three major currents, which we already described: a voltage-gated inward Sodium J_{Na} current, a voltage-gated outward Potassium J_{K} and an Ohmic leak current J_{l} (carried out mostly by Cl^- ions). They also saw that the Sodium channel had three activation gates (variable m) and one inactivation gates (variable h), while the Potassium channel had four activation gates (variable n). With this knowledge, we can use the formalism previously described in chapter 1 to arrive at the Hodgkin-Huxley equations:

$$C_{\mathrm{M}}\dot{V} = J_{\mathrm{ext}} - \overline{g}_{\mathrm{K}} n^4 (V - E_{\mathrm{K}}) - \overline{g}_{\mathrm{Na}} m^3 h (V - E_{\mathrm{Na}}) - g_{\mathrm{l}} (V - E_{\mathrm{l}}) \tag{3.1}$$

$$\dot{n} = \alpha_n(V)(1 - n) - n\beta_n(V) \tag{3.2}$$

$$\dot{m} = \alpha_m(V)(1 - m) - m\beta_m(V) \tag{3.3}$$

$$\dot{h} = \alpha_h(V)(1 - h) - h\beta_h(V)\,, \tag{3.4}$$

where the variables represent the same quantities as defined previously, with $C_{\mathrm{M}} = 1\,\mu\mathrm{F/cm}^2$ and J_{ext} is an externally applied current density. The transition rates are also experimentally determined:

$$\alpha_n(V) = 0.01 \frac{10 - V}{\exp(10 - V)/V - 1} \tag{3.5}$$

$$\beta_n(V) = 0.125 \exp(-V/80) \tag{3.6}$$

$$\alpha_m(V) = 0.1 \frac{25 - V}{\exp(25 - V)/10 - 1} \tag{3.7}$$

$$\beta_m(V) = 4 \exp(-V/18) \tag{3.8}$$

$$\alpha_h(V) = 0.07 \exp(-V/20) \tag{3.9}$$

$$\beta_h(V) = \frac{1}{\exp(30 - V)/10 + 1}, \tag{3.10}$$

and the reversal potentials are $E_{\mathrm{K}} = -12\,\mathrm{mV}$, $E_{\mathrm{Na}} = 120\,\mathrm{mV}$, and $E_{\mathrm{l}} = 10.6\,\mathrm{mV}$, and maximal conductances are $\overline{g}_{\mathrm{K}} = 36\,\mathrm{mS/cm}^2$, $\overline{g}_{\mathrm{Na}} = 120\,\mathrm{mS/cm}^2$, and $\overline{g}_{\mathrm{l}} = 0.3\,\mathrm{mS/cm}^2$.

These are the original equations, in which parameters are changed such that the resting potential is at around 0 mV. As previously, a change of variables leads to the following equations

$$C_{\mathrm{M}}\dot{V} = J - \overline{g}_{\mathrm{K}} n^4 (V - E_{\mathrm{K}}) - \overline{g}_{\mathrm{Na}} m^3 h (V - E_{\mathrm{Na}}) - g_{\mathrm{l}} (V - E_{\mathrm{l}}) \tag{3.11}$$

$$\dot{n} = (n_\infty(V) - n)/\tau_n(V) \tag{3.12}$$

$$\dot{m} = (m_\infty(V) - m)/\tau_m(V) \tag{3.13}$$

$$\dot{h} = (h_\infty(V) - h)/\tau_h(V), \tag{3.14}$$

where p_∞, for $p = \{n, m, h\}$, are steady-state activation functions given by the equations

$$p_\infty(V) = \alpha_p/(\alpha_p + \beta_p), \tag{3.15}$$

which can be approximated by Boltzmann functions (Izhikevich, 2007):

$$p_\infty(V) = \frac{1}{1 + \exp{(V_{1/2} - V)/k}}, \tag{3.16}$$

where $V_{1/2}$ is called a half-activation potential, such that $m_\infty(V_{1/2}) = 0.5$, and k is the half-activation slope.

Also, characteristic times are

$$\tau_p = 1/(\alpha_p + \beta_p), \quad p = \{n, m, h\}. \tag{3.17}$$

The response of the state variables due to application of a step current are shown in Fig 3.1. For times before $t = 40$ ms, the injected current is $J_{\mathrm{ext}} = 0\,\mu\mathrm{A/cm^2}$ and the neuron is at rest. From 40 ms $< t <$ 42.5 ms, the current jumps to $J_{\mathrm{ext}} = 3\,\mu\mathrm{A/cm^2}$ and the neuron is slightly depolarized, but does not fire. At 50 ms $< t <$ 52.5 ms, a current of $J_{\mathrm{ext}} = 10\,\mu\mathrm{A/cm^2}$ is injected and the neuron fires an action potential. We therefore see that the current has to be sufficiently strong for an action potential to happen. Leaving the current constant at $10\,\mu\mathrm{A/cm^2}$ would make the neuron fire periodically. We can explore this further by studying the gain function of the HH model, displayed in Fig 3.2, in which the neuron's firing frequency is calculated as a function of the injected current.

The sudden jump from zero frequency (resting behavior) to spiking with non-zero frequency shows that the HH neuron is of type II excitability, as defined in (Hodgkin, 1948; Prescott, 2013).

3.2 HUBER-BRAUN MODEL

The formalism introduced by Hodgkin and Huxley can be applied to various other cell types to obtain different neuronal models. This was done by Huber and Braun (Braun et al., 1998) studying mammalian cold receptors, neurons who encode environmental temperature information in their firing trains, exhibiting therefore a wide of firing patterns. This Huber-Braun (HB) model captures their rich dynamics by making modifications to the HH model, simplifying it in some aspects, and also adding subthreshold oscillation currents and two temperature-dependent factors to the ionic currents, which made it agree very well with the experimental data (Braun et al., 1998, 2011).

The model has a rich variety of different firing regimes that can be accessed by changing a physiological parameter (the temperature). For instance, it has two different transitions from tonic-to-bursting transitions, going from tonic spiking to chaotic bursting and then to regular

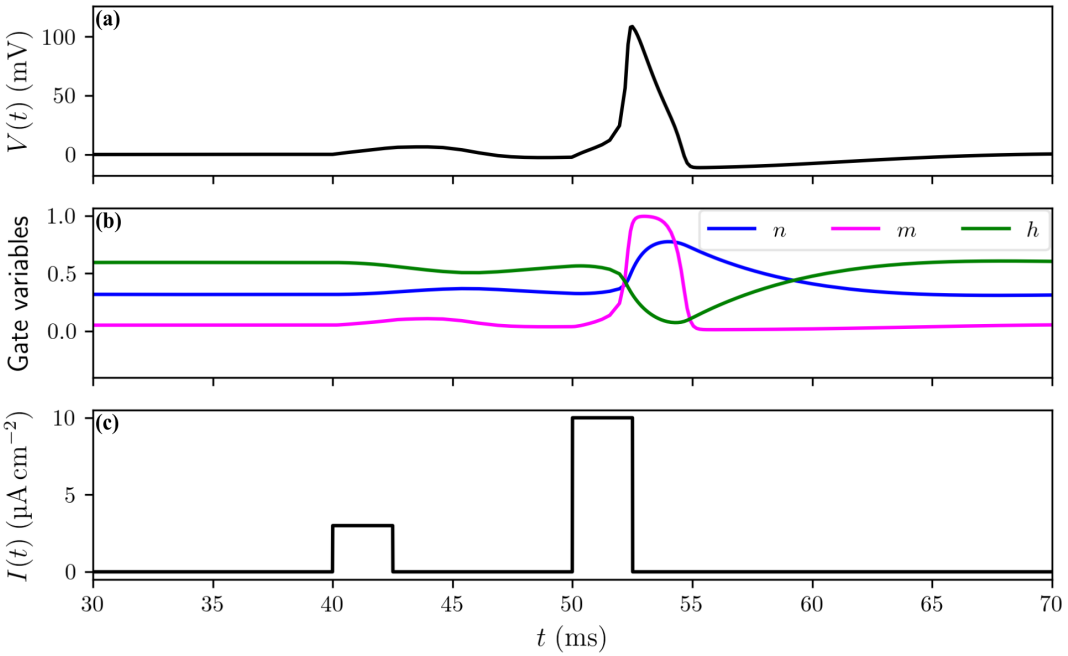

Figure 3.1: **State variables of the Hodgkin-Huxley model as a response to the application of square pulses.** Panel (a) displays the membrane voltage and panel (b) displays the activation and inactivation variables. The injected current is shown in panel (c). We see that the action potential, happening at $t \approx 52.5$ ms, only occurs for sufficiently strong currents.

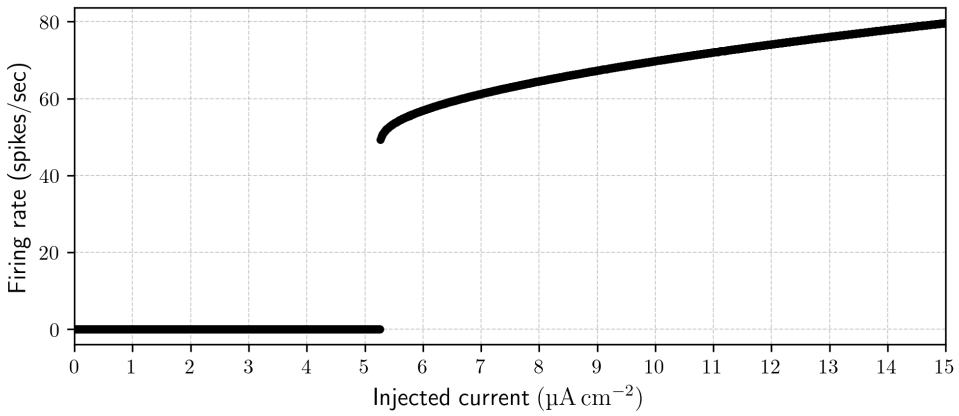

Figure 3.2: **The current-firing rate relation, also called gain function, of the Hodgkin-Huxley neuron.** The discontinuous jump in the firing rate characterizes it as of type II excitability.

bursting with an increase in the temperature. The bursting regime is made possible by the subthreshold currents, the physiological mechanism being similar to the one in neocortical chattering neurons and respiratory neurons, as already mentioned in section Section 1.5.2.

Despite having been first proposed to study cold receptors, who don't form networks (Feudel et al., 2000), the physiological similarities with other neurons that do form justify its use in networks. Furthermore, the model is very convenient for a study of neural networks' dynamics, since it is able to switch between different firing modes with a single change in a parameter. Finally, this model's rich dynamics have proven to be very useful in a variety of studies (Feudel et al., 2000; Finke et al., 2010; Postnova et al., 2007a,b; Du et al., 2010).

3.2.1 Model equations

The main equation for the model is

$$C_{\mathrm{M}}\frac{dV_i(t)}{dt} = -J_{\mathrm{d}} - J_{\mathrm{r}} - J_{\mathrm{sd}} - J_{\mathrm{sr}} - J_{\mathrm{l}} - J_{\mathrm{ext}}, \tag{3.18}$$

where C_{M} is the membrane capacitance; V is the membrane potential; J_{k} (k = {d, r, sd, sr, l}) are ionic currents and J_{ext} is an external current. The capacitance and the ionic currents are taken over a unit area. The leakage current J_{l}, generated by the natural permeability of the neuronal membrane, is

$$J_{\mathrm{l}} = \bar{g}_{\mathrm{l}}(V - E_{\mathrm{l}}). \tag{3.19}$$

The other ionic currents can be divided into two groups: (i) the fast, spike-generating depolarizing J_{d} and repolarizing J_{r} currents and (ii) the slow, oscillation-generating slow depolarizing J_{sd} and slow repolarizing J_{sr} currents (Feudel et al., 2000; Finke et al., 2010). Depolarizing currents tend to increase the membrane potential V, while repolarizing currents tend to decrease it. The fast group corresponds to the ionic currents J_{Na} and J_{K} in the HH model, but the Sodium inactivation gate is disregarded for simplicity. The slow group is an addition to the model, and has significantly slower activations. These currents are activated for potentials V below the firing threshold of the model (reason why they are called subthreshold currents). The interplay between fast and slow variables is essential for bursting behavior (Rinzel, 1987; Postnova et al., 2007a), which is the motivator for introducing the subthreshold currents in this model. Physiologically, J_{d} usually corresponds to a Sodium current, J_{r} to a Potassium current, J_{sd} to a persistent (non-inactivating) Sodium current (and also to a few calcium ions (Feudel et al., 2000)) and J_{sr} to a Calcium-dependent Potassium current. The equations for d, r, sd, sr are

$$J_{\mathrm{k}} = \rho\bar{g}_{\mathrm{k}}a_{\mathrm{k}}(V - E_{\mathrm{k}}),\ \mathrm{k} = \{\mathrm{d}, \mathrm{r}, \mathrm{sd}, \mathrm{sr}\}, \tag{3.20}$$

where ρ is a temperature-dependent factor, $\bar{g}_{\mathrm{k}}$ is the maximal conductance, a_{k} is the activation variable and E_k is the reversal potential of the ionic current k.

The activation variables follow

$$\frac{da_{\mathrm{k}}}{dt} = \frac{\phi}{\tau_{\mathrm{k}}}(a_{\mathrm{k},\infty} - a_{\mathrm{k}}),\ \mathrm{k} = \{\mathrm{d}, \mathrm{r}, \mathrm{sd}\}, \tag{3.21}$$

where ϕ is the second temperature-dependent factor, τ_k is a characteristic time and $a_{k,\infty}$ is the steady-state activation variable, given by

$$a_{\mathrm{k},\infty} = \frac{1}{1 + \exp[-s_{\mathrm{k}}(V - V_{0\mathrm{k}})]},\ \mathrm{k} = \{\mathrm{d}, \mathrm{r}, \mathrm{sd}\}. \tag{3.22}$$

In this case, s are half-activation slopes and $V_{0\mathrm{k}}$ are the half-activation potentials.

The sr current activation variable is

$$\frac{da_{\mathrm{sr}}}{dt} = \frac{\phi}{\tau_{\mathrm{sr}}}(-\eta J_{\mathrm{sd}} - \gamma a_{\mathrm{sr}}), \tag{3.23}$$

where η is a constant for the coupling between J_{sd} and J_{sr} (physiologically mediated by Calcium (Postnova et al., 2007a)) and γ is a tuning factor for the time constant.

Table 3.1: Parameter values of the constants for the Huber-Braun neuron model (Braun et al., 1998).

Membrane capacitance		$C_m = 1.0\,\mu F/cm^2$		
Maximum conductances (mS/cm^2)	$\overline{g}_{Na} = 1.5$	$\overline{g}_K = 2.0$	$\overline{g}_{sd} = 0.25$	$\overline{g}_{sr} = 0.4$
	$\overline{g}_l = 0.1$	$g_c \equiv 1.0$		
Characteristic times (ms):	$\tau_{Na} = 0.05$	$\tau_K = 2.0$	$\tau_{sd} = 10$	$\tau_{sr} = 20$
	$\tau_r = 0.5$	$\tau_d = 8.0$		
Reversal potentials (mV):	$E_{Na} = 50$	$E_K = -90$	$E_{sd} = 50$	$E_{sr} = -90$
	$E_l = -60$	$V_{0Na} = -25$	$V_{0K} = -25$	$V_{0sd} = -40$
	$E_{syn} = 20$			
Other parameters:	$\rho_0 = 1.3$	$\phi_0 = 3.0$		
	$T_0 = 50\,°C$	$\overline{T}_0 = 10\,°C$	$s_{Na} = 0.25\,mV^{-1}$	$\eta = 0.012\,cm^2/\mu A$
	$s_{sd} = 0.09\,mV^{-1}$	$\gamma = 0.17$	$s_K = 0.25\,mV^{-1}$	$s_0 = 1.0\,mV^{-1}$

The scaling factors, introducing the temperature dependence, are

$$\phi = \phi_0^{(T-T_0)/\overline{T}_0} \tag{3.24}$$

$$\rho = \rho_0^{(T-T_0)/\overline{T}_0}. \tag{3.25}$$

Finally, J_{ext} represents either an external current injected to the neuron or a synaptic current. This is the coupling term used in the network. Parameter values are displayed in Table 3.1. These are taken from the original papers (Braun et al., 1998). The reference temperature T_0 was changed originally (Prado et al., 2014) to 50 °C so that the temperature T could lie in the range of mammalian temperatures. This is for convenience only.

3.2.2 Dynamics

Figure 3.3 depicts the state variables of the model for $T = 31\,°C, 37\,°C, 38\,°C, 40\,°C$. For $T = 31\,°C$, the neuron is firing periodically and constantly (tonic spiking). At $T = 37\,°C$, the neuron is bursting chaotically. For $T = 38\,°C$ and $T = 40\,°C$, the neuron is bursting periodically. Therefore, we see that changing the temperature leads to different firing modes.

A careful analysis reveals that a_d and a_r behave very much like what we expect from Na^+ and K^+, respectively: activation of a_d depolarizes the membrane (upstroke), while the later activation of a_r repolarizes the membrane (downstroke). We also see that, during the burst, the sr current builds up until, when it reaches a maximum, the neuron terminates bursting and starts the quiescent phase. During this phase, the sr current deactivates, allowing another burst to start (Finke et al., 2010). Therefore, the bursting mechanism is based on the activation of the outward sr current, which puts the HB neuron close to neocortical chattering neurons. There is also the deactivation of the inward sd current, which puts the HB closer to pre-Botzinger (respiratory rhythm) neurons (Izhikevich, 2007).

A more complete analysis of the bursting mechanism has been done in (Finke et al., 2010), where the authors separated the system into two subsystems, the fast and the slow ones. They showed that the fast subsystem is always at rest, though still excitable, and the slow subsystem is oscillatory. The idea then is that the slow subsystem could then drive the fast subsystem to spiking or to resting behavior. This is roughly the case, but not complete so, due to a nonlinear coupling between the two systems that complicates matters. Still, various characteristics of the system can be explained in this way. Increasing the temperature, the oscillations in the slow subsystem (i) have smaller wavelength and (ii) have higher amplitude. The authors show that the reduction of the wavelength decreases the number of spikes per burst. Also, they showed that the

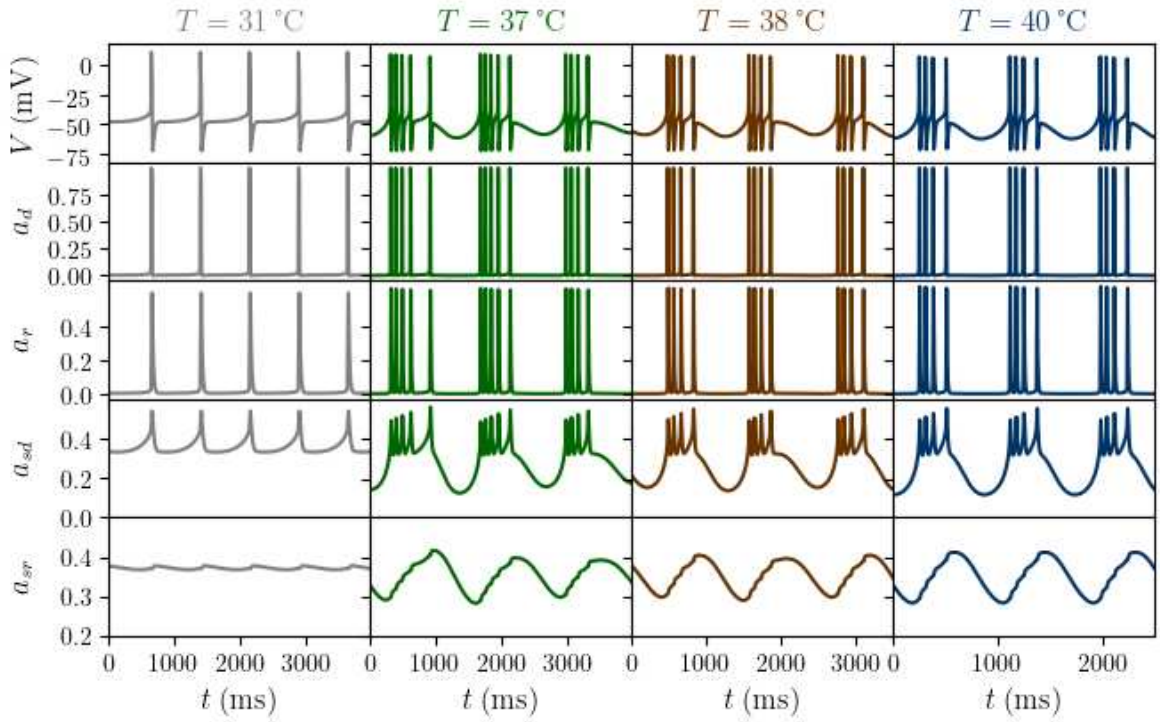

Figure 3.3: **The variables of the Huber-Braun model for different firing modes**, in $T = 31\,^{\circ}\text{C}$ (gray), $T = 37\,^{\circ}\text{C}$ (green), $T = 38\,^{\circ}\text{C}$ (brown) and $T = 40\,^{\circ}\text{C}$ (blue). An increase in the temperature takes the neuron from tonic spiking to chaotic bursting, to periodically firing. A transient time (roughly 45 500 ms) was taken from the simulations.

changes in the amplitude governs the changes in the firing modes (from resting to spiking) and the different spiking patterns during bursting (Finke et al., 2010).

3.2.3 Bifurcations

Given the voltage trace, we can calculate the times between bursts (inter-burst times IBI) or between spikes (inter-spike times ISI), as described in Section 5.3. Then, we can plot these values as a function of the temperature T, obtaining a bifurcation diagram, depicted in Fig 3.4, which shows qualitative changes in the system's behavior (represented by the ISI) as the parameters change. These changes are called bifurcations in dynamical systems theory and are very important in order to understand the behavior of the system. These were studied in the HB model with and without noise in some works (Finke et al., 2010, 2011; Braun et al., 2011; Feudel et al., 2000; Braun et al., 2000).

For temperatures $T \lessapprox 31.09\,^{\circ}\text{C}$, the neuron has a single ISI value, indicating, as we already saw, a periodic spiking. At that temperature, a period doubling cascade begins, leading to chaotic bursting. The bursting behavior is indicated by the clear separation of two ISI groups: one with low values, indicating times between spikes inside a burst and one with higher values, for the times between spikes of adjacent bursts. Further increasing the temperature leads to periodic windows, opened by a saddle-node bifurcation and closed by an interior crisis, very much like the behavior for the logistic map (Feudel et al., 2000). At $T \approx 35.02\,^{\circ}\text{C}$, the ISI values grow very fast (tending to infinity). This occurs due to a homoclinic bifurcation (Feudel et al., 2000).

At $T \approx 37.7\,^{\circ}\text{C}$ we see a transition from chaotic bursting to periodic, via an inverse period doubling cascade.

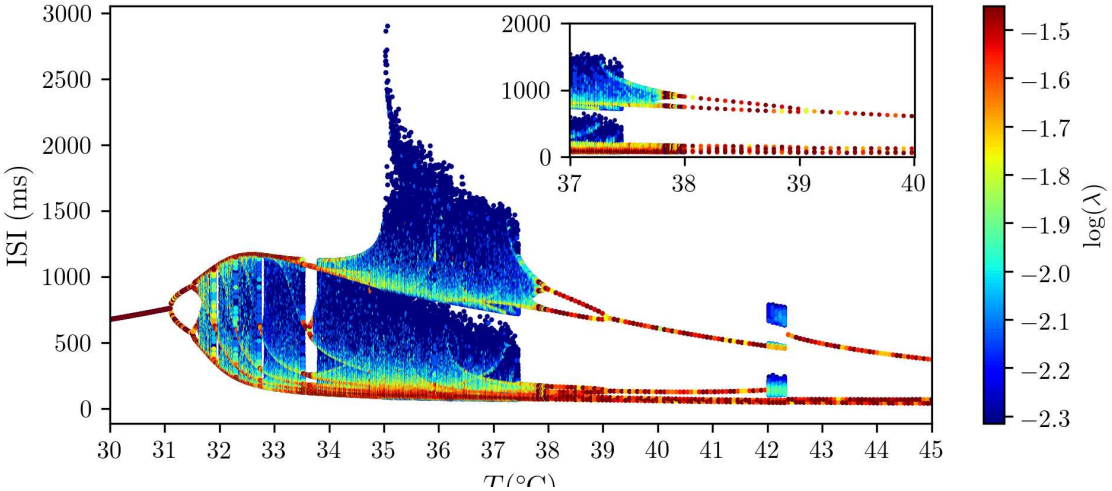

Figure 3.4: **Bifurcation diagram of the ISIs versus temperature for an uncoupled Huber-Braun neuron.** The color scheme corresponds to the logarithm of the frequency λ of appearance of each value of ISI. Parameters are given in Table 3.1.

Instead of using temperature, we may also use the external current J_{ext}. This is displayed in Fig 3.5 for $T = 38\,^{\circ}\text{C}$. We see that the external current destabilizes the periodic orbit and a chaotic behavior emerges. Furthermore, we note that external inputs can significantly increase the range of IBI in the HB neuron. This is also observed in the coupling currents for the coupled networks.

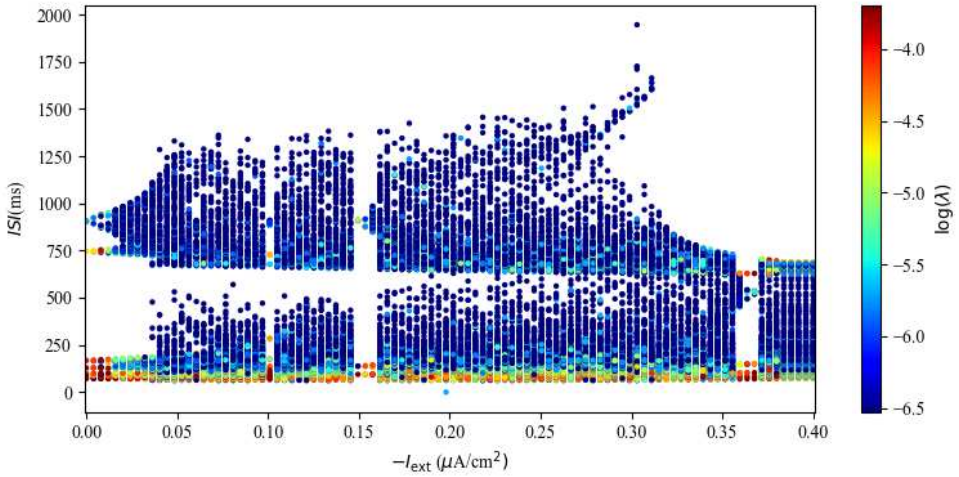

Figure 3.5: **Bifurcation diagram for the external current J_{ext} at $T = 38\,^{\circ}\text{C}$.** The current has negative value, so that its influence on the neuron is excitatory (cf. (3.18)), mirroring the influence of excitatory neurons. A complex bifurcation diagram emerges, with bifurcations happening even for relatively small current amplitudes. The color scheme corresponds to the logarithm of the frequency λ of appearance of each value of ISI. Parameters are given in Table 3.1.

To summarize, and for reference, in Fig 3.6 we show representative membrane potentials for the three temperatures we focus on this dissertation ($T = \{37, 38, 40\}^{\circ}\text{C}$) along with the bifurcation diagram.

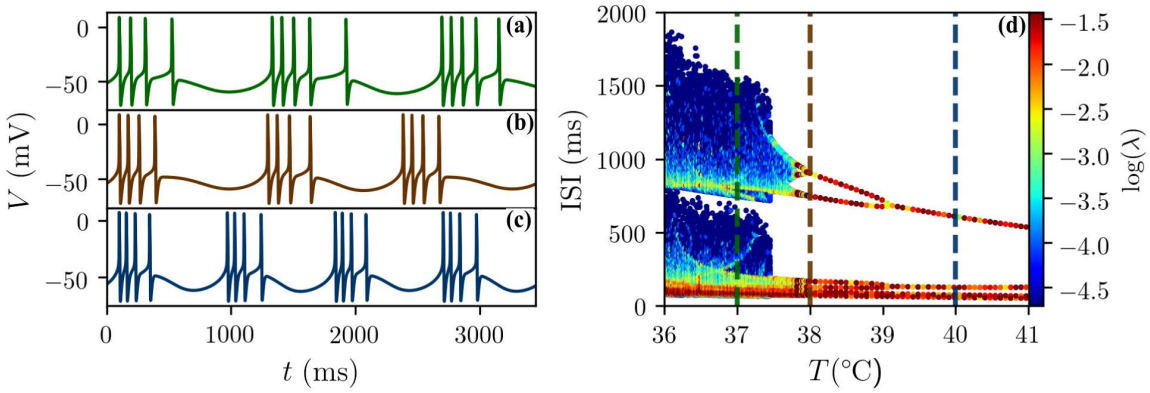

Figure 3.6: **Huber-Braun neurons' dynamics.** In the first row (panels (a), (b), (c)) the representative membrane potentials for the uncoupled neuron are displayed in green, brown and blue for 37 °C, 38 °C, 40 °C, respectively. The chaotic bursting in 37 °C suffers an inverse period doubling bifurcation and at 38 °C it becomes regular bursting with two IBIs, until a final bifurcation leads to regular bursting with one IBI in 40 °C.

We can also verify the periodicity or chaoticity of the uncoupled HB neuron through its Lyapunov Spectrum. This is shown in Fig 3.7 for various temperatures. The figure shows that $T = 37\,°\text{C}$ has positive maximum Lyapunov exponent, indicative of chaotic behavior, and that $T = 38\,°\text{C}$ and $T = 40\,°\text{C}$ have null maximum exponent, showing periodic behavior.

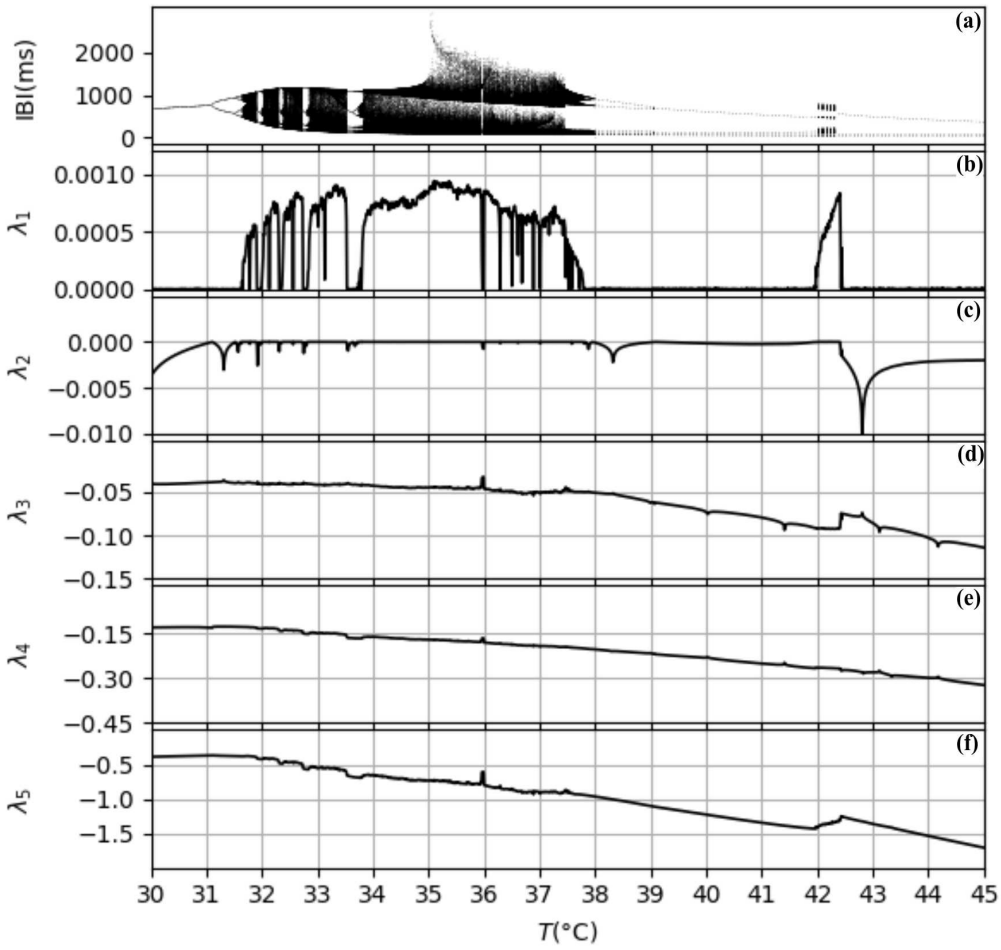

Figure 3.7: **Lyapunov spectrum for the HB neuron.** Panel (a) shows the inter-burst intervals for the Huber-Braun neuron for various temperatures. Panels (b)-(f) then depict the neuron's lyapunov spectrum. We can see that the maximum lyapunov exponent λ_1 goes to 0 at the periodic windows and, specially important, at $T = 38\,°\text{C}$ and $T = 40\,°\text{C}$. For $T = 37\,°\text{C}$ it is positive, indicating chaotic behavior. Calculation is made through the algorithm by Benettin (**?**), but could also be made with the algorithm described in Section 2.3.3.

4 COMPLEX NETWORKS

In this chapter we describe how to model the structure of connections between neurons by making use of graph theory. The structural organization (also called topology, or connection scheme) of the brain is known to be very complicated (Bullmore and Sporns, 2009; Sciences, 2002) and to be very important to support the relevant dynamics (Marconi et al., 2012). Despite all its intricacy, the field of complex networks has revealed, using largely graph theory, important features of the brain topology. Some of these features are small-worldness (roughly, high clustering while maintaining low mean distance between neurons), modularity (brain has a functionally hierarchical structure) and the presence of hubs (neurons with very high connectivity) (Bullmore and Sporns, 2009). The first feature is indeed ubiquitous in a wide range of networks, not just neural ones, and is described in more detail subsequently. Before that, we introduce some fundamental concepts of graph theory.

4.1 ELEMENTS OF GRAPH THEORY

A graph is simply a set of nodes (also called vertices) linked by connections (also called edges). These connections may be directed (one-way) or undirected (two-way), unweighted or weighted. In a neural network, the nodes may be neurons, brain areas, or even electrodes, with the connections being synapses, fibers or some association measure, respectively (Bullmore and Sporns, 2009; Fornito et al., 2013; De Vico Fallani et al., 2014). For networks of chemical synapses, the graph is directed (since neuron A being connected to B doesn't imply in the inverse being true), while for electrical synapses (gap junctions) the graph is undirected. We denote the number of nodes, also called the network size, as N and the number of connections as $\mathscr{N}$.

4.1.1 Adjacency matrix

A useful way to represent a graph is by the adjacency matrix $\mathbf{A}$. For unweighted graphs, this is a binary matrix, with element $A_{ij} = 1$ if j is connected to i (i.e. i receives a connection from j) and $A_{ij} = 0$ otherwise. For weighted graphs, A_{ij} denotes the weight of the connection from j to i. Naturally, for undirected graphs $A_{ij} = w \implies A_{ji} = w$ ($w = 0, 1$ for unweighted graphs), therefore the adjacency matrix is symmetric.

As a note, these matrices tend to be sparse, so a computationally more effective way is to define an adjacency vector. For unweighted graphs, this vector contains the indices of the nonzero connections.

4.1.2 Average path length and Global efficiency

We define the distance d_{ij} between any two nodes i and j as the total number of edges connecting them through the shortest route (Chen et al., 2014). The average path length, or characteristic path length of a graph is then the average of all distances:

$$L = \frac{1}{N(N-1)} \sum_{i \neq j} d_{ij}. \tag{4.1}$$

A short L indicates high global efficiency for sequential transfer of information (Latora and Marchiori, 2001). A way to measure efficiency for parallel transfer of information is given in (Latora and Marchiori, 2001). First, the average efficiency of the graph can be defined as

$$E = \frac{1}{N(N-1)} \sum_{i \neq j} \frac{1}{d_{ij}}. \tag{4.2}$$

Then, "ideal" efficiency E_{id} is defined as E in the case of a fully connected network (it is 1 for unweighted graphs). At last, the global efficiency, measuring how close to the "ideal" case the graph is, is:

$$E_{\text{glob}} = \frac{E}{E_{\text{id}}}. \tag{4.3}$$

Besides the convenient meaning and interpretability of this measure, it is also useful as a replacement of L because it still has meaning for disconnected graphs (graphs with at least one node without connections) (Latora and Marchiori, 2001; Bullmore and Sporns, 2009).

4.1.3 Neighborhood

We define the neighborhood Ω_i of a node i as the set of nodes immediately connected to it. Denoting a possible edge between nodes i and j as e_{ij} and the set of all edges as E, we have the definition:

$$\Omega_i \equiv \left\{ j : e_{ij} \in E \vee e_{ji} \in E \right\}. \tag{4.4}$$

4.1.4 Clustering coefficient

If the neighbors of a node are also directly connected between themselves, we say they form a cluster (in a graph-theoretical sense) (Bullmore and Sporns, 2009). To quantify the degree of clustering in a network, we define the clustering coefficient of a node as the number of connections existing between its neighbors relative to the maximum possible number of connections (Watts and Strogatz, 1998).

For a given node i, with k_i neighbors, the maximum number is $k_i(k_i - 1)$ (for directed). Denoting $\mathscr{N}_i$ as the number of actual connections between the neighbors, then

$$C_i = \frac{|\left\{ e_{jk} : j, k \in \Omega_i, e_{jk} \in E \right\}|}{k_i(k_i - 1)} = \frac{\mathscr{N}_i}{k_i(k_i - 1)}. \tag{4.5}$$

The clustering coefficient for the network is then the average taken over all nodes (Watts and Strogatz, 1998; Chen et al., 2014)

$$C = \frac{1}{N} \sum_{i=1}^{N} C_i. \tag{4.6}$$

A high clustering is associated with a high local efficiency of information transfer (Bullmore and Sporns, 2009). A way to quantify this is also given in (Latora and Marchiori, 2001), where the local efficiency is defined as the average efficiency of all neighborhoods in the graph:

$$E_{\text{loc}} = \frac{1}{N} \sum_{i} E(\Omega_i). \tag{4.7}$$

4.1.5 Degree distribution

The degree k of a node is defined as the total number of connections it makes and receives. For a directed graph, we may also define an out-degree to be the number of edges leaving the node (number of connections it makes with other nodes) and in in-degree to be the number of edges entering the node (number connections it receives from other nodes). The distribution of degrees is defined by a probability distribution and is an important characteristic of a graph (Chen et al., 2014).

4.2 GRAPH TOPOLOGIES

In this section, we describe some common and important topologies.

4.2.1 Regular graphs

A regular graph is one in which all nodes have the same number of connections (same degree). An important regular graph is the ring graph, which contains a periodic boundary condition and in which each node is connected to the $2k$ neighbors that are closest (in the indices). The ring network therefore has high L, but big C: low global efficiency, but high local efficiency. Another important graph is the global one, in which all pairs of neurons are connected, leads to the minimum possible L and maximum C (maximum local and global efficiencies).

4.2.2 Random graphs

On the other extreme of regular networks are the random ones, in which, generally, the number N of nodes and $\mathscr{N}$ of connections is fixed, but the topology itself is chosen at random. An important algorithm for random graphs was proposed by Erdős and Renyi (Erdos and Rényi, 2011):

1. Generate N nodes
2. For each of all possible pairs (i, j) $j \neq i$ of nodes, connect j to i with probability p.

Thus, the expected number of connections is $pN(N-1)$ (Chen et al., 2014). This results in a directed graph with no self-loops. These networks start completely disconnected por $p = 0$ and become denser as it is increased until they form a global network at $p = 1$. For most networks generated in this manner, the minimum probability p required for them to be connected (no isolated nodes) is $p \sim \ln N/N$. The average degree is $\langle k \rangle = p(N-1) \approx pN$. Consequently, it can be shown that average path length of these networks is

$$L_{\mathrm{ER}} \sim \frac{\ln N}{\ln \langle k \rangle}, \tag{4.8}$$

and the clustering coefficient is

$$C_{\mathrm{ER}} \sim \frac{\langle k \rangle}{N} = p. \tag{4.9}$$

This is the opposite case from regular networks: both L and C are small: Erdős-Renyi (ER) graphs have high global efficiency, but low local efficiency. As a note, we remark that the degree distribution of these networks is Poissonian.

4.2.3 Small-world graphs

Ring networks, with their local structure, have high average path length and clustering, while random ones, without local structures, are the opposite. It turns out that intermediate networks, with some local structure and some long-range connections, are ubiquitous in various areas, like in neural networks, power grids, social networks (Watts and Strogatz, 1998) and even protein structure (Barabasi and Albert, 1999). These graphs, called small-world (SW) graphs, are characterized by their low average path length (close to random), but high clustering coefficient (much bigger than random). In other words, they are efficient both locally and globally (Latora and Marchiori, 2001).

There are two important algorithms for generating SW graphs. The first is the original, due to Watts and Strogatz (Watts and Strogatz, 1998), and the second is due to Watts and Newman (Newman and Watts, 1999).

4.2.4 Watts-Strogatz algorithms

To generate a WS graph, the procedure is

1. Start with a ring network with N nodes and each neuron having $2K$ neighbors.
2. For pair (i, j) of connected nodes in the ring, rewire the edge with probability p. This rewiring is as follows: keep i, but change j to another random node in the network.

This generates a directed graph with no self-loops and $2KN$ connections. The graphs start being ring-shaped at $p = 0$, but receive long-range connections as p is increased until, at $p = 1$, a random graph is obtained. The probability p serves therefore as a transition parameter.

This algorithm has the advantage of a fixed number of connections and being able to transition from regular to small-world to random, but has the disadvantage of possibly generating disconnected networks (with isolated neurons).

Figure 4.1 depicts the average path length and clustering coefficient for graphs generated by the Watts-Strogatz route with $N = 1000$ and $K = 10$ averaged over 20 initializations. The small-world phenomenon occurs roughly in the range $[10^{-3}, 2 \times 10^{-2}]$, where C is still big, close to the regular network, but L has dropped significantly, tending to the random network. This is depicted in Fig 4.2(a).

4.2.5 Newman-Watts algorithm

To solve the disconnection problem with the WS model, Newman and Watts (Newman and Watts, 1999) proposed to add connections, instead of changing them. They followed the procedure:

1. Start with a ring network with N nodes and each neuron having $2K$ neighbors.
2. For every pair of originally unconnected nodes and add a connection with a probability p.

Again, this graph has no self-loops. It starts with a regular graph at $p = 0$ and ends with a global (fully-connected) one at $p = 1$. The probability serves then as a transition parameter from a sparse regular network to a dense one. This is depicted in Fig 4.2(b).

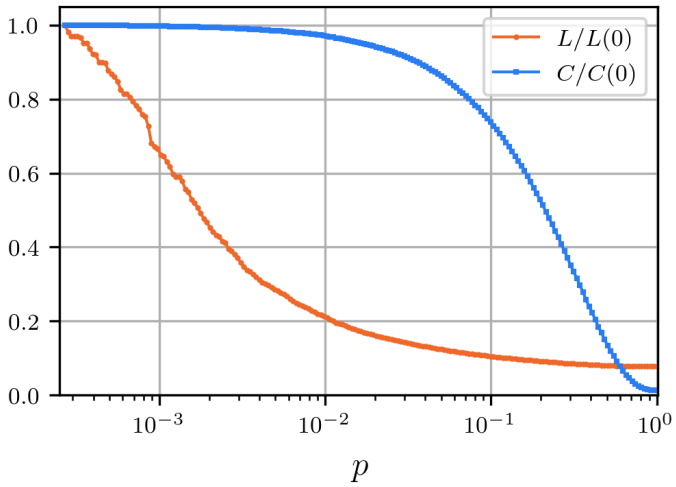

Figure 4.1: **Average path length $L(p)$ and clustering coefficient $C(p)$ for networks following the Watts-Strogatz route.** The parameters are $N = 1000$ and $k = 10$, with the results averaged over 20 random realizations of the network.

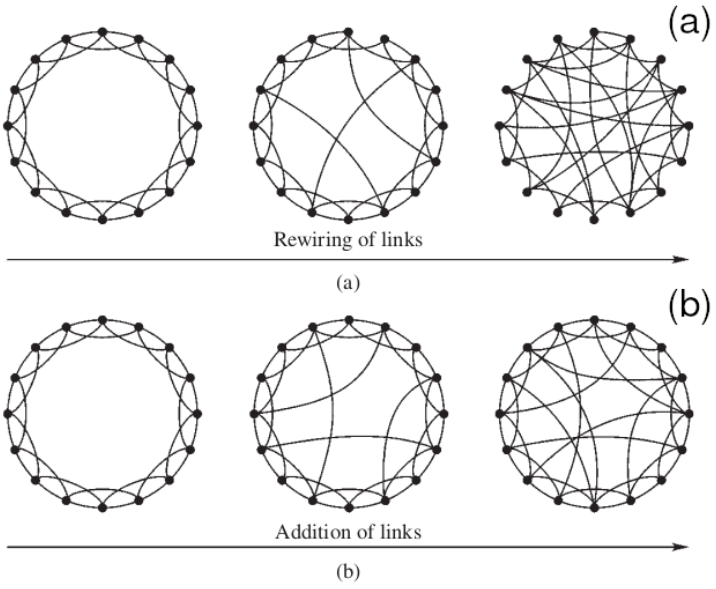

Figure 4.2: **The small-world networks generated through the Watts-Strogatz algorithm (panel (a)) and the Newman-Watts one (panel (b)).** Figure is taken from (Chen et al., 2014).

5 METHODS AND ANALYSIS

5.1 NETWORK IN THIS DISSERTATION

In chapters 3 and 4 we studied how to model neurons and their connections. We are now ready to unite these concepts and detail the construction of the neural network used in this dissertation.

The neurons are all identical, point-like, with dynamics described by the Huber-Braun model in Section 3.2. A neuron i is influenced by the others through the external current $J_{\mathrm{i,ext}}$ it receives, henceforth called coupling current $J_{\mathrm{i,coup}}$. For this synaptic current, we follow (Dayan and Abbott, 2005; Destexhe et al., 1994) and describe it using the Hodgkin-Huxley formalism:

$$J_{i,\mathrm{coup}} = \bar{g} P (V_i - E_{\mathrm{syn}}), \tag{5.1}$$

where $\bar{g}$ is the maximum conductance of the postsynaptic membrane; P is the fraction of bound postsynaptic receptors; E_{syn} is the synaptic reversal potential. For convenience, we write the maximum conductance as

$$\bar{g} = g_c \epsilon, \tag{5.2}$$

where $g_c \equiv 1\,\mathrm{mS/cm^2}$, introduced to carry the units, ϵ is the control parameter used for the synaptic conductance, henceforth called the coupling strength. The fraction P is considered a summation over the fraction of bound receptors due to each connected neuron:

$$P = \sum_{j \in \Gamma_i} r_j(t), \tag{5.3}$$

where Γ_i is the neighborhood of the i-th neuron and r_j is the coupling variable due to a neighbor j, whose temporal dynamics is (Destexhe et al., 1994)

$$\frac{dr_j}{dt} = \left(\frac{1}{\tau_r} - \frac{1}{\tau_d}\right) \frac{1 - r_j}{1 + \exp[-s_0(V_j - V_0)]} - \frac{r_j}{\tau_d}. \tag{5.4}$$

In this equation, τ_r and τ_d are characteristic times controlling the rise and decay times, and $s_0 \equiv 1\,\mathrm{mV^{-1}}$.

Putting all the equations together, the synaptic current arriving at neuron i is:

$$J_{i,\mathrm{coup}} = g_c \frac{\epsilon}{\nu} (V_i - E_{\mathrm{syn}}) \sum_{j \in \Gamma_i} r_j(t). \tag{5.5}$$

Coupling current:	$g_c \equiv 1.0\,\mathrm{mS/cm^2}$	$E_{\mathrm{syn}} = 20\,\mathrm{mV}$	$\tau_{\mathrm{r}} = 0.5\,\mathrm{ms}$	$\tau_{\mathrm{d}} = 8.0\,\mathrm{ms}$
Network parameters:	$N = 1000$	$\mathscr{N} = 4000$	$K = 4$	

Table 5.1: Parameter values related to the coupling and network.

In Table 5.1 we show the previously defined constants. The synaptic reversal potential was chosen at $E_{\mathrm{syn}} = 20\,\mathrm{mV}$ to ensure that all synapses are excitatory.

We used a ring-shaped random network topology, generated with the Watts-Strogatz algorithm for $p = 1$, directed and with no self-loops. The size N, number of neighbors K and

number of connections $\mathcal{N}$ are displayed in Table 5.1. The average path length and clustering coefficients for the random network were $L = 4.857$ and $C = 0.0045$. This is similar to the values obtained for $K = 10$, shown in Fig 4.1.

The degree distribution, along with a representation of the network, is displayed in Fig 5.1.

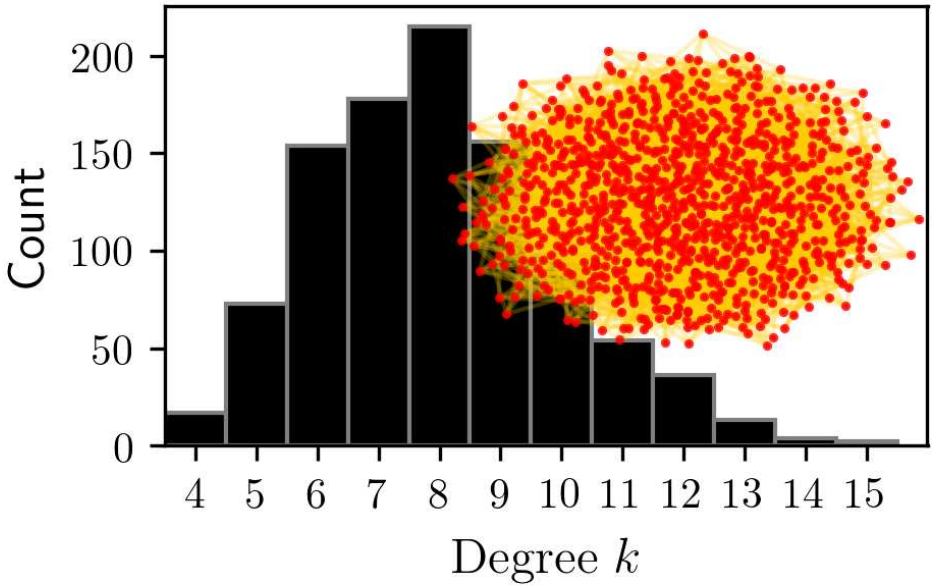

Figure 5.1: **Degree distribution for the network topology used.** Histogram of the degree distribution for the Watts-Strogatz network with $p = 1.0$, $k = 4$, $N = 1000$, along with a representation of the nodes (red circles) and their connections (yellow lines).

5.2 SOFTWARES

5.2.1 Numerical Integration

The solution of the various differential equations we mentioned previously is generally obtained using numerical integration. For all the simulations, unless otherwise stated, the CVODE solver (Hindmarsh et al., 2005) was used. It implements a 12-th order Adams-Moulton predictor-corrector method (Butcher, 2016). The time-step is adaptative, with a maximum of $h = 0.1$ ms. Absolute and relative tolerances were set at 10^{-6}. Tests were made with tolerances up to 10^{12} and $h = 0.01$ ms, and results were very similar.

5.2.2 Analysis and plotting

The data analysis was done both in Python (Van Rossum and Drake Jr, 1995), with help of the NumPy module (Oliphant, 2006) and in Julia (Bezanson et al., 2017). Plotting was done with Python using MatPlotLib (Hunter, 2007).

5.3 CALCULATING SPIKING AND BURSTING TIMES

Spike times are registered when the membrane potential V crosses the threshold $V_{\text{th}} = -10\,\text{mV}$ with positive first derivative. In dynamical systems theory this is known as a Poincaré surface of section (Feudel et al., 2000).

Bursts are then seen as sequences of any number (bigger than 1) of rapid spikes, followed a long quiescent period. With this, an algorithm can also determine the bursting times, defined as the time of the first spike in each burst.

Figure 5.2 shows a typical time series for the membrane potential of the Huber-Braun neuron for $T = 38\,^{\circ}\text{C}$, with the spike and burst times shown in orange and blue circles, respectively.

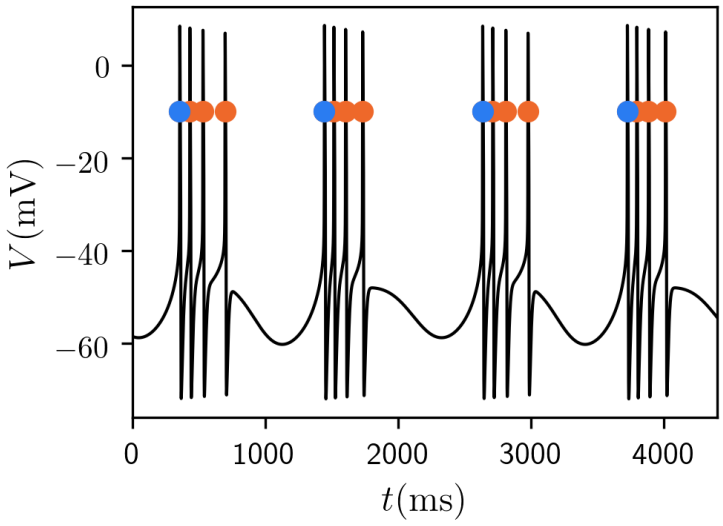

Figure 5.2: **Membrane potential V (black line), spike and burst times (orange and blue circles, respectively) for an isolated HB neuron with** $T = 38\,^{\circ}\text{C}$. A transient of $t = 100\,300$ ms was disconsidered.

We remark that this definition works for all parameter values studied in this work. For coupling strengths higher than the ones used, single spikes start appearing isolated from the bursts, and then it becomes ambiguous whether it is a mixed-mode oscillation or they are part of the burst. In the cases we studied, however, this is not significant because these events are rare and the distances are small, so the isolated spikes, if they occur, are considered to belong to the previous burst.

5.4 INTER-SPIKE AND INTER-BURST INTERVALS (ISI AND IBI)

An Inter-spike intervals ISI is the difference between subsequent spike times. Therefore, the kth ISI of the ith neuron in a network is difference between its kth and $(k+1)$th spike times:

$$\text{ISI}_{i,k} = t_{i,k+1} - t_{i,k}. \tag{5.6}$$

Similarly for Inter-burst intervals IBI:

$$\text{IBI}_{i,k} = t_{i,k+1} - t_{i,k}. \tag{5.7}$$

5.5 VARIABILITY

We regard neuronal variability as the range of possible responses (in the ISI or IBI) a neuron displays. The variability of one neuron i can be measured using the coefficient of variability CV_i, defined as the normalized standard deviation (Softky and Koch, 1993; Stevens and Zador, 1998):

$$\mathrm{CV}_i = \frac{\sigma\left(\mathrm{IBI}_{i,k}\right)_k}{\langle \mathrm{IBI}_{i,k} \rangle}, \tag{5.8}$$

where $\mathrm{IBI}_{i,k}$ is the sequence of IBIs of neuron i, $\sigma\left(\mathrm{IBI}_{i,k}\right)_k$ is the standard deviation of these IBIs over time (indexed by k) and $\langle \mathrm{IBI}_{i,k} \rangle$ is the average of the IBIs over time.

For a network, we define two types of variability: (i) temporal variability CV_t, the average, taken over all neurons, of each individual neuron's variability; (ii) CV_s ensemble variability is the average, taken over time, of the variability between the neurons. Ensemble variability gives a notion of how IBI are dispersed in the network. The formula for these variabilities is similar to (5.8):

$$\mathrm{CV}_t = \overline{\mathrm{CV}_i}, \tag{5.9}$$

$$\mathrm{CV}_e = \frac{1}{k_{\max}} \sum_{k=1}^{k_{\max}} \frac{\sigma\left(\mathrm{IBI}_{i,k}\right)_i}{\overline{\mathrm{IBI}_{i,k}}}, \tag{5.10}$$

where we use $\overline{(\cdot)}$ to denote an average over neurons (the ensemble), $\sigma(\cdot)_i$ to denote (again) standard deviation over neural indexes i, $k_{\max}$ to denote the total number of IBIs analyzed.

Thus, the temporal variability is the network average of the normalized dispersions in the IBIs of each individual neuron across time, and the ensemble variability measures the time average of the normalized dispersions in the IBIs across the network. The two are in principle different, each giving important information about the network.

5.6 PHASE SYNCHRONIZATION

To quantify phase synchronization (PS) we must first define a phase θ. Since we are generally interested in studying burst PS, we describe the method using burst times, but the same can be done for spike times. The phase is defined such that it starts at $\theta = 0$ and increases by 2θ for each new burst. In between bursts, it is a linear interpolation of the two extremes (Ivanchenko et al., 2004). Mathematically,

$$\theta_i(t) = 2\pi k_i + 2\pi \frac{t - t_{k,i}}{t_{k+1,i} - t_{k,i}}, \ (t_k < t < t_{k+1}), \tag{5.11}$$

where $t_{k,i}$ is the time at which the k-th burst of the i-th neuron ocurred, called the burst time, whose calculation is described in Section 5.3.

Then, the degree of PS is measured via the Kuramoto order parameter (Kuramoto, 1984)

$$R(t) = \frac{1}{N} \left| \sum_{i=1}^{N} e^{j\theta_i(t)} \right|, \tag{5.12}$$

where $j = \sqrt{-1}$ is the imaginary unit here. If $R = 1$, all neurons have the same phase, so the network is completely phase synchronized. If $R = 0$, a lot of different scenarios are possible, in which the network has groups of neurons that are completely out-of-phase. These groups may be

just one neuron (i.e. for each neuron there is another one that is completely out-of-phase), in which case we say the network is completely dessynchronized; they may also even be half of the network, in which case we say the network has anti-phase synchronization. The distinction between these cases can be done using other methods (e.g. raster plots).

We may take the time average of $R(t)$ to obtain the mean Kuramoto order parameter,

$$\langle R \rangle = \frac{1}{n} \sum_{t=t_0}^{t_f} R(t), \tag{5.13}$$

where t_0 is the transient time, t_f is the total simulation time and $n = (t_f - t_0)/h$ is the number of steps, with h being the time step.

We can also calculate the degree of synchronization between two oscillators as the Kuramoto order parameter between only the two of them:

$$R_{ik}(t) = \frac{1}{2} \left| e^{j\phi_i(t)} + e^{j\phi_k(t)} \right|, \tag{5.14}$$

where $j = \sqrt{-1}$ is the imaginary unit here.

5.7 AVERAGE TEMPORAL DRIFT

In this section we define a quantity to measure if neurons are phase-locked. Specifically, we assess the if the differences between firing times (either spike or burst) of different neurons stay constant in time. In the literature, there is a quantifier called the phase-locking value (PLV) (Lachaux et al., 1999), based on the Kuramoto parameter, which could do this. However, in this section we define a simpler quantifier that works well for our networks. In our network, neurons are tonically bursting and with similar periods. Due to this, we can align the burst times of all neurons in the network in bursting events, indexed here by k. For each pair (i, j), we then calculate the distance between their burst times for each event k:

$$\delta_{ij}^k = |t_{i,k} - t_{j,k}|. \tag{5.15}$$

Then, we see if this distance changes in the next bursting event, calculating the absolute difference of this distance between successive events for each pair (i, j),

$$\Delta_{ij}^l = |\delta_{ij}^k - \delta_{ij}^{k-1}|. \tag{5.16}$$

If Δ_{ij}^l is zero, then neurons stayed phase locked (guaranteed by the way we calculate phases 5.6), otherwise they did not. The temporal average of Δ_{ij}, $\langle \Delta_{ij} \rangle$, measures the tendency of the pair (i, j) to drift away from each other across time. We average the result over all pairs of neurons, resulting in

$$\Delta = \frac{1}{N(N-1)} \sum_{i,j,i \neq j}^{N} \langle \Delta_{ij} \rangle \equiv \overline{\langle \Delta_{ij} \rangle}, \tag{5.17}$$

which is termed the average drift of the network. This average drift tendency Δ measures how much, on average, the temporal distances between neurons' firings change. If it is low, neurons are locked together, the difference between their burst start times remaining fixed. If it is high, neurons are not phase-locked. The drift Δ therefore serves as a measure of promiscuity, a

phenomenon discussed in the results section characterized by intermittent changes in the phase differences between neurons.

5.8 CLUSTERING ANALYSIS

Groups of neurons that are functionally related (clusters) are ubiquitous in the brain, and the emergence of transient clusters is thought to form the basis for complex cognition (Bassett et al., 2015) and more (Shine et al., 2016) (for more details, see Section 1.9). In the metastable brain, these groups are constantly being formed and disbanded (Cavanna et al., 2018), which leads us to the idea of measuring promiscuity by the rate of change in cluster formation. To do that, we must first define algorithms for cluster identification. This is a very complex task, with no definite solution. There are various proposal in the literature (Tononi et al., 1998b; Zemanová et al., 2006), varying in levels of complexity. For this dissertation, we want to study rate of change of cluster compositions, and not focus on the clusters themselves, so we used a simple algorithm. In accord with other methods we use, we consider the functional relations as either degree of phase synchronization or of phase difference. These two considerations lead to two similar algorithms: one proposed by Bhowmik (Bhowmik and Shanahan, 2013) and a modification of Bhowmik's.

5.8.1 First cluster algorithm

This algorithm, proposed in (Bhowmik and Shanahan, 2013), uses the degree of PS as a criterion for clustering, using a synchronization threshold R_{th}. The algorithm can be applied for each time t and is as follows:

Algorithm 1: First clustering algorithm.

Result: Clusters.
Calculate the pairwise Kuramoto order parameter R_{ij} (5.14) between all neurons in the network ;
Select the pair with the maximum degree R_{ij};
if $R_{\text{max}} \geq R_{\text{th}}$ **then**
  put the two neurons in the cluster.;
else
  return null ;
end
while size(cluster) < size(network) **do**
  For each neuron i outside the cluster, calculate the Kuramoto order parameter R_i (5.12) as if the neuron were in the cluster. Select the maximum R_i to obtain R_{max}.;
  if $R_{\text{max}} \geq R_{\text{th}}$ **then**
    add the neuron to the cluster;
  else
    return cluster;
  end
end
return cluster;

The cluster returned by this algorithm is guaranteed to have $R \geq R_{\text{th}}$. Depending on the threshold, the cluster can therefore be considered a group of phase-synchronized neurons.

5.8.2 Second cluster algorithm

This second algorithm is very similar, but the clustering criterion is the phase difference between neurons, instead of the Kuramoto order parameter. To use it, we must first define a transformation in the phases.

5.8.2.1 Phase transformation

Suppose a neuron has phase $\phi_1 = 0$ and another has phase $\phi_2 = 2\pi$. Their phase difference is nonzero, even though they are in phase. To resolve this issue, we transform the phases according to

$$\Phi(\phi) = \frac{|\mathrm{mod}(\phi, 2\pi) - \pi|}{\pi}. \tag{5.18}$$

With these transformations, the phases in the previous examples would be $\Phi_1 = \Phi_2 = 0$, so their difference would correctly indicate that they are synchronized.

5.8.2.2 Algorithm

For this algorithm we define a phase difference threshold $\Delta\Phi_{th}$. Then, for each time t:

Algorithm 2: Second clustering algorithm.

```
Result: Clusters
Calculate the histogram of the transformed phases with a number n_bin of bins ;
Identify the mode of the binned phases and select the neuron whose phase is closest
  to the mode. ;
Put it in the cluster
while size(cluster) < size(network) do
    Calculate the average phase of the cluster: Φ_c;
    For each neuron i, calculate the difference between the average cluster phase Φ_c
      and its phase Φ_i ;
    Select the neuron with the smallest phase difference, denoted as ΔΦ_min
    if ΔΦ_min ≤ ΔΦ_th then
        add the neuron to the cluster;
    else
        return cluster;
    end
end
return cluster;
```

This algorithm is returns a cluster that groups neurons with similar phases together. Figure 5.3 shows examples of clusters generated by the second algorithm. The algorithm is very successful, and less ambiguous than others we tested, so it was chosen for the analysis.

5.8.3 Additional parameters and details

For both algorithms, we can apply them to all neurons outside the first cluster, potentially obtaining a second. This can be repeated a number $\mathcal{N}$ of trials, or until all neurons are in clusters. With this, we end up with a sequence of clusters $C_{t,i}$ for each time t.

Furthermore, the algorithms can be applied for any time t, but this is unnecessary. In this dissertation, we only apply the algorithm once every $\Delta t_{\mathrm{cluster}}$. Therefore, clusters are calculated

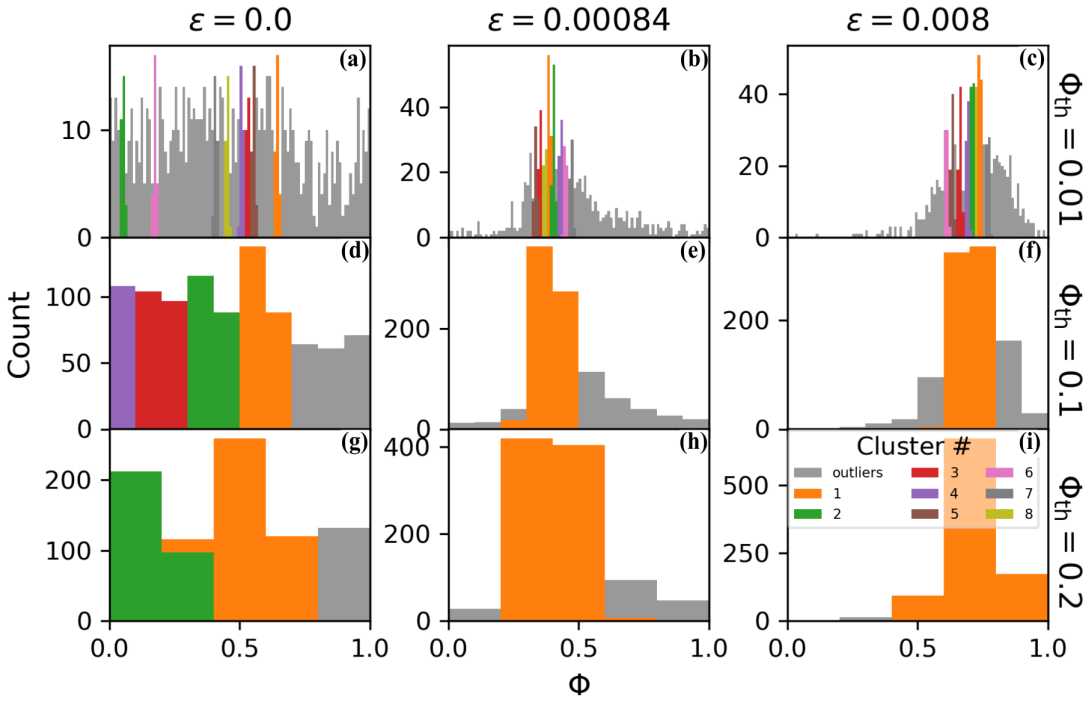

Figure 5.3: **Example of clustering result**. Histogram of the transformed phases Φ for all clusters for coupling strengths $\epsilon = \{0, 0.00084, 0.008\}$ (for relevance, see results Part II) along the columns and cluster thresholds $\Phi_{\text{th}} = \{0.01, 0.1, 0.2\}$ along the rows. Histogram for each cluster has a color, specified in the legend, and neurons outside any cluster, called outliers, are painted in gray. The size of each bin is equal to threshold Φ_{th} used in each case.

times at $\{t_k\}$; $k = 1, 2, \ldots, K$, with K here denoting the maximum number of applications, $t_{k+1} - t_k = \Delta t_{\text{cluster}}\ \forall k$, and with t_1 being the first burst time after the transients.

Through the dissertation, we use $\mathcal{N} = 8$ and $\Delta t_{\text{cluster}} = 1000$ ms. It is very easy to verify the robustness of the results to the former since it is enough to increase it and verify that no more clusters are found (in fact, even 8 clusters is already very rare identify.). The latter parameter was chosen that way because that is around one inter-burst interval. Robustness was tested by decreasing the parameter until $\Delta t_{\text{cluster}} = 100$, and results were very similar.

5.8.4 Cluster set notation

Clusters are sets containing their neurons' indices. A cluster C_i is said to be of size $|C_i|$, meaning the number of neurons inside it. Furthermore, the intersection between two clusters C_i and C_j is denoted $C_i \cap C_j$ and contains all neurons inside C_i and C_j simultaneously.

5.8.5 Time evolution of clusters

An important remark is that the previous algorithms do not establish an a priori relationship between clusters identified at different times. That is, clusters calculated at some time t_k (the k-th application of the algorithm) can be completely independent of clusters at t_{k+1}. This is not the case, as we see in the results Section 8.2.

5.8.5.1 Biggest cluster intersections

One way to verify the previous statement is to focus only on the biggest cluster (BC): at each time t_k, only the cluster with biggest size is selected for analysis. Then, we study how the composition of the BC changes with time by looking at which neurons stay in the BC across time. To do this, we calculate cluster intersections. Starting at a time t_k, we define the cluster intersections $C_{i,\mathcal{T}}(t_k)$ as $\mathcal{T}$ intersections of subsequent clusters, starting at $C_{\mathcal{B}C}(t_k)$:

$$C_{BC,\mathcal{T}}(t_k) \equiv C_{BC}(t_k) \cap C_{BC}(t_{k+1}) \cap \cdots \cap C_{BC}(t_{k+\mathcal{T}}). \tag{5.19}$$

If the cluster composition does not change with time, then $C_{i,\mathcal{T}}(t_k) = C_i(t_k)$ for any $\mathcal{T}$. If, however, it changes, then the size $|C_{BC,\mathcal{T}}(t_k)|$ decays with $\mathcal{T}$ and the decay rate gives a quantitative measure of rate of change of the cluster composition. In the results Section 7.2.2 we show these results, which indicate clusters at different times are related.

5.8.5.2 Analytical consideration

Now we describe a simple analytical result which useful for later. Suppose that, from one time t_k to the next t_{k+1}, the probability of neurons staying in a cluster C_i (for example, the BC) is the same p_i. Then,

$$|C_i(t_k) \cap C_i(t_{k+1})| \equiv |C_{i,1}(t_k)| = p_i|C_i(t_k)|, \tag{5.20}$$

and, therefore, for $\mathcal{T}$ intersections we have

$$\frac{|C_{i,\mathcal{T}}(t_k)|}{|C_i(t_k)|} = p_i^{\mathcal{T}}. \tag{5.21}$$

5.8.6 Measure of Promiscuity

Now we describe how to measure promiscuity indirectly as the rate of change in cluster compositions. The idea is to first measure the proportion of neurons that stay in the cluster as time passes, which we see can be interpreted as the probability of neurons staying in the cluster. The inverse of this probability then leads to the probability of neurons leaving the cluster, which is our measure of promiscuity. We start, for simplicity, analyzing only the biggest cluster, and then show the generalization and analysis considering all clusters.

5.8.6.1 Biggest cluster

To start, we define the proportion (probability) of neurons staying in the biggest cluster as

$$p_{BC}(t_k) \equiv \frac{|C_{BC}(t_k) \cap C_{BC}(t_{k+1})|}{|C_{BC}t_k)|}. \tag{5.22}$$

This can be done for all times $\{t_k\}; k = 1, 2, ..., K-1$ and then averaged to give $\overline{p}_{BC}$. Our measure of promiscuity is then

$$\mathcal{P}_{BC} = 1 - \overline{p_{BC}}. \tag{5.23}$$

In the results Section 7.2.2, we see that the biggest cluster intersections $C_{BC,\mathcal{T}}$ decay exponentially. This fits with the description given in Section 5.8.5.2 (for cluster $i = BC$), with the cluster size decaying according to (5.21). Given this exponential decay, another way to measure p is to use a log $\times$linear plot (like in panel (b) of Fig 7.3), in which then $C_{BC,\mathcal{T}}$ forms a line $y = ax$

where $y = \log \frac{|C_{BC,\mathcal{T}}(t_k)|}{|C_{BC}(t_k)|}$, $x = \mathcal{T}$ and $a = \log(p)$. A linear regression on this plot then gives us p. Though in the results we followed (5.22), we also tried this method, and results were very similar.

5.8.6.2 All clusters

In several cases, the network can have more than one cluster. The BC analysis gives good results and is a good first approach, but a more complete description has to consider all the clusters. In this case, we to calculate the proportion (probability) of neurons staying in each cluster, and average over the clusters. One possible problem arises when doing so if the clusters in the network have similar sizes. This can occur in desynchronized networks or for very small cluster thresholds (eg $\Phi_{\text{th}} = 0.01$). To describe this problem, consider an example: imagine a network of $N = 10$ neurons, in which we apply the algorithm two times (times t_1 and t_2). It is possible that for t_1, clusters are $C_1(t_1) = \{1, 2, 3, 4, 5\}$ and $C_2(t_1) = \{6, 7, 8\}$ (and $\{9, 10\}$ are not in any clusters). Then, for t_2, let us imagine that neurons 9 and 10 get in-phase with 6, 7, 8, and 4 and 5 get out of clusters, so that the clusters then become $C_1(t_2) = \{6, 7, 8, 9, 10\}$ and $C_2(t_2) = \{1, 2, 3\}$. If one were to naively analyze how cluster compositions change according to the cluster indexes (which, in our case, are obtained by sorting according to the cluster size), one would get intersections of null size for both C_1 and C_2, indicating that both clusters disbanded completely. However, that is not the case: as we have seen, only neurons $\{4, 5\}$ changed their behavior. To deal with this problem, we consider the maximum intersections to calculate the probability p. That is, instead of applying the equivalent of (5.22), calculating intersections of clusters with the same index, we do:

$$p_i(t_k) = \frac{\max\left(\left|C_{i,t_k} \cap C_{j,t_{k+1}}\right|\right)}{|C_{i,t_k}|}. \tag{5.24}$$

In the previous example, we would calculate the intersections $C_1(t_1) \cap C_2(t_2)$ and $C_2(t_1) \cap C_1(t_2)$.

By averaging this over time and then over clusters, we have an average probability of neurons staying in clusters p. We then define the measure

$$\mathcal{P} \equiv 1 - p \tag{5.25}$$

to quantify how much, on average, the clusters' compositions change in time, thus serving as a measure of promiscuity.

An alternative way to define p in this case is to calculate the proportion of neurons staying in clusters globally. That is, we calculate the number of neurons staying in their respective clusters (also applying the rule of maximum intersection) and then divide this number by the total number of neurons in clusters, obtaining the second measure p_2:

$$p_2(t_k) = \frac{\sum_{i=1}^{\mathcal{N}} \max\left(\left|C_{i,t_k} \cap C_{j,t_{k+1}}\right|\right)}{\sum_{i=1}^{\mathcal{N}} |C_i|}. \tag{5.26}$$

Both methods give very similar results, and we choose to use p to have a more individual look at each cluster.

6 METASTABILITY IN NEUROSCIENCE

The brain follows two opposing tendencies: specialization of regions and their integration. It has specialized processing regions, operating in parallel and segregated from each other in their activities, and it needs to integrate and globally coordinate some of these regions (Tognoli and Kelso, 2014; Sporns, 2013). Activity in the cortex thus changes continuously, with cortical regions integrating (functionally coupling) and segregating (functionally decoupling) across multiple scales (Stratton and Wiles, 2015). This is important for a variety of behaviors, such as cognition: "the emergence of a unified cognitive moment relies on the coordination of scattered mosaics of functionally specialized brain regions" (Varela et al., 2001). A dynamical regime capable of accounting for these phenomena is metastability (Tognoli and Kelso, 2014).

In this chapter, we provide a mini-review about the different definitions of metastability in neuroscience, and discuss them. Metastability is often used loosely in the field, so we believe this is an important step towards trying to unify the definitions.

We then proceed to briefly categorize different dynamical mechanisms that can lead to metastability. Most of these mechanisms have already been suggested throughout the literature, but are scattered among several works. We thus believe a compilation in a single work is also an important step in the study of this dynamical regime.

Though this is part of the work done in this dissertation, it is also part of the theoretical framework used for later, and so we decided to put this still in Part I.

6.1 DEFINITIONS IN THE LITERATURE

We can extract some categories from definitions of metastability, either explicit or implicit, in the literature of neuroscience. In the case of multiple definitions within one single work, we refer to them independently.

6.1.1 Definition 1a - Variability of states

Metastability here denotes the regime with a successive expression of the system's states over time. A state can be concretely given as a set of observables representing the system, like neuronal firing rates (La Camera et al., 2019). It can also be just an abstract concept (Váša et al., 2015; Alderson et al., 2020; Lee and Frangou, 2017; Werner, 2007b).

Since each of these states is successively replaced by another, none of them are equilibria. They are either transiently stable (were stable, but a change of parameters made them unstable), or are simply unstable states. In either case, they are generally called metastable states (metastates).

(La Camera et al., 2019) requires that the transitions between states be abrupt, "jump-like".

6.1.2 Definition 1b - Variability of activity patterns

Metastability here denotes the regime with a successive expression of activity patterns over time (Friston, 1997, 2000; Varela et al., 2001). Karl Friston says these patterns are "distinct, self-limiting and stereotyped" (Friston, 1997).

The patterns can be temporal or even spatial. In (Roberts et al., 2019), successive waves of electric potential are identified in whole-brain models, each denoting a spatial pattern, and their succession denoting metastability.

Each pattern could naturally reflect the system's state, so that definitions 1a and 1b could be equivalent. This view, however, can be more concrete, relying on the identification of patterns in the observations (activity) of the system, not on a potentially abstract state.

6.1.3 Definition 1c - Variability of synchronization or phase configurations

Metastability here refers directly to degrees of synchronization, or to oscillation phases. It can denote a (i) variability of the global degree of phase synchronization (Cabral et al., 2011; Deco et al., 2017) in time; (ii) variability of the states of phase configurations (Deco et al., 2017) in time; (iii) variability of synchronization between different node (Deco et al., 2017) in time; (iv) variability in the relative phases of nodes (Ponce-Alvarez et al., 2015) in time; (v) variability in the synchrony of each individual community in the network in time (Shanahan, 2010; Wildie and Shanahan, 2012). Promiscuity, which we define later, can be regarded here as a type of metastability.

On a topological scale, these definitions vary from a microscopic level (comparing nodes), to mesoscopic level (communities), to a macroscopic level (global).

If the degree of synchronization, or the configuration of phases, is considered to define a system state, then this definition is a specific case of 1a. If synchronization is considered an activity pattern, then this is a case of 1b also.

6.1.4 Definition 1d - Variability of regions in phase-space

Metastability here refers to a regime with transitions between regions in phase space (Hudson, 2017; beim Graben et al., 2019; Rabinovich et al., 2008; Cavanna et al., 2018). The trajectory of the system spends time in certain regions, and then moves to other regions. Mechanisms describing these are plentiful in dynamical systems theory (cf. Section 6.3.2).

The dynamical variables of the system, represented by a point in phase-space, represent its state (Cavanna et al., 2018; beim Graben et al., 2019). Thus, this definition is a phase-space view of definition 1a.

For example, (Rabinovich et al., 2008) considers the specific case where a state is a saddle, and metastability occurs due to a heteroclinic cycle.

6.1.5 Definition 1e - Variability of regions in energy landscape

Metastability here refers to a regime with transitions between local minima of energy, in an energy landscape. This is the definition in neuroscience closest to the one in physics. In this case, the system transitions from one state to another due to either external perturbations or to another dimension in the landscape (Shankar Gupta et al., 2018; Cavanna et al., 2018).

If each state or activity pattern has a value of energy, then this definition can be considered a specific case of the others.

6.1.6 Definition 2 - Regime for integration and segregation of neural assemblies

Metastability is often viewed as a dynamic regime that naturally implements the dual need for integration and segregation in the brain. The most common approach is to define metastability through one of the previous definitions, and consider integration-segregation as a consequence. However, (Fingelkurts and Fingelkurts, 2001, 2004) define metastability directly as the regime with this tendency of integration-segregation. According to their theory of Operational Architectonics, this tendency produces the cognitive or behavioral processes in the brain and,

therefore, metastability the regime behind them. These processes are constituted by a succession of different acts, each of which can is called a metastable state.

6.2 DISCUSSIONS

It is clear that most definitions (in number and frequency of occurrence) follow the common theme of variability in time of some concept, or, equivalently, the succession in time of aspects of this concept. This similarity allows us to equiparate them, or consider one a specific case of the other.

We can see that definitions 1a and 1b are the stronger candidates for a general definition. They include the other definitions, and are operational, as they rely on observations of the system, not on detailed knowledge of its phase space. In particular, 1b would be our preferred, as an activity pattern seems a more concrete idea than simply a state.

With these general definitions, the views on energy or synchronization are specific cases, dependent on the activity being measured and on the pattern that is found. The scale of observation and analysis is also important for the specific, practical view of metastability in each study. As seen in definition 1c, even considering synchronization, different views can be found in each scale. This relation between metastability and scales is further exemplified in Section 6.2.1 and in Chapter 9. In the former, we briefly view quantifiers for each scale. In the latter, we explore this metastability on the different levels of the topological scale.

6.2.1 Examples of metastability at different topological levels

We now offer some examples of metastability viewed at different levels of the topological scale.

6.2.1.1 Topological - macro level

The analysis in this case considers the whole network (all of its nodes). A common view of metastability follows definition 1c, as the variability in the degree of phase synchrony of the network. This is usually measured as the standard deviation $\sigma(R(t))$ in the Kuramoto order parameter $R(t)$ in time (cf. (5.12)) (Lee and Frangou, 2017; Alderson et al., 2020; Cabral et al., 2011; Deco et al., 2017; Kringelbach et al., 2015; Váša et al., 2015). Again, it is worth noting that some works may define metastability in a more general form, and then measure it in a specific way.

6.2.1.2 Topological - meso level

The analysis in this case considers a part of the nodes in the network, which are generally grouped in neural assemblies (also called clusters, or groups). As discussed in Section 1.9, neurons very commonly can be organized into assemblies, either anatomically or functionally, and these assemblies are quite important in several biological processes, which explain the ubiquity of this view.

One specific example of a neural assembly is the dynamic core (DC), defined as a "constantly evolving and transiently stable set of coordinated neurons" (Cavanna et al., 2018) (cf. Section 1.9). In the Dynamic Core Hypothesis, suggested by Tononi and Edelman, each conscious experience is associated with a DC. Metastability is seen as a mechanism leading to a "repertoire of dynamic core states" (Cavanna et al., 2018). This notion of metastable neural assemblies as "building blocks of brain organization" (Aguilera et al., 2016) is widespread in

neuroscience studies, like (Werner, 2007a; Buzsáki, 2010; Bassett et al., 2015; Cavanna et al., 2018; Werner, 2007b; Tognoli and Kelso, 2014).

Metastability is also seen to underlie the transient formation of clusters in (Ponce-Alvarez et al., 2015; Tognoli and Kelso, 2014; Kringelbach et al., 2015).

In (Shanahan, 2010; Wildie and Shanahan, 2012; Bhowmik and Shanahan, 2013), metastability is measured as the standard deviation of the Kuramoto order parameter calculated in clusters (or communities). The result is then an average over clusters, which characterizes a meso level analysis.

6.2.1.3 Topological - micro level

This analysis considers a few nodes of the network, only. In this case, one possibility is that the whole possible network is not being studied, only each node separately. In (Hudson, 2017), for example, the local field potential of regions of interest (macro level in a spatial scale) is taken and their spectral signatures are analyzed. The analysis is done for each region separately, constituting a micro level in a topological scale.

Another possibility is by studying only a few nodes at a time. In both (Tognoli and Kelso, 2014; Ponce-Alvarez et al., 2015), metastability is illustrated as changes in the relative phases between nodes of the network.

In each case, the view of metastability can follow from a general definition, as discussed.

6.3 MECHANISMS OF METASTABILITY

Considering for now a general definition, such as 1a or 1b, we can discuss and categorize some of the many mechanisms (Alderson et al., 2020; Deco et al., 2017; beim Graben et al., 2019) leading to a metastable regime. First, we need to distinguish between two cases:

1. Variation of system parameters
2. Intrinsic dynamics of the system

In the first, metastability occurs simply because the variation in the parameters caused the behavior of the system to also change; the second has many possible causes.

6.3.1 Variation of system parameters

One typical approach in the study of dynamical systems is to consider the long-term, asymptotic, behavior of a system, and to ignore its initial, transient, activity. This is generally done by studying the system's attractors, with the belief that the important dynamics lies in these regions, and not on the transition to them. This works extremely well for a variety of systems whose parameters can be kept constant, and the systems have time to settle.

As can be expected, this is not the case for the brain: both internally, with changes in neural conductances, strength of synaptic connections, neurotransmitter concentrations, etc., and externally, with changing hormone levels, varying inputs from the environment, etc. As a consequence, structures within the brain's phase space are perpetually changing (Friston, 1997). If the changes occur sufficiently fast, then the brain is also in a perpetual transient state (Friston, 1997).

These changes can lead to changes in the system's state (as defined before), in which case metastability arises due to variation of the system's parameters (be they slow or fast). One example of a drastic change in behavior due to changing parameters is a phase transition, a topic

of much study in neuroscience (Werner, 2007b; Fontenele et al., 2019; Ross, 2010). Another two are the phenomena of malleability and susceptibility, in which, roughly, small changes (even changes in a pair of neurons) in a neural network are able to radically change the network's behavior (like its synchronization properties) (Budzinski et al., 2020; Medeiros et al., 2019; Santos et al., 2018; Manik et al., 2017).

6.3.2 Intrinsic dynamics

The other possibility for generating metastability is due to the intrinsic dynamics of the system, happening even for constant parameters. We now provide examples of mechanisms leading to metastable behavior. These were introduced in Section 2.7.

6.3.2.1 Multistable quasi-attractors

The first possibility is chaotic itinerancy (cf. Section 2.7), also called attractor hopping (Kraut and Feudel, 2002). In this case, the system has several quasi-attractors (attractor-ruins) and it transitions between them (i.e. it hops between different quasi-attractors).

If each quasi-attractor is associated with a distinct state or activity pattern, then the system is metastable, as proposed in (Hudson, 2017; Shanahan, 2010).

6.3.2.2 Multiple unstable attractors

The second possibility is unstable attractors (cf. Section 2.7). In this case, the system does have Milnor attractors, but these are surrounded by the basins of attraction of other attractors, not theirs, so arbitrarily small perturbations can induce hopping between attractors (Timme et al., 2002). If each unstable attractor is associated with a distinct state or activity pattern, then the system is metastable.

6.3.2.3 One attractor

In this case, the system has one global attractor (it could actually have more, but one is enough). This attractor then has a very inhomogeneous measure, so that the attractor manifold can be divided in various submanifolds. The system spends some time in each submanifold, and transitions naturally between them (Friston, 1997). Thus, the submanifolds are analogous to the quasi-attractors in the first case, but here the trajectory does not leave the attractor.

Again, if each submanifold is associated with a distinct state or activity pattern, then the system is metastable. This mechanism is proposed by Friston (Friston, 1997).

An additional possibility is that the submanifolds can be further subdivided into subsubmanifolds, leading to a hierarchical metastability. This has been proposed in (Cavanna et al., 2018) as a possibility reflecting hierarchical relations in the system's scales.

An example of the above case is a heteroclinic cycle (a sequence of saddles connected to each other) (cf. Section 2.7.3). If each saddle corresponds to a different state, then the system is metastable, as proposed in (Rabinovich et al., 2008).

6.3.2.4 No attractor

In this case, the system has no global attractor, only a quasi-attractor (or attractor-ruin). This attractor-ruin attracts the trajectory temporarily, before it escapes and wanders in phase space until eventually approaching the ruin again and repeating the process. This is the case, for example, of type I Pomeau-Maneville intermittency, in which the trajectory is temporarily

attracted to the region where the saddle and node collided. It can also be the case of on-off intermittency, in which a before-stable attractor loses transversal stability, and orbits can escape.

If each region of phase space is associated with a distinct state or activity pattern, then the system is metastable (as it traverses the phase space, it changes states). This mechanism is defended mainly be Kelso and Tognoli (Tognoli and Kelso, 2014), who state that the system has "no attractors, only attracting tendencies" (Tognoli and Kelso, 2014).

Part II

Results

In the first part of this dissertation, we discuss the theoretical framework needed to understand and analyze the networks of bursting neurons we use. The interest in these networks is twofold: from a dynamical systems point of view, their rich dynamics is very interesting; from a neuroscience point of view, they serve to illustrate the discussions we made about metastability in Chapter 6 and the importance of studying different scales of the system.

In the first part of the results (chapters 7, 8), we focus on the dynamics of the network. We start analyzing its degree of phase synchronization (PS) and variabilities. The former gives us the general behavior of the network, with transition to phase synchronization as the coupling strength increases. The latter quantifies how neurons in the network differ dynamically and suggests promiscuity, defined as the intermittent changes in the phase differences between neurons. It is named this way because neurons may stay together with fixed phase differences for some time, but this inevitably changes after a while. Promiscuity is directly measured by the average drift. Then, its effects on cluster formation are studied. The analysis of clusters then gives us in-depth detail on the PS of the network, and lets us see promiscuity leading to changes in the composition of clusters in the network. We also take advantage of this model and study the network behavior at three different firing modes. At temperature 37 °C, an uncoupled neuron has a chaotic bursting mode, while for 38 °C and 40 °C a neuron has regular bursting, with 38 °C having two inter-burst intervals and 40 °C having just one (cf. Fig 3.6).

In Chapter 9 we explore the network's synchronization behavior in more detail. Adopting a specific definition of metastability, we use this study to illustrate how quantifiers of metastability for different scales can behave differently. We study the pairwise synchronization in the network R_{ij} (micro level), the cluster behavior $\mathcal{P}$ (meso) and the average synchronization $\langle R \rangle$ (macro level). We also briefly characterize the statistical properties of both the pairwise and network synchronization.

In all cases, a transient time of $t_0 = 300\,\mathrm{s}$ was disconsidered, and a total execution time of $t_f = 1300\,\mathrm{s}$ was used for analysis, unless otherwise stated. This is enough to overcome the transient behavior in all cases.

7 PHASE SYNCHRONIZATION, VARIABILITY AND PROMISCUITY

7.1 DEGREE OF PHASE SYNCHRONIZATION AND VARIABILITY

We start our analysis by looking at the average degree of phase synchronization (PS) of the network, calculated through the time-averaged Kuramoto order parameter $\langle R \rangle$ (5.13), as a function of the coupling strength. This is shown in the first row of Fig 7.1, for $\epsilon \in [0, 0.008]$. Panel (a) (37 °C) exhibits a monotonic transition to PS, common in several other models like Kuramoto oscillators (Kuramoto, 1984; Boccaletti et al., 2002; Arenas et al., 2008). In panel (b) (38 °C), there is a local maximum of synchronization for weak coupling, and a second transition for stronger coupling. This has also been observed in small-world topologies (Xu et al., 2018; Boaretto et al., 2018b; Budzinski et al., 2019c). In panel (c) (40 °C), the previous local maximum is replaced by a global maximum, which spans a wider interval of ϵ and in which even the spikes within bursts can be synchronized (Budzinski et al., 2019c). We see therefore that the networks have very different behaviors for weak coupling, ranging from desynchronization to burst synchronization and then to almost complete synchronization depending on the temperature (firing mode). However, for strong coupling, the behavior is similar across temperatures, with phase-synchronized networks.

Next, we study the coefficients of variability $\mathrm{CV_t}$ and $\mathrm{CV_e}$ (cf. Section 5.5), measuring the average dispersion of inter-burst intervals IBIs across time and across the network, respectively. These are in the second row, where we can first see that both have very similar values in all cases. For very weak coupling ($\epsilon < 1 \times 10^{-3}$), variabilities are very similar to the uncoupled case, as the coupling is not strong enough yet to change the neurons' dynamics. In 37 °C, variabilities start high (following the highly variable chaotic dynamics), start to decrease as the network transitions to PS and then increase again at very strong coupling ($\epsilon > 7 \times 10^{-3}$). For 38 °C, variability also goes down as the system transitions to the first PS states, reaching a minimum as $\langle R \rangle$ is maximal. These states are highly phase-synchronized with relatively low variability. Then, as the network desynchronizes the variabilities also increase, reaching a maximum as the $\langle R \rangle$ is minimum. The second transition to PS is then similar to the transition in 37 °C. For 40 °C, variabilities start very close to zero (following the uncoupled neuron, with zero variability), and the network is very strongly synchronized. As coupling increases, desynchronization happens, similar to 38 °C, with maximum variabilities at minimum $\langle R \rangle$. The second transition is then also similar to 37 °C and 40 °C. Variabilities appear to be equal here due to the neurons being identical, as making the neurons non-identical makes it so that the two variabilities differ.

In the third row we show the IBIs of the neurons in the network, color-coded according to the logarithmic frequency $\log(\lambda)$ in which they are observed in the simulations. Due to this log scale, one has to be careful when trying to assess the variabilities from these plots. Again, for all temperatures, the uncoupled dynamics can be seen to continue to influence the network behavior, as the IBIs for the uncoupled case remain highly visited, especially for weaker coupling ($\epsilon < 3 \times 10^{-3}$). These results, along with return maps $\mathrm{IBI}_k \times \mathrm{IBI}_{k+1}$ (Section 8.1) show also that for 38 °C and 40 °C the first phase synchronized states have more periodic characteristics than the final PS states, whose chaotic dynamics is more irregular. For all temperatures, this increase in chaoticity (reflected in the increase of IBIs) for strong coupling is an indication of the stronger role of the coupling term, which starts dictating the dynamics, explaining why that final transition is similar for the three temperatures.

These results therefore show a clear negative correlation between the degree of PS and the coefficients of variability for weak coupling, where we see that the influence of the individual, uncoupled dynamics is highest, as reported in similar networks (Budzinski et al., 2019b). Behavior at strong coupling is then similar for the three temperatures, as the coupling dominates the dynamics.

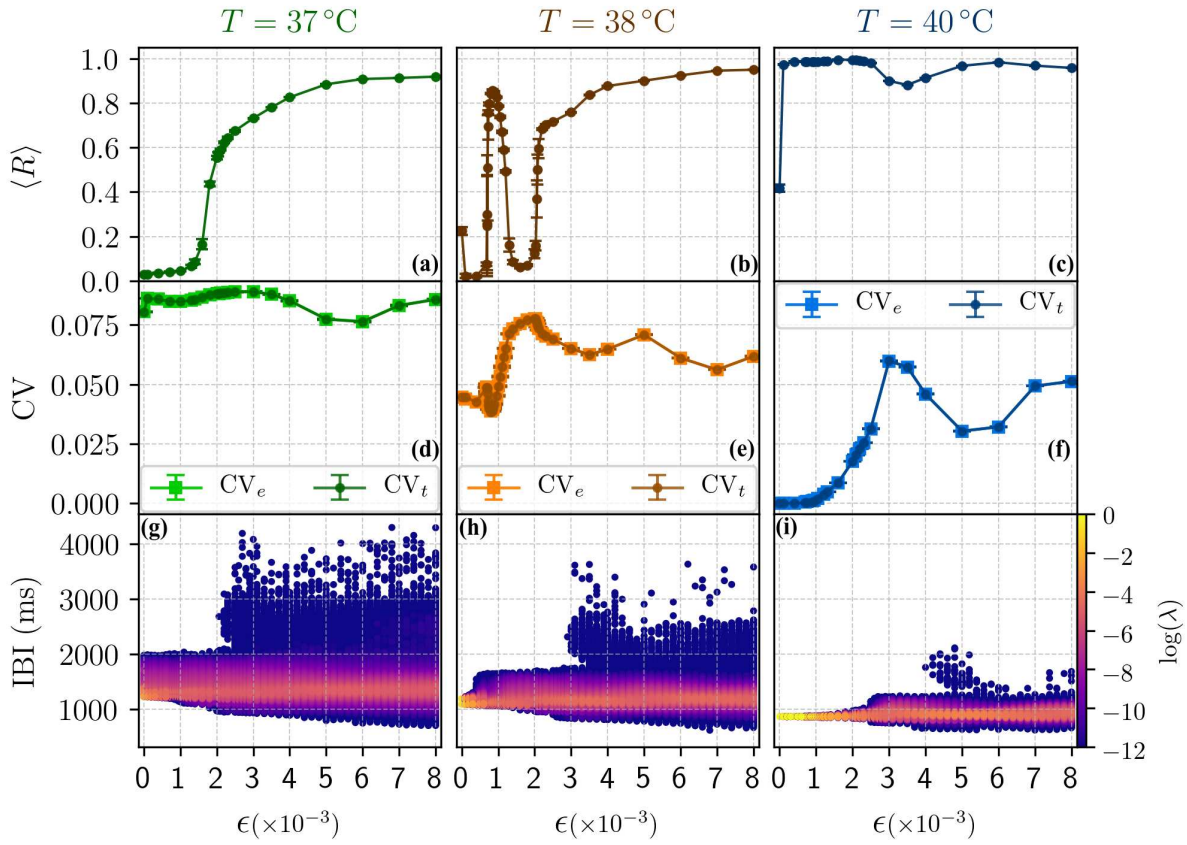

Figure 7.1: **Synchronization and variabilities in the network**. Each row corresponds respectively to the average degree of phase synchronization $\langle R \rangle$, the two variabilities $\mathrm{CV_e}$ and $\mathrm{CV_t}$, and the inter-burst intervals (color-coded by their frequency in the simulations). In the three cases (in each column), a transition from desynchronization to phase synchronization is observed. In the first column (37 °C), the transition is a common monotonic one; in the second and third columns (38 °C, 40) the transition is nonmotonic: a first phase-synchronized state appears at weak coupling, followed by desynchronization and later synchronization at strong coupling. For 40 °C the first PS state is very phase-synchronized. The two variabilities are also seen to be anti-correlated with the degree of phase synchronization for weak coupling. Results are given by an average over 5 initial conditions, with errorbars containing the standard deviation over them.

7.2 PROMISCUITY

The nonzero temporal variability shows that, for any neuron, different IBIs occur throughout time from the pool of possible IBIs. The way IBIs occur is of course dictated by the equations of the system, and may be so complicated as to seem random. This is corroborated by the return maps Fig 8.1.

The nonzero ensemble variability $\mathrm{CV_e}$ then shows that, for each burst, different IBIs occur for different neurons. This means the neurons are *dynamically asymmetrical* over short windows (e.g. across a few bursts). This is due to two effects: (i) different in-degrees (number of

received connections) (cf. Fig 5.1) and (ii) the neurons' intrinsic, uncoupled, dynamics. Even if the network were symmetrical, and degrees were homogenous, the asymmetry would still be observed: neurons would be identical, so over a (sufficiently) long time window, the same set of IBIs would occur, but, for short windows, IBIs would still be generally different, as each neurons' trajectory differs in phase space. This dynamical asymmetry also means that phase relations between neurons must change in time, as different IBIs are chosen. In this case, even highly phase-synchronized states do not have permanently phase-locked neurons if the ensemble variability is nonzero. In other words, ensemble variability indicates promiscuity.

7.2.1 Drift

To verify the previous affirmation, we calculated the average drift Δ (cf. section 5.7), measuring how much, on average, the differences in burst times change between neurons. A null drift Δ means relative phases (i.e. phase differences) between neurons in the network are constant throughout time, while higher drifts mean higher rates of change in the relative phases.

We show the results in Fig 7.2, with the drift Δ as a function of the coupling strength ϵ for the three temperatures: 37 °C (green), 38 °C (brown) and 40 °C (blue). Our predictions are confirmed: the drift Δ follows the ensemble variability CV_e (cf. 7.1), showing that phase relations within the network are labile. This is *promiscuity*, with higher Δ indicating neurons are, on average, more promiscuous. An interesting observation for 40 °C is that Δ is very nearly

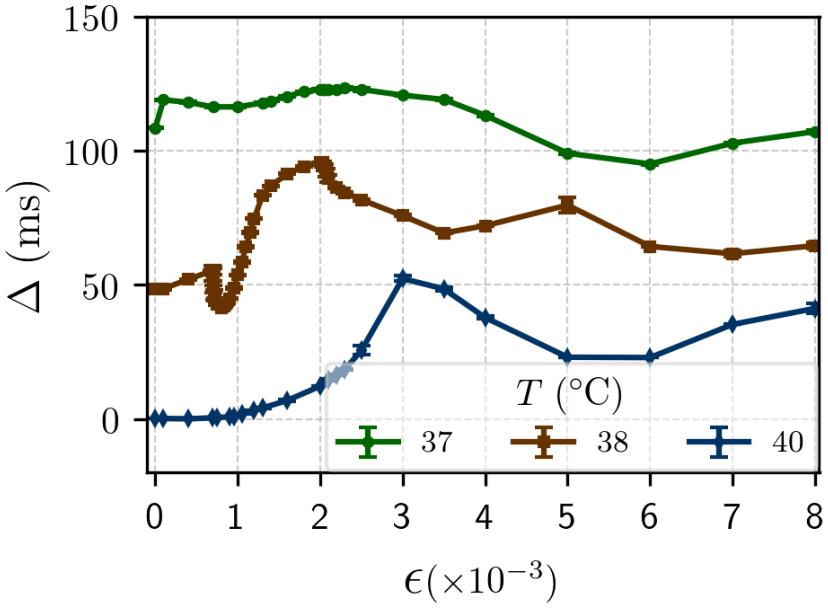

Figure 7.2: **First measure of promiscuity.** The average drift Δ, measuring average rate of change in neurons' relative burst times of the network is shown as a function of the coupling strength ϵ for temperatures $T = 37\,°C, 38\,°C, 40\,°C$. The degree of promiscuity is seen to follow the ensemble variability CV_e (cf. Fig 7.1 panels (d),(e),(f)) and is relatively high even for strongly synchronized states. Results are given by an average over 5 initial conditions, with errorbars containing the standard deviation over them.

0 until $\epsilon = 1 \times 10^{-3}$, when it starts to increase. The average degree of PS remains high until $\epsilon = 2.3 \times 10^{-3}$ (cf. Fig 7.1), so we see that this first phase synchronized state can be subdivided into a region with no promiscuity and one with some promiscuity. This is again similar to 38 °C, with the difference that $\langle R \rangle$ does not decrease.

For all temperatures, the strongly coupled regime, though highly phase-synchronized, is considerably promiscuous. Also, in both 38 °C and 40 °C the first PS states have smaller promiscuity than for strong coupling. This is an interesting behavior: stronger coupling makes neurons less phase-locked in this case.

7.2.2 Clustering

To further understand this behavior, we analyze clustering in the network. Our algorithm groups neurons according to their phases (cf. Section 5.8). In this way, neurons with similar phases are put in the same cluster, so promiscuity should reflect in more frequent changes of cluster composition (i.e. more neurons leaving and entering the clusters).

We start by examining only the biggest cluster (BC, cf. Section 5.8.5.1). That is, for all times $\{t_k\}$, separated by 1000 ms, we identify the clusters, select the biggest in each time, and analyse its behavior. We start by showing the time-averaged size of the BC $\langle |C_{\mathrm{BC}}(t_k)| \rangle_k$ in the first row of Fig 7.3 as a function of the coupling strength. Each panel corresponds to a temperature, and in any panel each curve corresponds to a different threshold Φ_{th}. The average cluster size follows the average degree of phase synchronization (cf. Fig 7.1), as more synchronized networks have more neurons with similar phases. By changing the threshold Φ_{th} we can control how similar neurons in the cluster have to be, with smaller thresholds meaning more similar. This explains why smaller thresholds lead to smaller clusters. The important observation is that the cluster size does not decrease at the same rate for every coupling strength (as the threshold is decreased). For 37 °C, the desynchronized region ($\epsilon < 1.2 \times 10^{-3}$) decays faster than the synchronized region, as could be expected. For 38 °C, the previous observation is still true, as the two desynchronized regions (before and after the local maximum) decay faster. The interesting behavior is that the first phase synchronized states (around the local maximum) decay more slowly than for the second phase synchronized states (strong coupling). In fact, the first phase-synchronized states start, at $\Phi_{\mathrm{th}} = 0.3$, with smaller clusters compared to the second states. As the threshold is decreased this starts to reverse, and the first PS states have bigger clusters. This indicates that the first PS states have more neurons very out-of-phase (explaining the start), but also more neurons very in-phase compared to the second PS states (explaining the reversion). This is a difficult level of analysis to obtain with other tools we used, or by visually inspecting raster plots, but is possible through this analysis.

For 40 °C, results are similar: desynchronized regions decay faster than the rest, and first PS states decay more slowly than the second PS states. A local maximum of the cluster size is visible for weak coupling ($\epsilon \approx 1 \times 10^{-3}$), the same region observed for 38 °C, but not visible through $\langle R \rangle$.

The previous analysis provided details about the PS of the neurons in the networks. Now we want to measure more directly how the cluster composition changes. To do this, we take a number $\mathcal{T}$ of intersections between clusters subsequent in time (cf. Section 5.8). Starting from a cluster at time t_k, we denote the intersections $C_{BC,\mathcal{T}}(t_k) \equiv C_{BC}(t_k) \cap C_{BC}(t_{k+1}) \cap \cdots C_{BC}(t_{k+\mathcal{T}})$. With this, we can examine how the average size of the intersections $C_{BC,\mathcal{T}}$ decreases with the number of intersections $\mathcal{T}$. If this size remains constant, the composition does not change. If it does, then the rate of decrease gives the rate of composition change. The second row of Fig 7.3 shows this analysis done for threshold $\Phi_{\mathrm{th}} = 0.1$ (a representative case, which captures all the relevant behaviors). Each line represents a coupling strength ϵ, with the color chosen according to the colormap in the figure.

Several coupling strengths have a linear decay in the figure. Since the y-axis is in logarithmic scale, this means the cluster intersections decay exponentially. This can be explained with the simple model described in Section 5.8.5.2: assuming probability p_{BC} of

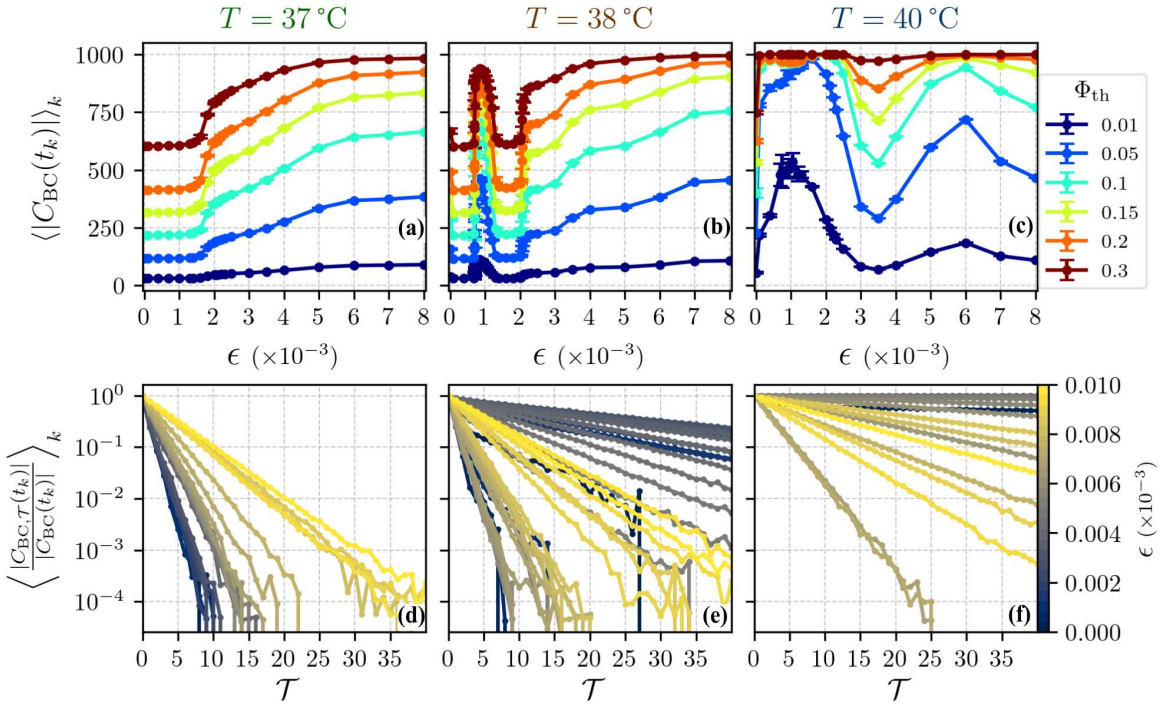

Figure 7.3: **Analyses of the biggest cluster.** The first row contains the average size $\langle |C_{\mathrm{BC}}(t_k)| \rangle_k$ of the biggest cluster as a function of coupling strength ϵ for different clustering thresholds Φ_{th}. Second row shows the normalized size of the cluster intersections in log scale as a function of the number of intersections $\mathcal{T}$ for a fixed threshold $\Phi_{th} = 0.1$ and various coupling strengths. The cluster size follows the profile of the degree of phase synchronization, and shows differences in the PS characteristics of different ϵ. The linear decay in (b) means the normalized cluster intersections follows an exponential decay. Results in the first row are an average over 5 initial conditions with errorbars containing the standard deviation over them; the second row is an representative example for one initial condition only.

staying in the cluster (C_{BC}) from one time t_k to another t_{k+1} is the same for all times $\{t_k\}$, then $C_{BC,\mathcal{T}}(t_k) = p_{BC}\ C_{BC,\mathcal{T}-1}(t_k) = \cdots = p_{BC}^{\mathcal{T}} C_{BC}(t_k)$. The linear decay is not present (thus, the model does not work), for some couplings strengths. In Fig 9.2, we will see that these cases are where the network's degree of synchronization $R(t)$ is intermittent.

From the figure, we can see that, for example, for 38 °C the first PS states have much smaller decays compared to the second PS states. Thus, the former are less promiscuous than the latter. This analysis could be done for other cases but, instead of relying on this visual inspection, we can quantify the average rate of decay (i.e. of cluster composition change). Following Section 5.8.6, we can calculate the average proportion (probability) $\mathcal{P}_{BC}$ of neurons leaving the cluster. This rate of change in cluster composition can be seen as an indirect measure of promiscuity. This result is displayed in Fig 7.4 as a function of coupling strength and the three temperatures.

Promiscuity measured as rate of change in cluster composition agrees with the promiscuity measured by the mean drift Δ, and both agree with the ensemble variability $\mathrm{CV_e}$. This analysis, however, brings additional details. First, smaller thresholds (i.e. higher similarity between neurons in the cluster) lead to higher promiscuity $\mathcal{P}_{BC}$, indicating that more in-phase neurons tend to stay that way for less time or, in other words, more exclusive clusters change their members more frequently. This observation is in line with the previously mentioned idea that, each time neurons burst, different IBIs occur, thereby making the neurons' relative phases evolve intermittently.

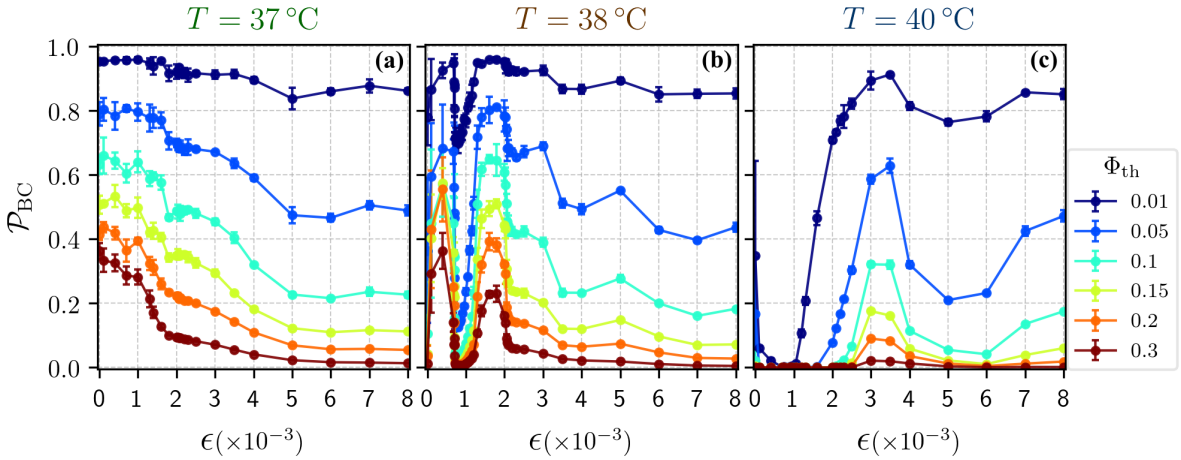

Figure 7.4: **Promiscuity measured as rate of change in the biggest cluster's composition.** The average proportion $\mathcal{P}_{BC}$ (cf. Section 5.8.6) of neurons leaving the BC is plotted as a function of the coupling strength ϵ for the three temperatures 37 °C, 38 °C, and 40 °C for different cluster thresholds Φ_{th}. 37 °C follows a more common behavior, with promiscuity decreasing (though not vanishing) as ϵ increases. Both 38 °C and 40 °C have nonmonotonic changes in the promiscuity. In all cases, this analysis fits well with the analysis via Drift Δ and ensemble variability CV_e. Results are given by an average over 5 initial conditions, with errorbars containing the standard deviation over them.

Also, again changes in the quantifier as the threshold Φ_{th} varies do not occur homogeneously for all ϵ. Taking as an example 38 °C, for high threshold Φ_{th} both the first synchronized states (local maximum at Fig 7.1(b), $\epsilon \approx 1 \times 10^{-3}$) and the second synchronized states (after final transition, at $\epsilon > 4 \times 10^{-3}$) have very similar, close-to-zero promiscuity. This result is trivial for the second PS states since the cluster sizes are very close to network size, but not so for the first PS states. We see that, decreasing Φ_{th}, the first PS are clearly less promiscuous than the second PS states (and, in fact, all other ϵ).

For 40 °C, a similar behavior occurs, but with enhanced contrast: promiscuity is much smaller in the first PS states. In fact, as seen in the drift Δ (cf. Fig 7.2), the first PS states ($\epsilon < 2.5 \times 10^{-3}$) can be subdivided in two states: one with near zero promiscuity (and maximum cluster size in Fig 7.5), at $0 < \epsilon \leq 1 \times 10^{-3}$ (very near to the first maximum for 38 °C), and a second part with higher promiscuity (though still lower than other ϵ) at $1 \times 10^{-3} < \epsilon < 2.8 \times 10^{-3}$. These two parts have different characteristics, even though the average degree of PS $\langle R \rangle$ is almost the same. For 37 °C, behavior is more uneventful: higher coupling is less promiscuous for all thresholds. In all temperatures, maximum promiscuity occurs at the desynchronized states, either before or after the transition to the first PS states in the case for 38 °C and 40 °C.

Until now, we have only analyzed the biggest cluster, but for some coupling strengths there are other clusters. Figure 7.5 shows the size of the clusters for coupling strengths and temperatures at a fixed threshold of $\Phi_{th} = 0.1$.

We see that more clusters emerge when the average PS of the network is lower. Our main discussion so far focused on synchronized states, for which only one cluster (the biggest) is found on this threshold. Higher thresholds have even fewer clusters, as one cluster is generally large, and lower thresholds have more clusters, all with similar sizes. This is discussed in Chapter 8 in Fig 8.2. In any case, we have to consider all clusters to be more accurate.

To do this, the idea is to calculate the probability of neurons leaving each cluster and average over all clusters to obtain $\mathcal{P}$. The procedure is similar to the biggest cluster case, but with additional details explained in Section 5.8 and discussed further in Section 8.2. After these

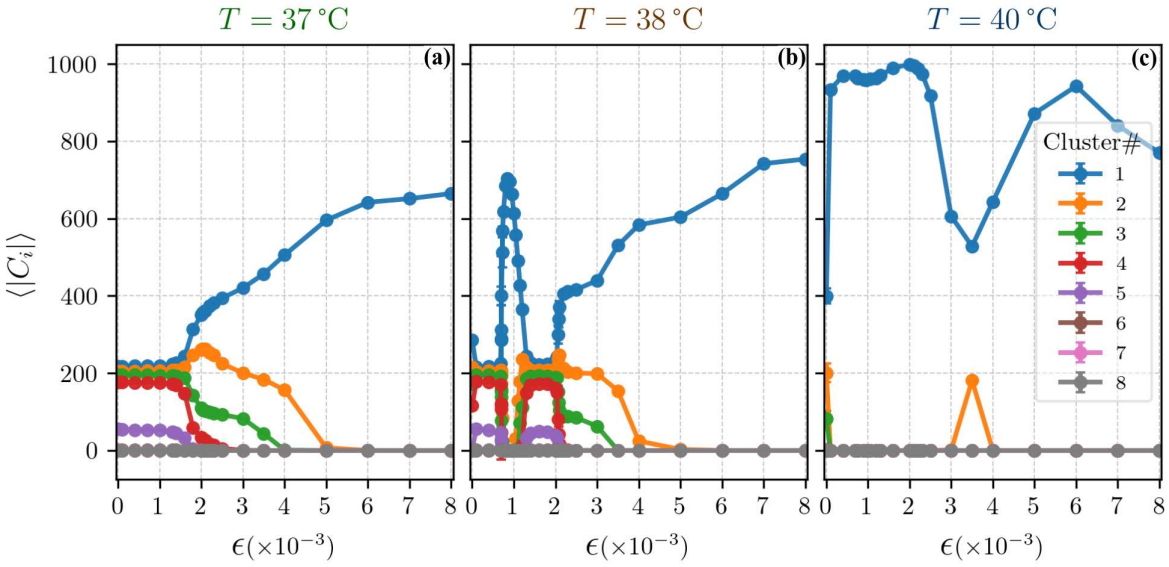

Figure 7.5: **Sizes of clusters.** The average size of each cluster found in the network is shown as a function of coupling strength ϵ and for the three temperatures 37 °C, 38 °C and 40 °C for a fixed threshold Φ_{th}. This is a representative case to illustrate how the sizes and number of these clusters vary in each case. For more thresholds, refer to Fig 8.2. We see that more desynchronized regions tend to have more clusters, with more similar sizes. Errorbars depict the standard deviation over 5 initial conditions, and each point is an average over time and over the initial conditions.

considerations, we plot the resulting average probability of neurons leaving clusters in Fig 7.6. Results show that the biggest cluster case under-estimated the probability by not considering the other clusters, but the behavior is nonetheless similar. Again, promiscuity follows the average drift Δ (cf. Fig 7.2) and the ensemble variability CV_{e} (cf. Fig 7.1) and smaller thresholds Φ_{th}, leading to stricter clusters, are associated with higher promiscuity. For 37 °C, strong coupling reduces promiscuity. For 38 °C, the second synchronized states have smaller $\mathcal{P}$ for $\Phi_{\text{th}} = 0.3$, as the cluster encompasses the whole network, but have bigger $\mathcal{P}$ (are more promiscuous) for smaller Φ_{th}. This again shows that strong coupling brings neurons closer together (e.g. bigger cluster sizes) but is unable to keep their phase relations. The most promiscuous regions are the desynchronized ones, both before and after the local maximum. 40 °C is similar to 38 °C, and the main difference to the biggest cluster case is that $\mathcal{P}$ is not very near zero for $\Phi_{\text{th}} = 0.01$ in the first part of the first synchronized states ($0.5 \times 10^{-3} < \epsilon \leq 1 \times 10^{-3}$).

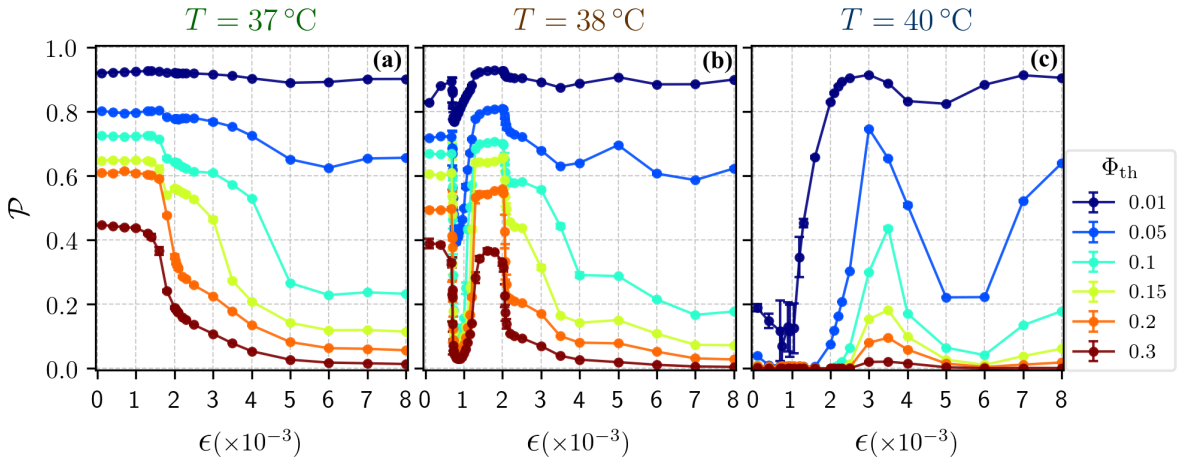

Figure 7.6: **Promiscuity measured as rate of change in the clusters' composition, averaged over all clusters.** The average probability $\mathcal{P}$ of neurons leaving the clusters is plotted as a function of of the coupling strength ϵ for the three temperatures 37 °C, 38 °C, and 40 °C for different cluster thresholds Φ_{th}. The result and conclusions are very similar to the analysis made with the biggest cluster (cf. Fig 7.4). Results are given by an average over 5 initial conditions, with errorbars containing the standard deviation over them.

8 ADDITIONAL SUPPORTING RESULTS

8.1 RETURN MAPS

As mentioned in the previous chapter, the return maps $\mathrm{IBI}_k \times \mathrm{IBI}_{k+1}$ provide some information regarding the periodicity behavior in the network. In Fig 8.1, we show the return maps for the network as a function of the coupling strength ϵ for the three temperatures 37 °C, 38 °C, 40 °C (colored green, brown and blue, respectively). Starting at the uncoupled dynamics, we again see that 37 °C has chaotic behavior, and 38 °C and 40 °C are regular with two and one IBIs, respectively. Coupling is then increased to $\epsilon = 0.00084$, the local maximum of synchronization for 38 °C (cf. Fig 7.1). We see the increase of irregularity in all cases, with 38 °C having similar dynamics to the chaotic 37 °C, and 40 °C slightly nonperiodic. For $\epsilon = 0.008$, a further increase of irregularity occurs, with the dynamics becoming very different to the previous two cases, but also similar across the temperatures. One can see, however, that the more periodic case (40 °C) has the less spread in IBIs in this case, which can lead to the prediction that the network in this case is less promiscuous and more phase-synchronized (indeed observed in figures 7.1 and 7.6).

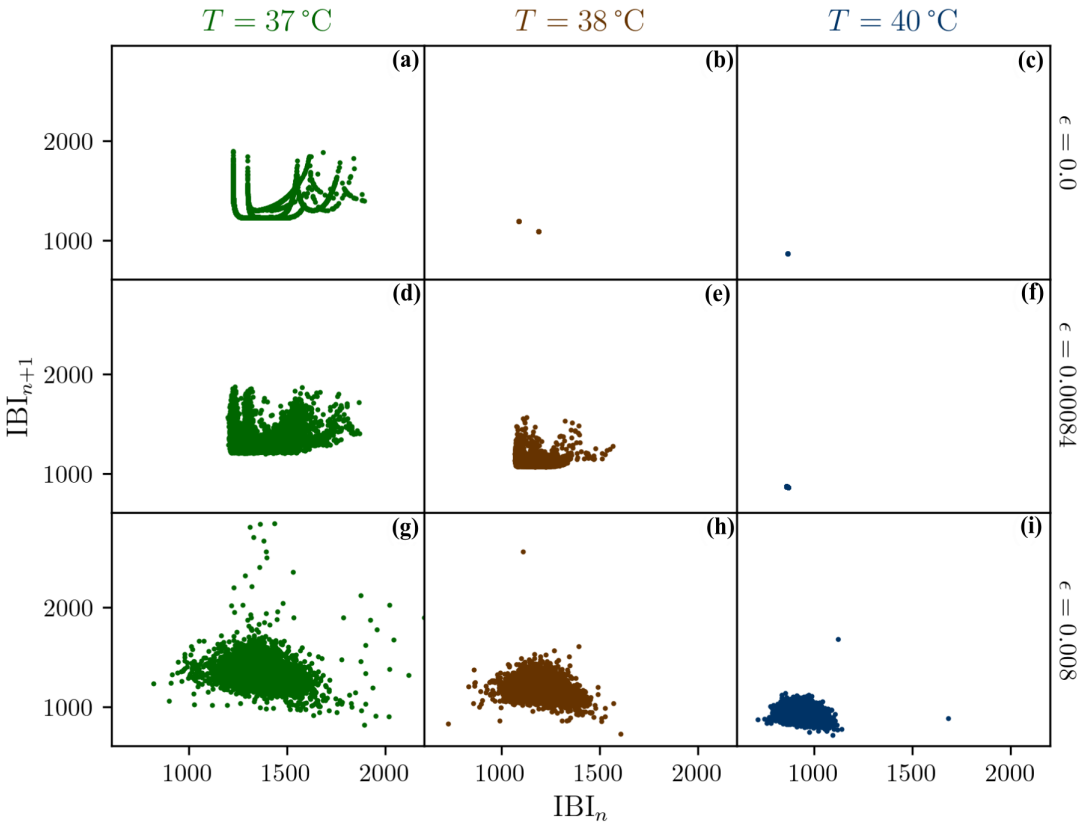

Figure 8.1: **Changes in the regularity of the network behavior.** The return maps of the IBIs for all neurons $\mathrm{IBI}_k \times \mathrm{IBI}_{k+1}$ are shown for the three temperatures 37 °C, 38 °C, 40 °C and three coupling strengths $\epsilon = 0$ (uncoupled) $\epsilon = 0.00084$ (local maximum of $\langle R \rangle$ at 38 °C) and $\epsilon = 0.008$ (strongest coupling strength). We see a clear increase in irregularity, and decrease in similarity to the uncoupled case, as ϵ increases.

8.2 CLUSTERS

We now complete the discussion about clusters started in the results section, getting to more details. First, we show the sizes of all 8 clusters for the three temperatures $T = \{37, 38, 40\}$°C (along columns) and three cluster thresholds $\Phi_{\text{th}} = \{0.01, 0.1, 0.3\}$ (along rows) averaged over 5 initial conditions and with standard deviation in the errorbars. First, we would like to remember (cf. Section 5.8) that, for each time, clusters are indexed according to their sizes. In the first row ($\Phi_{\text{th}} = 0.01$), we see that cluster sizes are similar for most coupling strengths. The exception is for 40 °C in the first part of the first phase-synchronized states (ϵ around $[0.0001, 0.001]$), where the network is very synchronized and the biggest cluster dominates. The similarity in cluster sizes could lead to ambiguity in determining which cluster is which through time. As an example, say a group of neurons is in one cluster (say, cluster 1) at some time t_k. At the next time t_{k+1}, this group could be in another cluster (say, cluster 2). This would happen if, for example, another cluster increased in size, dislocating cluster 1 at t_k to cluster 2 at t_{k+1}. This is much more likely to occur with similarly sized clusters, which mainly happens for $\Phi_{\text{th}} = 0.01$.

For $\Phi_{\text{th}} = 0.1$ (shown also in the results section), we see that clusters are similarly sized only for the most desynchronized regions of coupling strengths, and even fewer clusters are present (generally $1, 2, 3, 4$). For higher threshold $\Phi_{\text{th}} = 0.3$, only one cluster is found, and no problem of similar sizes occurs.

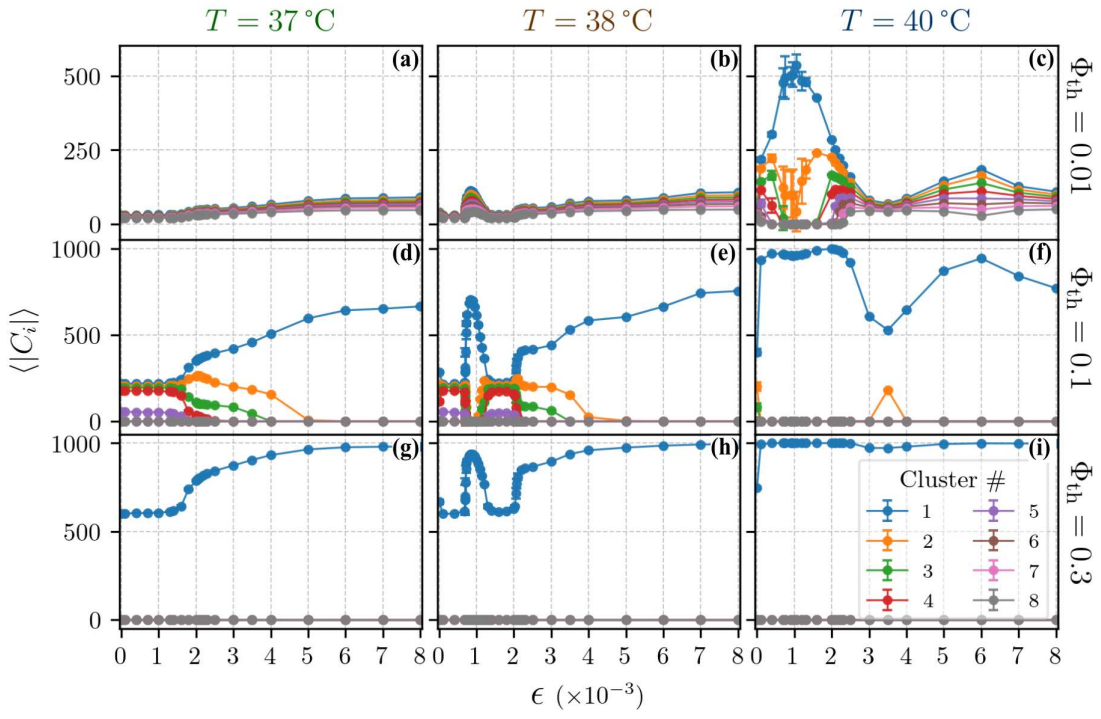

Figure 8.2: **Clusters' sizes.** The average size of all clusters is plotted for the three temperatures 37 °C, 38 °C, 40 °C and three cluster thresholds $\Phi_{m}rth = 0.01$, $\Phi_{\text{th}} = 0.1$, $\Phi_{\text{th}} = 0.3$ as a function of the coupling strength ϵ. Each cluster is colored according to the legend shown in the last panel. Average is taken over time and over 5 initial conditions, with the errorbars showing the standard deviation over them. Results are given by an average over 5 initial conditions, with errorbars containing the standard deviation over them.

As discussed in the cluster analysis section of the Theoretical Framework part (Section 5.8), we reduce significantly the problem of similar sizes by analyzing the maximum intersections between clusters. Returning to the previous example, we would identify that cluster 1 in time t_k

became cluster 2 at t_{k+1} because the intersection between these two would be bigger than the intersection with cluster 1 at t_{k+1}. To verify if this eliminates ambiguity (i.e. not knowing how to compare clusters at different times), we look at the transition proportions

$$p_{ij} \equiv \frac{|C_i(t_k) \cap C_j(t_{k+1})|}{|C_i(t_k)|} \tag{8.1}$$

between each cluster. In Fig 8.3, we plot these proportions for 10 times, with the maximum proportion for each cluster (i.e. $\max(p_{ij})_i$) in bigger sizes. Each panel illustrates the typical case that the maximum intersections are generally significantly bigger than the others for each cluster (i.e. for each color, bigger markers are significantly above smaller markers). This happens even in regions where cluster sizes are similar, indicating that there is no ambiguity in the calculation of the promiscuity measure $\mathcal{P}$.

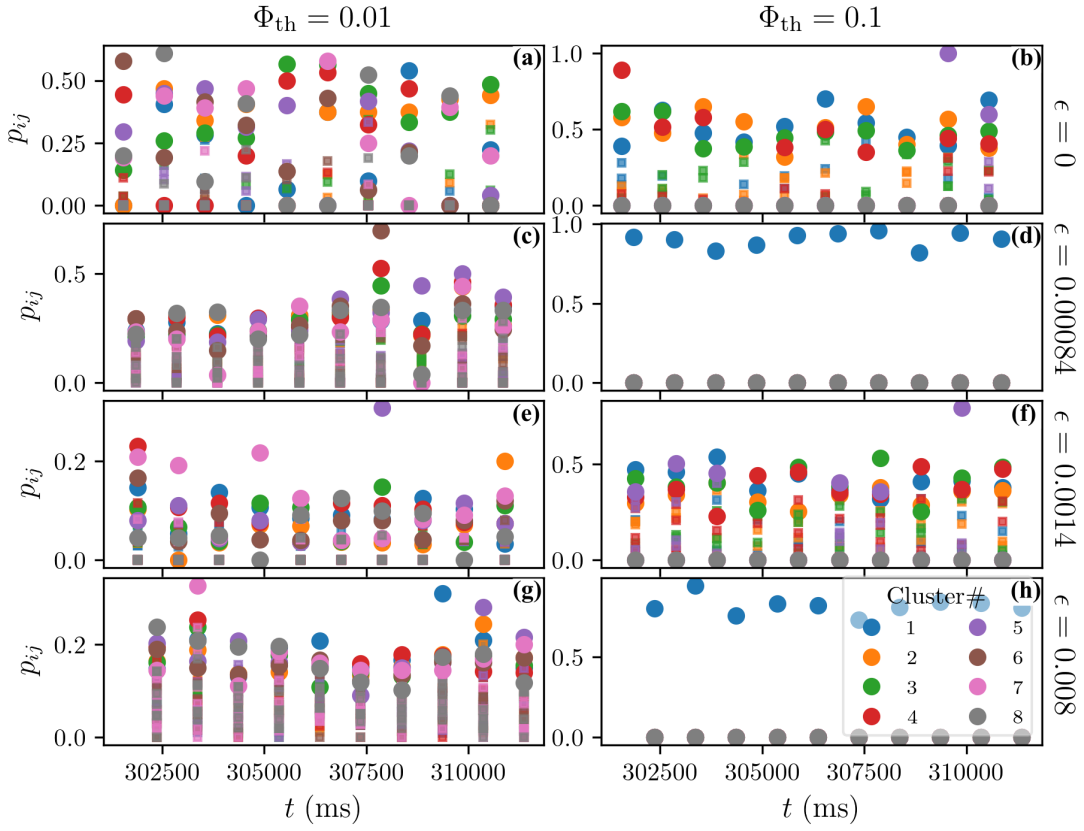

Figure 8.3: **Example of transition probabilities between clusters.** Probabilities p_{ij} of transitions between neurons from cluster i to cluster j from times t_k to the next t_{k+1} are shown for 10 times for $T = 38\,^{\circ}\text{C}$. Columns correspond to $\Phi_{th} = 0.01$ and $\Phi_{th} = 0.1$, respectively and lines to $\epsilon = 0.0$, $\epsilon = 0.00084$, $\epsilon = 0.0014$, $\epsilon = 0.008$. We see that the maximum probabilities of transitions for each cluster i are generally well above the others, meaning there is no ambiguity in calculating the probabilities of neurons staying in each cluster.

We remark also that the reliability of the cluster analysis results is further enhanced by noting that they fit with independent measures, like ensemble variability CV_e, drift Δ, cluster measures without similarity in clusters sizes, and with other cluster analysis measures not shown in this dissertation.

The next part of our analysis is to examine differences between each neuron in their probabilities of staying in clusters. Neurons are parametrically identical in the network, but

the in-degrees differ (cf. Fig 5.1), so some asymmetry can be expected. For each neuron, we calculate the number of times in which they stayed in the biggest cluster. Then, we calculate their probability of staying in the BC as the number of times they stayed in the cluster divided by the number of times in which they were in the BC and average over all times. In Fig 8.4, we plot the histogram of the probabilities of each neuron for a few cases. For $T = 37\,^{\circ}\mathrm{C}$, with uncoupled chaotic neurons, the distribution appears similar to Gaussian. For the first three coupling strengths ϵ, in which the network is desynchronized (cf. Fig 7.1), the distribution does not change much. For strong coupling at $\epsilon = 0.008$, for which the network is synchronized, the distribution shifts to the right, and neurons's probabilities become more similar. For $T = 38\,^{\circ}\mathrm{C}$, in which uncoupled neurons are periodic, the probability distribution indicates most neurons never stay in the cluster, while some do, and for differing times. This is for reference, and is a result of the periodicity of the neurons. Increasing coupling to $\epsilon = 0.00084$ (peak of the local maximum of synchronization), the probability distribution becomes similar to $T = 37\,^{\circ}\mathrm{C}$. For $\epsilon = 0.0014$ the distribution shifts to the right, with neurons spreading farther apart in their probabilities, and then to $\epsilon = 0.008$ the distribution gets very similar to the one in $T = 37\,^{\circ}\mathrm{C}$, but the average is slightly higher. For $T = 40\,^{\circ}\mathrm{C}$ the same strange behavior seen in $T = 38\,^{\circ}\mathrm{C}$ happens, due to the periodicity. We see that some neurons stay permanently in the cluster, and some never stay. This is a result of neurons being periodic (or very close to, cf. Fig 8.1). We again see that behavior at strong coupling is very similar for all temperatures, with $T = 40\,^{\circ}\mathrm{C}$ being the less promiscuous.

Now we take the individual time-averaged probability of each neuron staying in the cluster and average over the network. This resulting probability is similar to the probability of neurons staying in clusters $\overline{p}$, used previously, but is not necessarily the same. We confirm in Fig 8.5 that this is indeed the case: the behavior is very similar to $\mathcal{P}$ (Fig 7.6), but not the same, especially for the less synchronized cases.

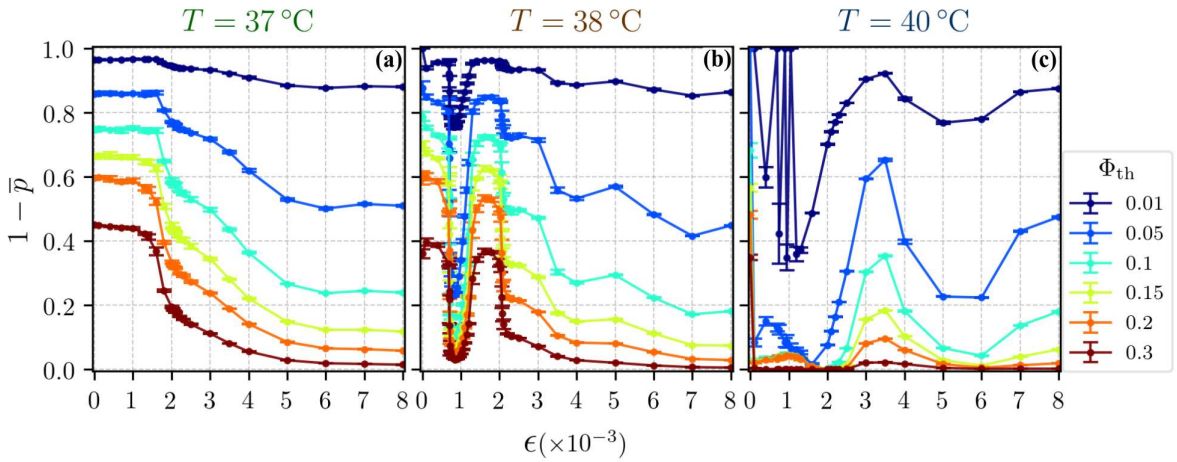

Figure 8.5: **Measure of promiscuity using the average probability of each neuron staying in the biggest cluster**. The average over time and initial conditions is shown for the three temperatures 37 °C, 38 °C, 40 °C as a function of the coupling strength ϵ and for different cluster thresholds Φ_{th}. Result is very similar to the measure $\mathcal{P}$ (cf. Fig 7.6), but not the same, as the probabilities for each neuron are not identical.

There are thus several different ways of measuring the rate of cluster composition change, but the results are similar. This analysis of clusters in the network constitute a powerful tool to characterize the behavior of a network.

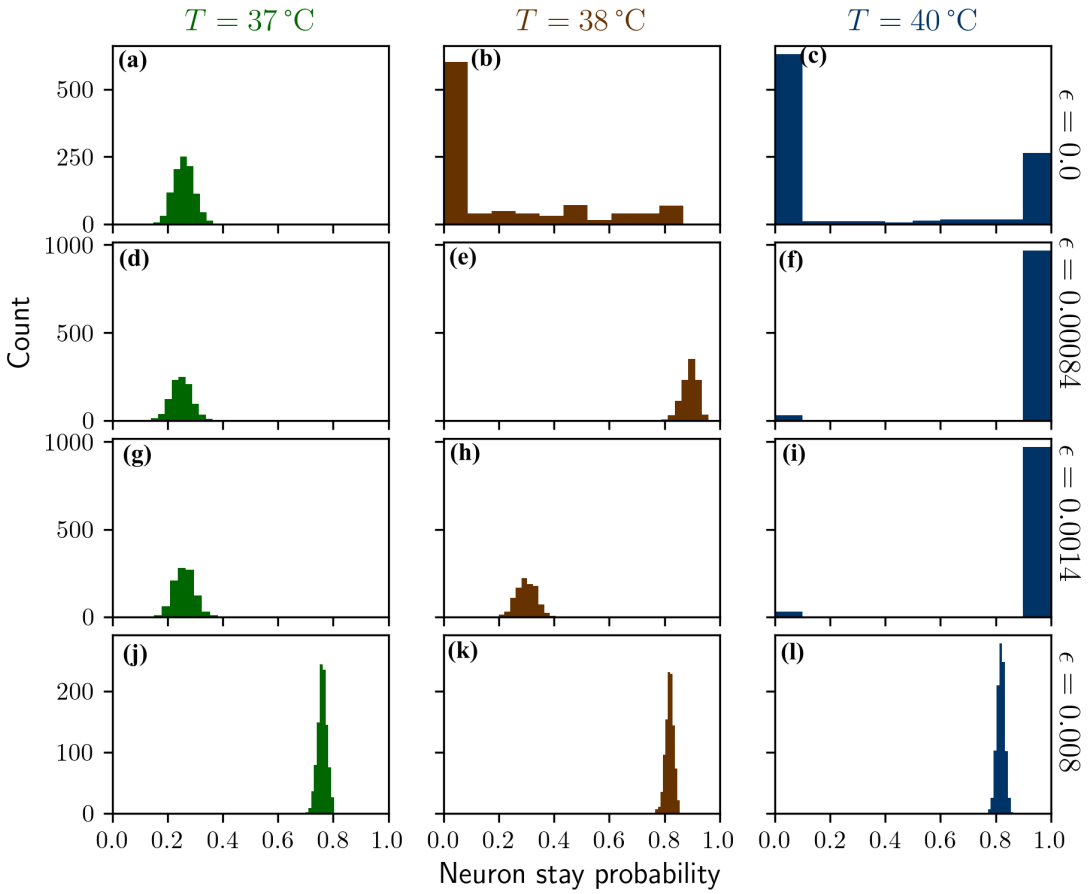

Figure 8.4: **Stay probability for each neuron in the biggest cluster.** For each neuron in the network, we calculate individually the probability that they remain in the BC from each time t_k to the next t_{k+1} and average over time. The figure shows the histogram of these probabilities, showing that neurons are not identical: some are more likely to stay in a cluster than others. Results are shown for the three temperatures 37 °C, 38 °C, 40 °C and coupling strengths $\epsilon = 0.0$, $\epsilon = 0.00084$, $\epsilon = 0.0014$, $\epsilon = 0.008$.

9 METASTABILITY AT DIFFERENT SCALES

On the previous chapters, we have characterized the behaviors of our network, seen that the neural variability reflects in network variabilities which lead to the phenomenon we have called promiscuity. Promiscuity refers to the intermittent phase-locking between neurons. It evidently deals with the phase configurations between neurons, but can also be seen leading to changes in cluster composition. Promiscuity can be regarded as a type of metastability, definition 1c (cf. Section 6.1.3). We adopt this definition of metastability here, which can also be seen as a specific case of the more general definition as variability in activity patterns (cf. Section 6.2).

We thus intend to explore metastability in the network in more detail here, looking at the network's behavior on different levels of the topological scale. These levels can be seen as different specific views of metastability (cf. Section 6.2.1). The macroscopic measure $\sigma(R)$ quantifies the variability in the whole network's degree of phase synchronization, and is very common in the literature; the mesoscopic measure $\mathcal{P}$ quantifies the rate of change in the clusters' composition and, though proposed by us, reflects a common view of metastability affecting cluster formation; the microscopic measure $\sigma(R_{ij})$ quantifies the variability in the pairwise phase synchronization between neurons, and though also proposed by us, reflects a view of metastability as changing the phase relations between neurons.

With this study, we aim at deepening our understanding of metastability in the network, and also at illustrating how quantifiers of metastability for different scales can have different behaviors.

We start with the average degree of phase synchronization, measured via the Kuramoto order parameter (cf. Eq. 5.13) and already shown in Fig 7.1 for the three temperatures ($T = 37\,°C$, $T = 38\,°C$, $T = 40\,°C$) as a function of the coupling strength ϵ. This behavior is already known, and is here to serve as reference for the next measures. The second row contains the standard deviation of the Kuramoto order parameter ($\sigma(R(t))$); the third row contains the standard deviation over the pairwise Kuramoto order parameters, averaged over all pairs ($\sigma(R_{ij})$); the fourth row contains the average probability of neurons staying in clusters ($\mathcal{P}$), already shown before in Fig 7.6. These measures correspond to different levels of analysis on a topological scale: respectively, macro, micro and meso. The macro measure, $\sigma(R)$, peaks at the transitions to and from phase synchronization. Intermittency in transitions has already been observed in very similar networks (Budzinski et al., 2019b) and in Kuramoto oscillator networks (Cabral et al., 2011). In $T = 37\,°C$, only one transition happens, and thus there is only one peak. For $T = 38\,°C$, three transitions happen (from desynchronization to the local maximum, from there to desynchronization and then again to synchronization at strong coupling), and there are three corresponding peaks in the $\sigma(R)$. For $T = 40\,°C$, the first transition occurs for very small ϵ and can be seen only for one point (right after $\epsilon = 0$), the second transition occurs to desynchronization, with a corresponding peak, the third transition is the only exception, without a clear peak.

Therefore, in a macro topological view, the regions of transition are very metastable. In a micro and meso view, however, these regions are on a plateau, and have similar degrees of metastability as in other coupling strengths. This is very clear for $T = 37\,°C$ and $T = 38\,°C$. For $T = 40\,°C$, the plateaus are still seen, but not as clearly. Our focus is on $T = 38\,°C$, so this curious behavior has to be examined in future works.

Focusing on $T = 38\,°C$, we now look at the points around the local maximum of synchronization (also called the first synchronized states, $\epsilon \approx 1 \times 10^{-3}$), and compare to the other points with similar degrees of synchronization, at strong coupling (also called the second

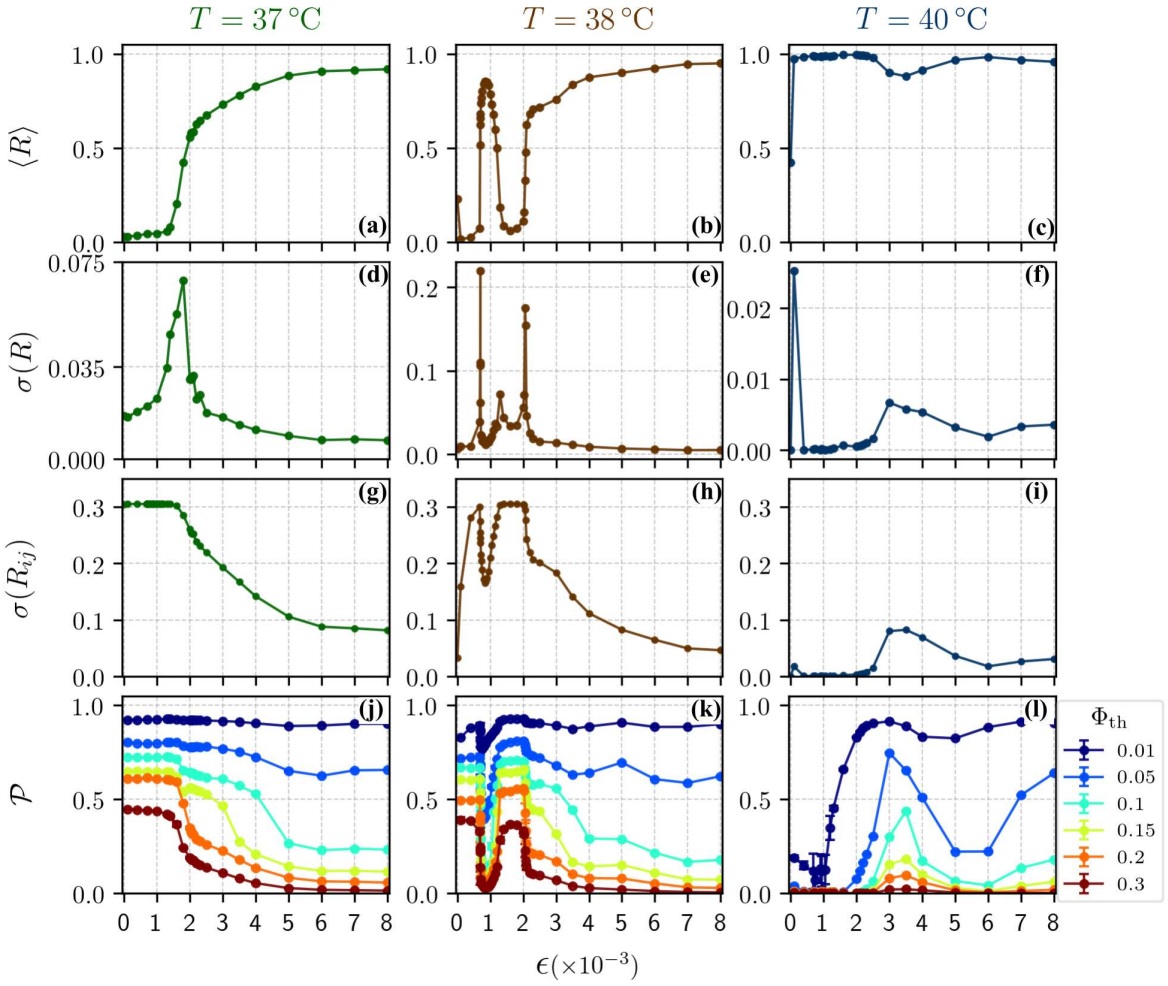

Figure 9.1: **Measures of metastability at different levels of the topological scale.** The first row shows the average degree of phase synchronization, for reference. Then, the second, third and fourth rows depict the macro measure, in the variability of global PS ($\sigma(R)$), the micro measure in the variability of individual PS ($\sigma(R_i j)$) and the meso measure in the rate of change of clusters' composition ($\mathcal{P}$).

PS states, $\epsilon \geq 4 \times 10^{-3}$). For the macro level, metastability is slightly larger in the first than the second, and for the micro level it is considerably larger. For the meso level, the behavior depends on the cluster threshold Φ_{th}: for Φ_{th}, the behavior is the same as in the macro and micro. As the threshold is decreased, the situation reverses and the first PS states are measured as less metastable than the second PS states.

To better understand what is happening, and why these measures differ so much, we plot in Fig 9.2 representative time series of the Kuramoto order parameter ($R(t)$) and the pairwise Kuramoto order parameter ($R_{ij}(t)$ for pair $(i, j) = (1, 2)$). In the local maximum ($\epsilon = 0.00085$) the average degree of network PS varies a bit more than for strong coupling ($\epsilon = 0.008$), in line with the measure of $\sigma(R)$. For the pairwise Kuramoto we see several dips from R_{12} close to 1 in both cases, but with an important distinction: the local maximum has large dips, but the dips are rarer; strong coupling has very frequent dips, but they are generally small. This may be difficult to see in this figure, but is observed in subsequent figures. Taking this to be true now, we see that strong coupling makes neurons have smaller phase differences on average, but these phase differences change more frequently. This is in line with the local maximum having smaller variabilities CV_e and CV_t and smaller drift Δ. It also happens in such a way that the rarer,

larger dips in the local maximum outweigh the more frequent, smaller dips in the strong coupling leading to the larger $\sigma(R_{12})$. Also, with a large clustering threshold, the cluster is more inclusive and neurons inside can have relatively large phase differences. This means the smaller dips in the strong coupling do not affect the cluster composition, but the larger dips in the local maximum do, making clusters in this case change composition more frequently. However, for smaller Φ_{th}, neurons in the cluster have smaller phase differences and the more frequent dips in R_{12} become relevant, so clusters change composition more frequently for strong coupling in this case.

This figure is also interesting as it clearly shows that, for both $\epsilon = 0.00085$ and $\epsilon = 0.008$, the macro level indicates little or no metastability (constant $R(t)$), but the micro level has the opposite (very intermittent $R_{12}(t)$).

All these results are consistent, as the system is the same, but we can clearly see that conclusions can be different depending on the level of analysis. It is therefore important to analyze several levels to understand the system's behavior as a whole.

Analyzing now $\epsilon = 0.000703$ (first transition to PS), we see that for $t \lessapprox 900\,\text{s}$ the average PS degree increases, until finally stabilizing. This means the first transition does not have large intermittency, and the large standard deviation observed is due to the initial (though long in experimental terms ($\approx 900\,\text{s}$)) growth of $R(t)$. The pairwise synchronization in this case does not cease when $R(t)$ stabilizes. For $\epsilon = 0.00206$ (second transition to PS), we see a clear intermittency in $R(t)$, and also extremely frequent and large dips in $R_{12}(t)$. This also happens for $\epsilon = 0.0013$ (not shown), which corresponds to the transition from the local maximum to desynchronization.

We can also see here that the temporal scale is important: for short timescales, one could fail to observe the intermittencies, and conclude no metastability is present (for either the topological macro or micro levels), and only observe the metastability for larger timescales.

To corroborate and better characterize the observations regarding the previous time series, we now analyze their distributions. The first row of Fig 9.3 contains the histograms of $R(t)$, shown in Fig 9.2, with the y-axis in logarithmic scale. For $\epsilon = 0.000703$ there is a distribution around $R = 0.5$, corresponding to the initial growth of $R(t)$, and the peak around $R = 0.7$ corresponds to the final state, which stabilizes around that value, still with a relatively large dispersion. Comparing $\epsilon = 0.00085$ and $\epsilon = 0.008$, we see that the latter has a higher average and a smaller dispersion around it. $\epsilon = 0.00206$ has a large dispersion, consistent with the large intermittency in R. In the second row, the average of the histogram of $R_{ij}(t)$ over all pairs is shown in the solid brown line, with the standard deviation over them shown also above and below. Again, we see the pairs spend a lot of time synchronized, but also a significant amount of time desynchronized for all coupling strengths, and the more synchronized the whole network is the more time the pairs spend synchronized. Specifically comparing $\epsilon = 0.00085$ to $\epsilon = 0.008$, we again see that the former has more large dips (number of bins with $R_{ij} \lessapprox 0.75$ is bigger), but has less small dips.

In Fig 9.2 we see that $R_{12}(t)$ has a laminar period, close to 1, with several dips, escaping this period. To further characterize this intermittency, we calculate the distribution of durations τ in the laminar period, defined as the region above a threshold $R_{ij,\text{th}}$. In Fig 9.4 we show these distributions for thresholds $0.9, 0.95, 0.99, 0.999$ for the same coupling strengths analyzed in the previous two figures. In all cases, we see that higher thresholds lead to shorter laminar periods: they start with higher values at small τ and decay faster for greater τ. Also, the profile of the decay changes: for $R_{ij,\text{th}} = \{0.9, 0.95\}$, the distribution follows a power-law (line in a $\log \times \log$), while for $R_{ij,\text{th}}$ the distribution is more similar to an exponential (line in a $\log \times$linear plot, not shown). Also, we see that $\epsilon = 0.008$ has the maximum laminar period duration for smaller threshold $R_{ij,\text{th}} = 0.9$, but loses to the first maximum ($\epsilon = 0.00085$) for the higher thresholds

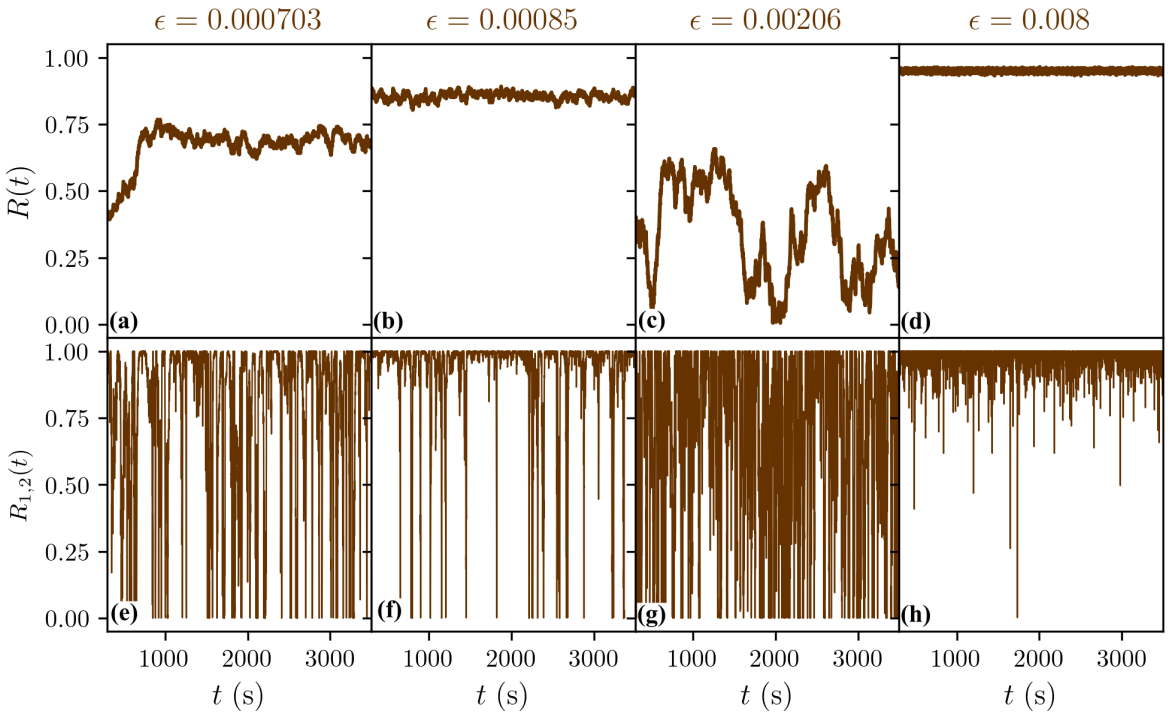

Figure 9.2: **Representative time series for network and pairwise synchronizations in $T = 38\,°\mathrm{C}$.** The first row contains the time series of the network's degree of phase synchronization $R(t)$, and the second row contains the degree of phase synchronization for the neuron pair $(1, 2)$. Simulations in these specific cases were run from $t = 300\,\mathrm{s}$ to $t = 3500\,\mathrm{s}$. This figure illustrates how different scales and levels of analysis can lead to different conclusions regarding metastability.

$R_{ij,\mathrm{th}} = 0.95, 0.99, 0.999$. This again shows that the former has frequent small dips, while the latter has rare big dips in $R_{ij}(t)$.

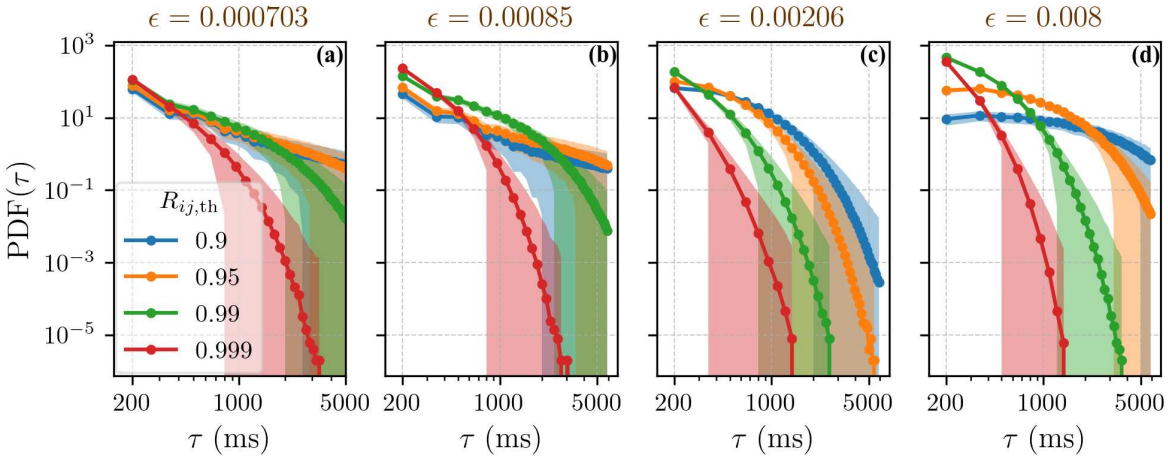

Figure 9.4: **Distributions of duration in the laminar period of R_{ij}.** For each pair (i, j), the laminar period is defined as the region above a threshold $R_{ij,\mathrm{th}}$. Results shown are an average of the histogram of the laminar period duration τ taken over all pairs, with the standard deviation in the filled area for the four thresholds $0.9, 0.95, 0.99, 0.999$ (blue, orange, green, red lines, respectively) and for coupling strengths $\epsilon = 0.000703$ (first transition to phase synchronization), $\epsilon = 0.00085$ (local maximum), $\epsilon = 0.00206$ (second transition to PS) and $\epsilon = 0.008$ (strong coupling). Both axis are in logarithmic scale. Higher thresholds are seen to lead to shorter laminar periods, and we again see that strong coupling has frequent, small dips, while the local maximum has rare, large dips.

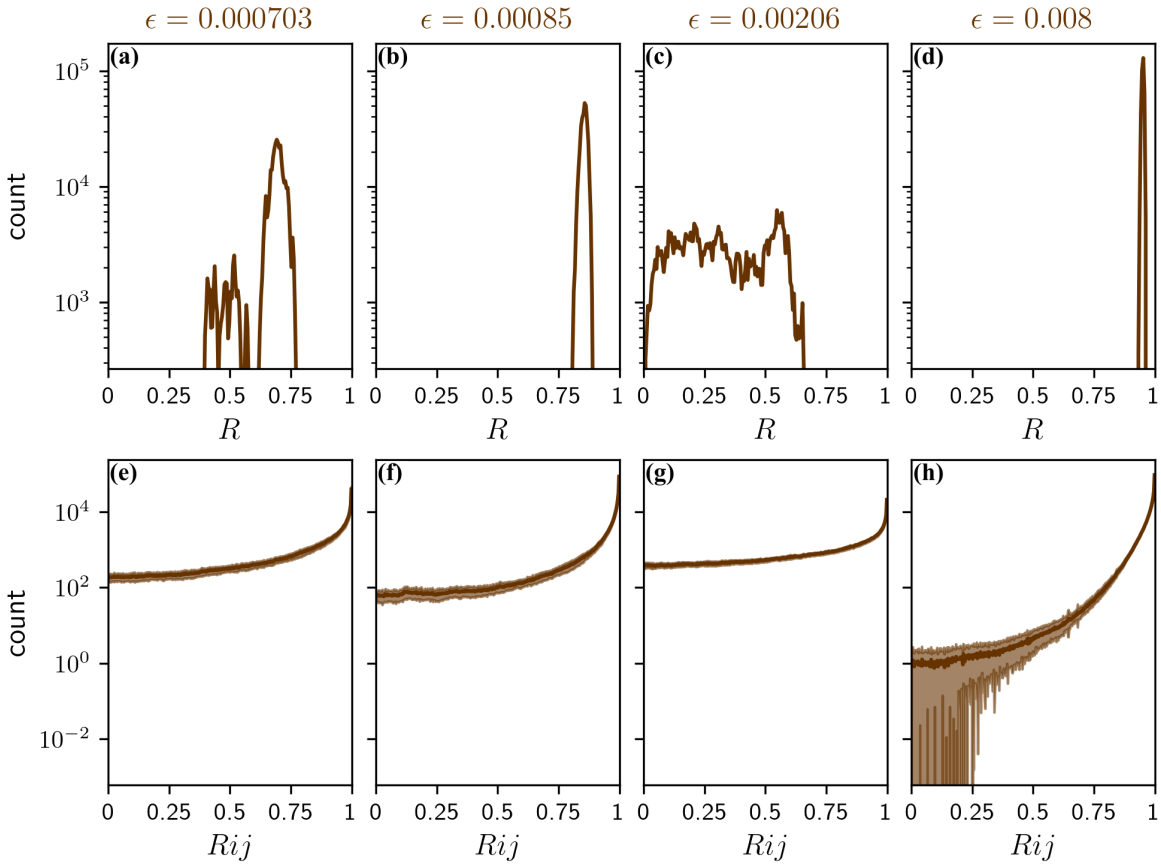

Figure 9.3: **Distributions of $R(t)$ and $R_{ij}(t)$ for $T = 38\,^{\circ}\mathrm{C}$.** First row depicts the histogram of $R(t)$ and the second depicts the histogram of $R_{ij}(t)$ average over all pairs, with the standard deviation shown in the filled areas. These are performed for $\epsilon = 0.000703$ (first transition to phase synchronization), $\epsilon = 0.00085$ (local maximum), $\epsilon = 0.00206$ (second transition to PS) and $\epsilon = 0.008$ (strong coupling). This figure corroborates the analysis in Fig 9.2.

Part III

Summary, Conclusions and Future Perspectives

This dissertation has aimed to study the phase synchronization properties of a simple network of bursting neurons coupled with a random topology, and use it as an example to illustrate points regarding the study of metastability. This network has several simplifications compared to real biological networks, such as identical neurons, few connections, and no noise. This is important here, as we can isolate important behaviors of the network to specific origins. In this case, we see that promiscuity, which we relate to metastability, arises from a dynamical heterogeneity in the model, not from other sources like noise or differing parameters. This heterogeneity is captured by the firing variabilities that we measure.

First, by changing the neurons' temperature, we were able to do the study for three different uncoupled bursting modes: chaotic bursts and periodic bursts (with two and one inter-burst intervals IBIs). We have seen that each mode leads to different transitions to phase synchronization (PS) due to an increase in the coupling strength: a monotonic transition, common in the literature, and two nonmonotonic transitions, with a region of high PS for weak coupling, a subsequent desynchronization and later resynchronization.

We have also studied two types of variability in the neuronal firing: average over neurons of their individual dispersion of IBIs in time (temporal variability) and average over time of the dispersion of IBIs in the network for each bursting event (ensemble variability). The two measures quantify different behaviors, but in all cases they have the same value, likely due to the system being ergodic.

For relatively weak coupling, there is a strong correlation between the degree of PS and the variabilities, as we have shown that in this region the neurons' dynamics is largely influenced by their uncoupled dynamics: uncoupled chaotic neurons have higher variability, which remains high when they are uncoupled, and can be interpreted as hindering the PS of the network; uncoupled periodic neurons have very low variability, which increases due to coupling (they become chaotic) but not as much, so PS is not as hindered and the network synchronizes to a higher degree. Though very tentative, we remark that the relation between variability and phase synchronization in this case was only shown to be correlative, not causal. Other results, even for other models, have established the causal relation for some cases, but are not shown here. The influence of the uncoupled dynamics was further seen in the IBI bifurcation diagram and in the return maps of the IBIs. For stronger coupling, we have seen that the dynamics becomes similar in all cases, as the impact of the coupling current increases, the neurons become more chaotic (more irregular) and the phase synchronization properties become more similar. In all cases, the ensemble variability has very similar values to the temporal variability. This seems to be a reflection of the neurons being identical: in other results, not shown here, where neurons were made non-identical, variabilities are different between themselves.

The ensemble variability predicts a behavior we have called promiscuity: the intermittent changes in the neurons' phase differences. By measuring the average drift of burst times, we confirmed this behavior. We have further characterized it through an analysis of clustering of the neurons' phases. This provided further details about the PS of the networks, and also allowed us to observe promiscuity in the changes of the clusters' composition in time. With this, we have seen that strong coupling is able to bring neurons' phases close, but unable to maintain their phase relations fixed. This is not the standard behavior observed for networks, where usually stronger coupling leads to phase locking (Cabral et al., 2011).

We have also discussed metastability in neuroscience, a highly studied phenomenon due to its putative importance to brain functioning. We provided a mini-review of the different definitions in the literature, and discussed them, in a first step to unifying the term's definition. Possible mechanisms leading to metastable behavior were also reviewed and categorized. We also exemplified how the specific definitions or quantifiers of metastability can depend on the

scales of activity being studied or analyzed. We illustrated this in our promiscuous network, where we studied metastability, for a specific definition, on different scales. Using the insights gained from the study of promiscuity, which can be regarded as a type of metastable behavior, we explored how quantifiers for metastability can differ on the different scales.

With these studies, we can also point out that metastability in this system seems to occur due to a dynamical (not parametrical) heterogeneity between neurons, captured by the ensemble and temporal variabilities. The dynamical heterogeneity here arises from the neuron's complex dynamics in phase-space and also in part due to their differing in-degrees (though it can be observed in regular networks). This is a counter-example of an idea in the literature that metastability arises from broken symmetry in the form of unidentical oscillators (Tognoli and Kelso, 2014; Bressler and Kelso, 2016).

With these studies, we therefore managed to characterize in detail the behavior of the network. We also hope to have provided a first step toward unifying the definitions of metastability in the literature, and identifying the mechanisms in the brain generating the observed metastable behavior. For the future, we intend on suggesting a general encompassing definition of metastability and, with this, on exploring the consequences of the different mechanisms for metastability to a system's behavior, and how they would reflect in experimental data. We can then look at experimental data and simulated data from biologically realistic models to study their metastable behavior at different scales. These works, stemming from this dissertation, can potentially have a significant positive impact in the field of neuroscience.

REFERENCES

Abbott, L. F. and Nelson, S. B. (2000). Synaptic plasticity: taming the beast. *Nature Neuroscience*, 3(11):1178–1183.

Afraimovich, V., Tristan, I., Huerta, R., and Rabinovich, M. I. (2008). Winnerless competition principle and prediction of the transient dynamics in a Lotka-Volterra model. *Chaos*, 18(4):043103.

Aguilera, M., Bedia, M. G., and Barandiaran, X. E. (2016). Extended neural metastability in an embodied model of sensorimotor coupling. *Frontiers in Systems Neuroscience*, 10(SEP):76.

Alderson, T. H., Bokde, A. L., Kelso, J. A., Maguire, L., and Coyle, D. (2020). Metastable neural dynamics underlies cognitive performance across multiple behavioural paradigms. *Human Brain Mapping*, 41(12):3212–3234.

Alligood, K. T., Sauer, T. D., and Yorke, J. A. (1997). *Chaos*. Textbooks in Mathematical Sciences. Springer Berlin Heidelberg, Berlin, Heidelberg.

Ansmann, G., Lehnertz, K., and Feudel, U. (2016). Self-induced switchings between multiple space-time patterns on complex networks of excitable units. *Physical Review X*, 6(1):011030.

Arenas, A., Díaz-Guilera, A., Kurths, J., Moreno, Y., and Zhou, C. (2008). Synchronization in complex networks. *Physics Reports*, 469(3):93–153.

Aydore, S., Pantazis, D., and Leahy, R. M. (2013). A note on the phase locking value and its properties. *Neuroimage*, 74:231–244.

Barabasi, A. L. and Albert, R. (1999). Emergence of scaling in random networks. *Science*, 286(5439):509–512.

Barreira, L. (2017). *Lyapunov Exponents*. Springer International Publishing, Cham.

Barttfeld, P., Uhrig, L., Sitt, J. D., Sigman, M., and Jarraya, B. (2015). Correction Correction for "Signature of consciousness in the dynamics of resting-state brain activity," by A B E F C G D. *Proc Natl Acad Sci*, 3:887–892.

Bassett, D. S., Wymbs, N. F., Porter, M. A., Mucha, P. J., Carlson, J. M., and Grafton, S. T. (2011). Dynamic reconfiguration of human brain networks during learning. *Proceedings of the National Academy of Sciences of the United States of America*, 108(18):7641–7646.

Bassett, D. S., Yang, M., Wymbs, N. F., and Grafton, S. T. (2015). Learning-induced autonomy of sensorimotor systems. *Nature Neuroscience*, 18(5):744–751.

beim Graben, P., Jimenez-Marin, A., Diez, I., Cortes, J. M., Desroches, M., and Rodrigues, S. (2019). Metastable Resting State Brain Dynamics. *Frontiers in Computational Neuroscience*, 13:62.

Berry, M. J. and Tkačik, G. (2020). Clustering of Neural Activity: A Design Principle for Population Codes. *Frontiers in Computational Neuroscience*, 14(13):20.

Betzel, R. F. and Bassett, D. S. (2017). Multi-scale brain networks. *NeuroImage*, 160:73–83.

Bezanson, J., Edelman, A., Karpinski, S., and Shah, V. B. (2017). Julia: A fresh approach to numerical computing. *{SIAM} Review*, 59(1):65–98.

Bhowmik, D. and Shanahan, M. (2013). Metastability and Inter-Band Frequency Modulation in Networks of Oscillating Spiking Neuron Populations. *PLoS ONE*, 8(4):e62234.

Boaretto, B. R., Budzinski, R. C., Prado, T. L., Kurths, J., and Lopes, S. R. (2018a). Suppression of anomalous synchronization and nonstationary behavior of neural network under small-world topology. *Physica A: Statistical Mechanics and its Applications*, 497:126–138.

Boaretto, B. R. R., Budzinski, R. C., Prado, T. L., Kurths, J., and Lopes, S. R. (2018b). Neuron dynamics variability and anomalous phase synchronization of neural networks. *Chaos*, 28(10):106304.

Boaretto, B. R. R., Budzinski, R. C., Prado, T. L., Kurths, J., and Lopes, S. R. (2018c). Suppression of anomalous synchronization and nonstationary behavior of neural network under small-world topology. *Physica A: Statistical Mechanics and its Applications*, 497:126–138.

Boaretto, B. R. R., Budzinski, R. C., Prado, T. L., Kurths, J., and Lopes, S. R. (2019). Protocol for suppression of phase synchronization in Hodgkin-Huxley-type networks. *Physica A: Statistical Mechanics and its Applications*, 528:121388.

Boccaletti, S., Kurths, J., Osipov, G., Valladares, D. L., and Zhou, C. S. (2002). The synchronization of chaotic systems. *Physics Reports*, 366(1-2):1–101.

Braun, H. A., Huber, M. T., Dewald, M., Schafer, K., and Voigt, K. (1998). Computer simulations of neuronal signal transduction: the role of nonlinear dynamics and noise. *International Journal of Bifurcation and Chaos*, 8(05):881–889.

Braun, H. A., Schwabedal, J., Dewald, M., Finke, C., Postnova, S., Huber, M. T., Wollweber, B., Schneider, H., Hirsch, M. C., Voigt, K., Feudel, U., and Moss, F. (2011). Noise-induced precursors of tonic-to-bursting transitions in hypothalamic neurons and in a conductance-based model. *Chaos*, 21(4):47509.

Braun, W., Eckhardt, B., Braun, H. A., and Huber, M. (2000). Phase-space structure of a thermoreceptor. *Physical review. E, Statistical physics, plasmas, fluids, and related interdisciplinary topics*, 62(5 Pt A):6352–6360.

Bressler, S. L. and Kelso, J. A. S. (2016). Coordination dynamics in cognitive neuroscience. *Frontiers in Neuroscience*, 10:397.

Brown, A. G. (1991). *Nerve cells and nervous systems*. Springer London, London.

Budzinski, R. C., Boaretto, B. R. R., Prado, T. L., and Lopes, S. R. (2017). Detection of nonstationary transition to synchronized states of a neural network using recurrence analyses. *Physical review. E*, 96(1-1):12320.

Budzinski, R. C., Boaretto, B. R. R., Prado, T. L., and Lopes, S. R. (2019a). Phase synchronization and intermittent behavior in healthy and Alzheimer-affected human-brain-based neural network. *Physical review. E*, 99(2-1):22402.

Budzinski, R. C., Boaretto, B. R. R., Prado, T. L., and Lopes, S. R. (2019b). Synchronization domains in two coupled neural networks. *Communications in Nonlinear Science and Numerical Simulation*, 75:140–151.

Budzinski, R. C., Boaretto, B. R. R., Prado, T. L., and Lopes, S. R. (2019c). Temperature dependence of phase and spike synchronization of neural networks. *Chaos, Solitons & Fractals*, 123:35–42.

Budzinski, R. C., Rossi, K. L., Boaretto, B. R. R., Prado, T. L., and Lopes, S. R. (2020). Synchronization malleability in neural networks under a distance-dependent coupling. *{arXiv}:2006.03643 [physics, q-bio]*.

Bullmore, E. and Sporns, O. (2009). Complex brain networks: Graph theoretical analysis of structural and functional systems. *Nature Reviews. Neuroscience*, 10(3):186–198.

Buschman, T. J. and Miller, E. K. (2007). Top-down versus bottom-up control of attention in the prefrontal and posterior parietal cortices. *Science*, 315(5820):1860–1862.

Butcher, J. C. (2016). *Numerical methods for ordinary differential equations*. John Wiley & Sons, Ltd, Chichester, {UK}.

Butera, R. J., Rinzel, J., and Smith, J. C. (1999). Models of respiratory rhythm generation in the pre-Bötzinger complex. I. Bursting pacemaker neurons. *Journal of Neurophysiology*, 82(1):382–397.

Buzsáki, G. (2010). Neural Syntax: Cell Assemblies, Synapsembles, and Readers.

Buzsáki, G. and Draguhn, A. (2004). Neuronal oscillations in cortical networks. *Science*, 304(5679):1926–1929.

Cabral, J., Hugues, E., Sporns, O., and Deco, G. (2011). Role of local network oscillations in resting-state functional connectivity. *Neuroimage*, 57(1):130–139.

Cao, Y. (2004). A note about Milnor attractor and riddled basin. *Chaos, Solitons and Fractals*, 19(4):759–764.

Cavanagh, J. F., Cohen, M. X., and Allen, J. J. B. (2009). Prelude to and resolution of an error: {EEG} phase synchrony reveals cognitive control dynamics during action monitoring. *The Journal of Neuroscience*, 29(1):98–105.

Cavanna, F., Vilas, M. G., Palmucci, M., and Tagliazucchi, E. (2018). Dynamic functional connectivity and brain metastability during altered states of consciousness. *NeuroImage*, 180(Pt B):383–395.

Chen, G., Wang, X., and Li, X. (2014). *Fundamentals of complex networks: models, structures and dynamics*. John Wiley & Sons Singapore Pte. Ltd, Singapore.

Chouard, T. and Gray, N. (2010). Glia. *Nature*, 468(7321):213.

Colgin, L. L., Denninger, T., Fyhn, M., Hafting, T., Bonnevie, T., Jensen, O., Moser, M.-B., and Moser, E. I. (2009). Frequency of gamma oscillations routes flow of information in the hippocampus. *Nature*, 462(7271):353–357.

Coombes, S. and Bressloff, P. C. (2005). *Bursting: The genesis of rhythm in the nervous system*. World Scientific Publishing Co.

Csicsvari, J., Hirase, H., Czurko, A., and Buzsáki, G. (1998). Reliability and state dependence of pyramidal cell-interneuron synapses in the hippocampus: an ensemble approach in the behaving rat. *Neuron*, 21(1):179–189.

Dayan, P. and Abbott, L. F. (2005). *Theoretical Neuroscience: Computational And Mathematical Modeling Of Neural Systems (computational Neuroscience Series)*. The Mit Press, 1st editio edition.

De Vico Fallani, F., Richiardi, J., Chavez, M., and Achard, S. (2014). Graph analysis of functional brain networks: practical issues in translational neuroscience. *Philosophical Transactions of the Royal Society of London. Series B, Biological Sciences*, 369(1653).

Deco, G., Kringelbach, M. L., Jirsa, V. K., and Ritter, P. (2017). The dynamics of resting fluctuations in the brain: Metastability and its dynamical cortical core. *Scientific Reports*, 7(1):3095.

Dehaene, S., Charles, L., King, J.-R., and Marti, S. (2014). Toward a computational theory of conscious processing. *Current Opinion in Neurobiology*, 25:76–84.

Del Negro, C. A., Hsiao, C. F., Chandler, S. H., and Garfinkel, A. (1998). Evidence for a novel bursting mechanism in rodent trigeminal neurons. *Biophysical Journal*, 75(1):174–182.

Destexhe, A., Mainen, Z. F., and Sejnowski, T. J. (1994). An efficient method for computing synaptic conductances based on a kinetic model of receptor binding. *Neural Computation*, 6(1):14–18.

Deweese, M. R. and Zador, A. M. (2004). Shared and private variability in the auditory cortex. *Journal of Neurophysiology*, 92(3):1840–1855.

Ding, S. L., Royall, J. J., Sunkin, S. M., Ng, L., Facer, B. A., Lesnar, P., Guillozet-Bongaarts, A., McMurray, B., Szafer, A., Dolbeare, T. A., Stevens, A., Tirrell, L., Benner, T., Caldejon, S., Dalley, R. A., Dee, N., Lau, C., Nyhus, J., Reding, M., Riley, Z. L., Sandman, D., Shen, E., van der Kouwe, A., Varjabedian, A., Write, M., Zollei, L., Dang, C., Knowles, J. A., Koch, C., Phillips, J. W., Sestan, N., Wohnoutka, P., Zielke, H. R., Hohmann, J. G., Jones, A. R., Bernard, A., Hawrylycz, M. J., Hof, P. R., Fischl, B., and Lein, E. S. (2016). Comprehensive cellular-resolution atlas of the adult human brain. *Journal of Comparative Neurology*, 524(16):3127–3481.

Dinstein, I., Pierce, K., Eyler, L., Solso, S., Malach, R., Behrmann, M., and Courchesne, E. (2011). Disrupted neural synchronization in toddlers with autism. *Neuron*, 70(6):1218–1225.

Dombeck, D. A., Graziano, M. S., and Tank, D. W. (2009). Functional clustering of neurons in motor cortex determined by cellular resolution imaging in awake behaving mice. *Journal of Neuroscience*, 29(44):13751–13760.

Du, Y., Lu, Q., and Wang, R. (2010). Using interspike intervals to quantify noise effects on spike trains in temperature encoding neurons. *Cognitive neurodynamics*, 4(3):199–206.

Engel, A. K., Fries, P., König, P., Brecht, M., and Singer, W. (1999). Temporal binding, binocular rivalry, and consciousness. *Consciousness and Cognition*, 8(2):128–151.

Engel, A. K., Fries, P., and Singer, W. (2001). Dynamic predictions: oscillations and synchrony in top-down processing. *Nature Reviews. Neuroscience*, 2(10):704–716.

Érdi, P., Esposito, A., Marinaro, M., and Scarpetta, S., editors (2004). *Computational Neuroscience: Cortical Dynamics*, volume 3146 of *Lecture Notes in Computer Science*. Springer Berlin Heidelberg, Berlin, Heidelberg.

Erdos, P. and Rényi, A. (2011). On the evolution of random graphs. *The Structure and Dynamics of Networks*, 9781400841:38–82.

Fell, J. and Axmacher, N. (2011). The role of phase synchronization in memory processes. *Nature Reviews. Neuroscience*, 12(2):105–118.

Feudel, U., Neiman, A., Pei, X., Wojtenek, W., Braun, H., Huber, M., and Moss, F. (2000). Homoclinic bifurcation in a Hodgkin-Huxley model of thermally sensitive neurons. *Chaos*, 10(1):231–239.

Fields, R. D., Araque, A., Johansen-Berg, H., Lim, S.-S., Lynch, G., Nave, K.-A., Nedergaard, M., Perez, R., Sejnowski, T., and Wake, H. (2014). Glial biology in learning and cognition. *The Neuroscientist*, 20(5):426–431.

Fields, R. D. and Stevens-Graham, B. (2002). New insights into neuron-glia communication. *Science*, 298(5593):556–562.

Fingelkurts, A. A. and Fingelkurts, A. A. (2001). Operational architectonics of the human brain biopotential field: Towards solving the mind-brain problem.

Fingelkurts, A. A. and Fingelkurts, A. A. (2004). Making complexity simpler: Multivariability and metastability in the brain.

Finke, C., Freund, J. A., Rosa, E., Braun, H. A., and Feudel, U. (2010). On the role of subthreshold currents in the Huber-Braun cold receptor model. *Chaos*, 20(4):45107.

Finke, C., Freund, J. A., Rosa, E., Bryant, P. H., Braun, H. A., and Feudel, U. (2011). Temperature-dependent stochastic dynamics of the Huber-Braun neuron model. *Chaos*, 21(4):47510.

Fontenele, A. J., De Vasconcelos, N. A., Feliciano, T., Aguiar, L. A., Soares-Cunha, C., Coimbra, B., Dalla Porta, L., Ribeiro, S., Rodrigues, A. J., Sousa, N., Carelli, P. V., and Copelli, M. (2019). Criticality between Cortical States. *Physical Review Letters*, 122(20):208101.

Fornito, A., Zalesky, A., and Breakspear, M. (2013). Graph analysis of the human connectome: promise, progress, and pitfalls. *Neuroimage*, 80:426–444.

Fox, D. M., Rotstein, H. G., and Nadim, F. (2015). Bursting in neurons and small networks. In Jaeger, D. and Jung, R., editors, *Encyclopedia of computational neuroscience*, pages 455–469. Springer New York, New York, {NY}.

Fries, P. (2005). A mechanism for cognitive dynamics: neuronal communication through neuronal coherence. *Trends in Cognitive Sciences*, 9(10):474–480.

Fries, P. (2015). Rhythms for Cognition: Communication through Coherence. *Neuron*, 88(1):220–235.

Fries, P., Nikolić, D., and Singer, W. (2007). The gamma cycle. *Trends in Neurosciences*, 30(7):309–316.

Friston, K. J. (1997). Transients, metastability, and neuronal dynamics. *NeuroImage*, 5(2):164–171.

Friston, K. J. (2000). The labile brain. I. Neuronal transients and nonlinear coupling. *Philosophical Transactions of the Royal Society of London. Series B, Biological Sciences*, 355(1394):215–236.

Gaillard, R., Dehaene, S., Adam, C., Clémenceau, S., Hasboun, D., Baulac, M., Cohen, L., and Naccache, L. (2009). Converging intracranial markers of conscious access. *{PLoS} Biology*, 7(3):e61.

Galvan, A. and Wichmann, T. (2008). Pathophysiology of parkinsonism. *Clinical Neurophysiology*, 119(7):1459–1474.

Glaze, T. A., Lewis, S., and Bahar, S. (2016). Chimera states in a Hodgkin-Huxley model of thermally sensitive neurons. *Chaos*, 26(8):083119.

Glendinning, P. (1994). *Stability, Instability And Chaos: An Introduction To The Theory Of Nonlinear Differential Equations (cambridge Texts In Applied Mathematics)*. Cambridge University Press, Cambridge [England], 1 edition.

Gonzalez, W. G., Zhang, H., Harutyunyan, A., and Lois, C. (2019). Persistence of neuronal representations through time and damage in the hippocampus. *Science*, 365(6455):821–825.

Hindmarsh, A. C., Brown, P. N., Grant, K. E., Lee, S. L., Serban, R., Shumaker, D. E., and Woodward, C. S. (2005). {SUNDIALS}: Suite of nonlinear and differential/algebraic equation solvers. *{ACM} Transactions on Mathematical Software ({TOMS})*, 31(3):363–396.

Hodgkin, A. L. (1948). The local electric changes associated with repetitive action in a non-medullated axon. *The Journal of Physiology*, 107(2):165–181.

Hodgkin, A. L. and Huxley, A. F. (1952). A quantitative description of membrane current and itsc application to conduction and excitation in nerve. *The Journal of Physiology.*, 117:500–544.

Hudson, A. E. (2017). Metastability of neuronal dynamics during general anesthesia: Time for a change in our assumptions? *Frontiers in Neural Circuits*, 11:58.

Hunter, J. D. (2007). Matplotlib: A {2D} Graphics Environment. *Computing in science & engineering*, 9(3):90–95.

Ivanchenko, M. V., Osipov, G. V., Shalfeev, V. D., and Kurths, J. (2004). Phase synchronization in ensembles of bursting oscillators. *Physical Review Letters*, 93(13):134101.

Izhikevich, E. (2006). Bursting. *Scholarpedia*, 1(3):1300.

Izhikevich, E. M. (2007). *Dynamical systems in neuroscience*. {MIT} press.

Johnston, D. . (1995). *Foundations Of Cellular Neurophysiology*. A Bradford book. Mit Press, Cambridge, Mass, 1 edition.

Kandel, E. R., Schwartz, J. H., Jessell, T. M., Siegelbaum, S. A., Hudspeth, A. J., and Others (2000). *Principles of neural science*, volume 4. {McGraw}-hill New York.

Kaneko, K. and Tsuda, I. (2003). Chaotic itinerancy. *Chaos*, 13:926.

Kara, P., Reinagel, P., and Reid, R. C. (2000). Low response variability in simultaneously recorded retinal, thalamic, and cortical neurons. *Neuron*, 27(3):635–646.

Kelso, J. A. and Tognoli, E. (2007). Toward a complementary neuroscience: Metastable coordination dynamics of the brain. *Understanding Complex Systems*, 2007:39–59.

Klinshov, V. V., Teramae, J., Nekorkin, V. I., and Fukai, T. (2014). Dense Neuron Clustering Explains Connectivity Statistics in Cortical Microcircuits. *PLoS ONE*, 9(4):94292.

Koch, C. and Segev, I. (2000). The role of single neurons in information processing. *Nature Neuroscience*, 3 Suppl:1171–1177.

Kraut, S. and Feudel, U. (2002). Multistability, noise, and attractor hopping: The crucial role of chaotic saddles. *Physical Review E - Statistical Physics, Plasmas, Fluids, and Related Interdisciplinary Topics*, 66(1):015207.

Kringelbach, M. L., McIntosh, A. R., Ritter, P., Jirsa, V. K., and Deco, G. (2015). The Rediscovery of Slowness: Exploring the Timing of Cognition.

Kuramoto, Y. (1984). *Chemical Oscillations, Waves, and Turbulence*, volume 19 of *Springer Series in Synergetics*. Springer Berlin Heidelberg, Berlin, Heidelberg.

La Camera, G., Fontanini, A., and Mazzucato, L. (2019). Cortical computations via metastable activity. *Current Opinion in Neurobiology*, 58:37–45.

Lachaux, J. P., Rodriguez, E., Martinerie, J., and Varela, F. J. (1999). Measuring phase synchrony in brain signals. *Human Brain Mapping*, 8(4):194–208.

Latora, V. and Marchiori, M. (2001). Efficient behavior of small-world networks. *Physical Review Letters*, 87(19):198701.

Le Van Quyen, M. (2003). Disentangling the dynamic core: A research program for a neurodynamics at the large scale.

Lee, W. H. and Frangou, S. (2017). Linking functional connectivity and dynamic properties of resting-state networks. *Scientific Reports*, 7(1):16610.

Lisman, J. E. (1997). Bursts as a unit of neural information: making unreliable synapses reliable. *Trends in Neurosciences*, 20(1):38–43.

Lowet, E., Roberts, M. J., Bonizzi, P., Karel, J., and De Weerd, P. (2016). Quantifying Neural Oscillatory Synchronization: A Comparison between Spectral Coherence and Phase-Locking Value Approaches. *Plos One*, 11(1):e0146443.

Manik, D., Rohden, M., Ronellenfitsch, H., Zhang, X., Hallerberg, S., Witthaut, D., and Timme, M. (2017). Network susceptibilities: Theory and applications. *Physical Review E*, 95(1):012319.

Marconi, E., Nieus, T., Maccione, A., Valente, P., Simi, A., Messa, M., Dante, S., Baldelli, P., Berdondini, L., and Benfenati, F. (2012). Emergent functional properties of neuronal networks with controlled topology. *Plos One*, 7(4):e34648.

McCormick, D. A. and Pape, H. C. (1990). Properties of a hyperpolarization-activated cation current and its role in rhythmic oscillation in thalamic relay neurones. *The Journal of Physiology*, 431:291–318.

Medeiros, E. S., Medrano-T, R. O., Caldas, I. L., Tél, T., and Feudel, U. (2019). State-dependent vulnerability of synchronization. *Physical Review E*, 100(5):052201.

Melloni, L., Molina, C., Pena, M., Torres, D., Singer, W., and Rodriguez, E. (2007). Synchronization of neural activity across cortical areas correlates with conscious perception. *The Journal of Neuroscience*, 27(11):2858–2865.

Milnor, J. (1985). On the concept of attractor. *Communications in Mathematical Physics*, 99(2):177–195.

Milnor, J. (2006). Attractor. *Scholarpedia*, 1(11):1815.

Mormann, F., Lehnertz, K., David, P., and E. Elger, C. (2000). Mean phase coherence as a measure for phase synchronization and its application to the {EEG} of epilepsy patients. *Physica D: Nonlinear Phenomena*, 144(3-4):358–369.

Movshon, J. A. (2000). Reliability of neuronal responses. *Neuron*, 27(3):412–414.

Nawrot, M. P. (2010). Analysis and Interpretation of Interval and Count Variability in Neural Spike Trains. In Grün, S. and Rotter, S., editors, *Analysis of Parallel Spike Trains*, pages 37–58. Springer {US}, Boston, {MA}.

Nawrot, M. P., Boucsein, C., Rodriguez Molina, V., Riehle, A., Aertsen, A., and Rotter, S. (2008). Measurement of variability dynamics in cortical spike trains. *Journal of Neuroscience Methods*, 169(2):374–390.

Newman, M. E. and Watts, D. J. (1999). Scaling and percolation in the small-world network model. *Physical review. E, Statistical physics, plasmas, fluids, and related interdisciplinary topics*, 60(6 Pt B):7332–7342.

Nowak, L. G., Azouz, R., Sanchez-Vives, M. V., Gray, C. M., and McCormick, D. A. (2003). Electrophysiological classes of cat primary visual cortical neurons in vivo as revealed by quantitative analyses. *Journal of Neurophysiology*, 89(3):1541–1566.

O'Donnell, C. and van Rossum, M. C. W. (2014). Systematic analysis of the contributions of stochastic voltage gated channels to neuronal noise. *Frontiers in Computational Neuroscience*, 8:105.

Oliphant, T. E. (2006). *A guide to {NumPy}*, volume 1. Trelgol Publishing {USA}.

Ott, E. (2006). Crises. *Scholarpedia*, 1(10):1700.

Ott, E. and Edward, O. (2002). *Chaos in Dynamical Systems*. Cambridge University Press, Cambridge, U.K, 2nd editio edition.

Perin, R., Berger, T. K., and Markram, H. (2011). A synaptic organizing principle for cortical neuronal groups. *Proceedings of the National Academy of Sciences of the United States of America*, 108(13):5419–5424.

Perin, R., Telefont, M., and Markram, H. (2013). Computing the size and number of neuronal clusters in local circuits. *Frontiers in Neuroanatomy*, (JAN).

Pikovsky, A. . (2016). *Lyapunov Exponents: A Tool to Explore Complex Dynamics*. Cambridge University Press,, Cambridge.

Pikovsky, A., Rosenblum, M., Kurths, J., and Hilborn, R. C. (2002). synchronization: A universal concept in nonlinear science. *American journal of physics*, 70(6):655.

Ponce-Alvarez, A., Deco, G., Hagmann, P., Romani, G. L., Mantini, D., and Corbetta, M. (2015). Resting-State Temporal Synchronization Networks Emerge from Connectivity Topology and Heterogeneity. *PLoS Computational Biology*, 11(2):e1004100.

Postnova, S., Voigt, K., and Braun, H. A. (2007a). Neural synchronization at tonic-to-bursting transitions. *Journal of Biological Physics*, 33(2):129–143.

Postnova, S., Wollweber, B., Voigt, K., and Braun, H. (2007b). Impulse pattern in bi-directionally coupled model neurons of different dynamics. *Bio Systems*, 89(1-3):135–142.

Prado, T. d. L., Lopes, S. R., Batista, C. A. S., Kurths, J., and Viana, R. L. (2014). Synchronization of bursting Hodgkin-Huxley-type neurons in clustered networks. *Physical Review. E, Statistical, Nonlinear, and Soft Matter Physics*, 90(3):32818.

Prescott, S. A. (2013). Excitability: types I, {II}, and {III}. In Jaeger, D. and Jung, R., editors, *Encyclopedia of computational neuroscience*, pages 1–7. Springer New York, New York, {NY}.

Prut, Y. and Perlmutter, S. I. (2003). Firing properties of spinal interneurons during voluntary movement. I. State-dependent regularity of firing. *The Journal of Neuroscience*, 23(29):9600–9610.

Quiroga, R. Q. and Panzeri, S. (2013). *Principles of neural coding*. {CRC} Press.

Rabinovich, M. I., Huerta, R., Varona, P., and Afraimovich, V. S. (2008). Transient cognitive dynamics, metastability, and decision making. *PLoS Computational Biology*, 4(5):1000072.

Reinagel, P., Godwin, D., Sherman, S. M., and Koch, C. (1999). Encoding of visual information by {LGN} bursts. *Journal of Neurophysiology*, 81(5):2558–2569.

Rieke, F., Warland, D., De Ruyter Van Steveninck, R., and Bialek, W. (1999). *Spikes: Exploring The Neural Code (computational Neuroscience)*. Bradford book. The Mit Press, Cambridge, Mass, reprint edition.

Rinzel, J. (1987). A formal classification of bursting mechanisms in excitable systems. In Teramoto, E., Yumaguti, M., and Levin, S., editors, *Mathematical topics in population biology, morphogenesis and neurosciences*, volume 71 of *Lecture notes in biomathematics*, pages 267–281. Springer Berlin Heidelberg, Berlin, Heidelberg.

Roberts, J. A., Gollo, L. L., Abeysuriya, R. G., Roberts, G., Mitchell, P. B., Woolrich, M. W., and Breakspear, M. (2019). Metastable brain waves. *Nature Communications*, 10(1):1056.

Rodriguez, E., George, N., Lachaux, J. P., Martinerie, J., Renault, B., and Varela, F. J. (1999). Perception's shadow: long-distance synchronization of human brain activity. *Nature*, 397(6718):430–433.

Roelfsema, P. R., Engel, A. K., König, P., and Singer, W. (1997). Visuomotor integration is associated with zero time-lag synchronization among cortical areas. *Nature*, 385(6612):157–161.

Ross, S. (2010). *Modeling Phase Transitions in the Brain*. Springer New York.

Santos, V., Szezech, J. D., Batista, A. M., Iarosz, K. C., Baptista, M. S., Ren, H. P., Grebogi, C., Viana, R. L., Caldas, I. L., Maistrenko, Y. L., and Kurths, J. (2018). Riddling: Chimera's dilemma. *Chaos*, 28(8):081105.

Schaefer, N., Rotermund, C., Blumrich, E.-M. M., Lourenco, M. V., Joshi, P., Hegemann, R. U., Jamwal, S., Ali, N., García Romero, E. M., Sharma, S., Ghosh, S., Sinha, J. K., Loke, H., Jain, V., Lepeta, K., Salamian, A., Sharma, M., Golpich, M., Nawrotek, K., Paidi, R. K., Shahidzadeh, S. M., Piermartiri, T., Amini, E., Pastor, V., Wilson, Y., Adeniyi, P. A., Datusalia, A. K., Vafadari, B., Saini, V., Suárez-Pozos, E., Kushwah, N., Fontanet, P., and Turner, A. J. (2017). The malleable brain: plasticity of neural circuits and behavior – a review from students to students. *Journal of Neurochemistry*, 142(6):790–811.

Sciences, D. (2002). *Brain Architecture : Understanding the Basic Plan: Understanding the Basic Plan*. Oxford University Press, {USA}.

Shadlen, M. N. and Newsome, W. T. (1994). Noise, neural codes and cortical organization. *Current Opinion in Neurobiology*, 4(4):569–579.

Shanahan, M. (2010). Metastable chimera states in community-structured oscillator networks. *Chaos*, 20(1):13108.

Shankar Gupta, D., Fingelkurts, A. A., Kröger, M., Zürich, E., Gili, T., Spalletta, G., and Ciullo, V. (2018). Metastable States of Multiscale Brain Networks Are Keys to Crack the Timing Problem. *Frontiers in Computational Neuroscience | www.frontiersin.org*, 12:75.

Sherman, S. M. (2001). Tonic and burst firing: dual modes of thalamocortical relay. *Trends in Neurosciences*, 24(2):122–126.

Shine, J. M., Bissett, P. G., Bell, P. T., Koyejo, O., Balsters, J. H., Gorgolewski, K. J., Moodie, C. A., and Poldrack, R. A. (2016). The Dynamics of Functional Brain Networks: Integrated Network States during Cognitive Task Performance. *Neuron*, 92(2):544–554.

Singer, W. (1999). Neuronal synchrony: a versatile code for the definition of relations? *Neuron*, 24(1):49–65,111.

Softky, W. R. and Koch, C. (1993). The highly irregular firing of cortical cells is inconsistent with temporal integration of random {EPSPs}. *The Journal of Neuroscience*, 13(1):334–350.

Sporns, O. (2013). Network attributes for segregation and integration in the human brain. *Current Opinion in Neurobiology*, 23(2):162–171.

Stein, R. B., Gossen, E. R., and Jones, K. E. (2005). Neuronal variability: noise or part of the signal? *Nature Reviews. Neuroscience*, 6(5):389–397.

Steriade, M. (2003). *Neuronal substrates of sleep and epilepsy*. Cambridge University Press.

Stevens, C. F. and Zador, A. M. (1998). Input synchrony and the irregular firing of cortical neurons. *Nature Neuroscience*, 1(3):210–217.

Stratton, P. and Wiles, J. (2015). Global segregation of cortical activity and metastable dynamics. *Frontiers in Systems Neuroscience*, 9(AUGUST):119.

Strogatz, S. H. (2018). *Nonlinear dynamics and chaos: with applications to physics, biology, chemistry, and engineering*. {CRC} Press.

Su, H., Alroy, G., Kirson, E. D., and Yaari, Y. (2001). Extracellular calcium modulates persistent sodium current-dependent burst-firing in hippocampal pyramidal neurons. *The Journal of Neuroscience*, 21(12):4173–4182.

Swadlow, H. A. and Gusev, A. G. (2001). The impact of 'bursting' thalamic impulses at a neocortical synapse. *Nature Neuroscience*, 4(4):402–408.

Taylor, R. L. (2011). Attractors: Nonstrange to Chaotic. *SIAM Undergraduate Research Online*, 4:72–80.

Timme, M., Wolf, F., and Geisel, T. (2002). Prevalence of Unstable Attractors in Networks of Pulse-Coupled Oscillators. *Physical Review Letters*, 89(15):154105.

Timofeev, I., Grenier, F., Bazhenov, M., Sejnowski, T. J., and Steriade, M. (2000). Origin of slow cortical oscillations in deafferented cortical slabs. *Cerebral Cortex*, 10(12):1185–1199.

Tognoli, E. and Kelso, J. A. (2014). The Metastable Brain. *Neuron*, 81(1):35–48.

Tononi, G., Edelman, G. M., and Sporns, O. (1998a). Complexity and coherency: integrating information in the brain. *Trends in Cognitive Sciences*, 2(12):474–484.

Tononi, G., McIntosh, A. R., Russell, D. P., and Edelman, G. M. (1998b). Functional clustering: identifying strongly interactive brain regions in neuroimaging data. *Neuroimage*, 7(2):133–149.

Tsuda, I. (2013). Chaotic itinerancy. *Scholarpedia*, 8(1):4459.

Tsuda, I. and Umemura, T. (2003). Chaotic itinerancy generated by coupling of Milnor attractors. *Chaos*, 13(3):937–946.

Uhlhaas, P. J., Pipa, G., Lima, B., Melloni, L., Neuenschwander, S., Nikolić, D., and Singer, W. (2009). Neural synchrony in cortical networks: history, concept and current status. *Frontiers in Integrative Neuroscience*, 3:17.

Uhlhaas, P. J. and Singer, W. (2006). Neural synchrony in brain disorders: relevance for cognitive dysfunctions and pathophysiology. *Neuron*, 52(1):155–168.

Van Rossum, G. and Drake Jr, F. L. (1995). *Python reference manual*. Centrum voor Wiskunde en Informatica Amsterdam.

Varela, F., Lachaux, J. P., Rodriguez, E., and Martinerie, J. (2001). The brainweb: phase synchronization and large-scale integration. *Nature Reviews. Neuroscience*, 2(4):229–239.

Váša, F., Shanahan, M., Hellyer, P. J., Scott, G., Cabral, J., and Leech, R. (2015). Effects of lesions on synchrony and metastability in cortical networks. *NeuroImage*, 118:456–467.

Wang, X. J. (1999). Fast burst firing and short-term synaptic plasticity: a model of neocortical chattering neurons. *Neuroscience*, 89(2):347–362.

Watt, A. J. and Desai, N. S. (2010). Homeostatic plasticity and STDP: Keeping a neuron's cool in a fluctuating world.

Watts, D. J. and Strogatz, S. H. (1998). Collective dynamics of 'small-world' networks. *Nature*, 393(6684):440–442.

Werner, G. (2007a). Brain dynamics across levels of organization. *Journal of Physiology Paris*, 101(4-6):273–279.

Werner, G. (2007b). Metastability, criticality and phase transitions in brain and its models. *BioSystems*, 90(2):496–508.

Wildie, M. and Shanahan, M. (2012). Metastability and chimera states in modular delay and pulse-coupled oscillator networks. *Chaos*, 22(4):43131.

Womelsdorf, T. and Fries, P. (2007). The role of neuronal synchronization in selective attention. *Current Opinion in Neurobiology*, 17(2):154–160.

Xu, K., Maidana, J. P., Castro, S., and Orio, P. (2018). Synchronization transition in neuronal networks composed of chaotic or non-chaotic oscillators. *Scientific Reports*, 8(1):8370.

Zemanová, L., Zhou, C., and Kurths, J. (2006). Structural and functional clusters of complex brain networks. *Physica D: Nonlinear Phenomena*, 224(1-2):202–212.